Computational Simulation of Trabecular Bone Distribution around Dental Implants and the Influence of Abutment Design on the Bone Reaction for Implant-Supported Fixed Prosthesis

Dissertation

zur

Erlangung des Doktorgrades (Dr. rer. nat.)

der

Mathematisch-Naturwissenschaftlichen Fakultät

der

Rheinischen Friedrich-Wilhelms-Universität Bonn

Vorgelegt von

Istabrak Hasan

Aus

Bagdad, Irak

Bonn, Mai 2011

Angefertigt mit Genehmigung der Mathematisch-Naturwissenschaftlichen

Fakultät der Rheinischen Friedrich-Wilhelms-Universität Bonn

Table of Content

To my mother who brought me to this marvellous world

Acknowledgment

This thesis would not have been possible without the support of many exceptional people. To them, my thanks:

My advisor, Professor Christoph Bourauel for his guidance, all-round discussions and, and the continuous support to overcome the obstacles that faced the research

My second advisor, Professor Kai-Thomas Brinkmann, for accepting me as a PhD student at him and the friendly cooperation.

Dr. Ludger Keilig for his support in applying the algorithm for my work and consuming the hours for the discussion and numerical support. Ludger, saying thanks is not enough for what you did. Without your help my project could not be successfully finished.

The members of my research group, Dr. Susanne Reimann and Marcel Drolshagen for their friendly support.

For you Sarmad for helping me in writing the first version of my algorithm.

To Uta, my close friend for your smiley face that encouraged me in the darkest time and to be always there when I was in need to you.

Leo and Hans, for the warm family feeling that you supplied me.

My family, without whom I would not be the person I am.

Abstract

Computational modelling of trabecular bone distribution based on the remodelling process is a challenging issue. Up to now, most of bone remodelling models attempted to describe the remodelling process with non-cemented implants of the hip joint. Few studies are published about remodelling processes around dental implants.

This work presents a computational simulation of bone remodelling around dental implants from a biomechanical point of view. The model is based on the stimulation of bone remodelling by a local mechanical stimulus. Furthermore, this study investigates the reaction of the bone to different prosthetic abutment designs that are commonly used for implant-supported fixed prosthesis.

The first part includes the investigation of the influence of abutment design on the bone behaviour at the cervical region of the implants that are used for implant-supported fixed prosthesis. The investigations cover three aspects: Experimental, numerical, and clinical. The experimental part deals with measuring the magnitude of implant micromotion in relation to the abutment design. The numerical part analyses the distribution of stresses and strains and their relation to the abutment design. The clinical part represents the final step for the validation of the experimental and numerical results. The probing depth is measured up to one-year after the placement of the abutments.

The second part of the presented study deals with testing the sensitivity of the applied remodelling model to different mechanical conditions, e.g. varying boundary conditions, loading conditions, material properties, etc.

The third part of this work deals with the simulation of remodelling processes during the healing phase by considering three healing intervals and different tissue layers by means of different mechanical properties at the bone-implant interface.

In conclusion, this work demonstrates, in its first half, the reaction of the bone to the load distribution created by different abutment designs in implant-supported fixed prosthesis. In its second half, the present word describes a computational simulation of trabecular structure around dental implants based

on the change of the apparent bone density as a function of the mechanical daily stimulus.

Chapter 1

1.   Introduction

For a successful dental implant, there is a definitive pattern of mineralised tissue development during osseointegration and bone remodelling. Osseointegration, generally, takes place in the peri-implant region in the first three to six months after the implantation. Thereafter, the implant gains increasing in its stability through the bone remodelling within the surrounding cortical and cancellous bones. After a certain period of healing, an equilibrium status of remodelling can be achieved, where the loss of bone is minimal and the rate of implant failure becomes low.

Bone remodelling has been an important topic of biomechanical research in the long bone community over the past three decades. In this context, one of the most successful methods has been to incorporate finite element analyses. Phenomenologically, there are certain similarities of remodelling mechanisms and algorithms of long bones and alveolar bone. Hence, it is realistic to simulate alveolar bone remodelling by using the procedures established in long bones.

Clinically, the long term success of dental implants can be related to bone turnover activity. For this reason, the understanding of two associative issues becomes critical: (1) how the bone is engaged to the implant and (2) how the morphological changes of bone quality are monitored and predicted.

This thesis studies the relation of prosthetic abutment design to the biomechanical behaviour of the bone. Experimental, numerical, and clinical aspects are considered in this work.

Furthermore, in this thesis we apply a mathematical remodelling model to alveolar bone segment surrounding a dental implant. The model is based on the adaptation of apparent bone density to the local daily stimulus as a function of time. Starting with homogenous distribution of density, by means of finite elements, of the cortical and cancellous bones and ending with a load-dependent density adaptation by applying the remodelling model.

In detail, this thesis is organised as follows:

In Chapter 2, we review the bone architecture, remodelling theories and the common aspects of restorative treatment with implant-supported fixed partial prosthesis which are relevant for this thesis and discuss the most important aspects of prosthetic implant and abutment design.

Chapter 3 presents the materials and methods of this thesis. We present the experimental set-up and clinical protocol for studying the influence of the abutment design on the prognosis of implant-supported fixed prosthesis. Later on, we introduce the mathematical model of bone remodelling and the respective sensitivity analysis of it.

Chapter 4 highlights the force/displacement relation with different abutment designs which was observed from the experimental investigation, followed by presenting the results of the numerical analysis of the corresponding abutment designs used in an implant-supported fixed prosthesis. Finally, the clinical results concerning probing depth are presented together with the statistical analysis of the measured data. The second part of this chapter presents the results obtained by applying the remodelling model to the dental implant and the response of the model to the variation of the mechanical conditions by means of sensitivity analysis. Finally, we present the results of the remodelling model with the presence of soft tissue layer at the bone-implant interface.

In Chapter 5, we discuss the results that were presented in chapter 4 and compare them with those obtained by other similar studies.

Chapter 2

2. Review of the Literature

This chapter covers the background of two main topics: The first part includes bone architecture and (re)modelling processes, the relation between bone remodelling and mechanical stimuli and the corresponding experimental and computational studies that explain this correlation. Finally, fracture healing and bone repair around implants are described as an introduction to the different stages of the healing process around dental implants until the osseointegrated phase. The second part covers the replacing of missing upper anterior teeth by implant-supported fixed partial prostheses (FPP) as a treatment of choice and the influence of implant and abutment design on the prognosis of the prosthesis.

2.1. Bone Biology

Bone is a metabolically active tissue capable of adapting its structure to mechanical stimuli and repairing structural damage through the process of remodelling. The bones of most mammals have four surfaces or bone envelopes upon which the addition or removal of bone can occur: The periosteal, endocortical, trabecular, and Haversian (or intracortical) envelopes. Skeletal envelopes differ in their surface area to volume ratios and in their response to certain stimuli. At each skeletal envelope, bone resorption and formation are executed and regulated by the bone cells, the osteoclast and osteoblast, respectively (Figure 1). Tissue yielded by osteoblastic formation is maintained by the osteocytes and bone lining cells, which are terminally differentiated relics of once-prolific osteoblasts.

The cells that populate bone tissue are derived from different origins, and they proliferate and differentiate in response to different cues. Osteoblast-lineage cells, in addition to regulating bone formation, also regulate bone resorption via an elegant signalling pathway that controls osteoclast generation and activity. Further, bone cells, most probably the osteocytes, are strain-sensitive

cells and can transduce mechanical signals derived from mechanical loading into cues that finally result in reduced bone loss and enhanced bone gain (Robling et al., 2006).
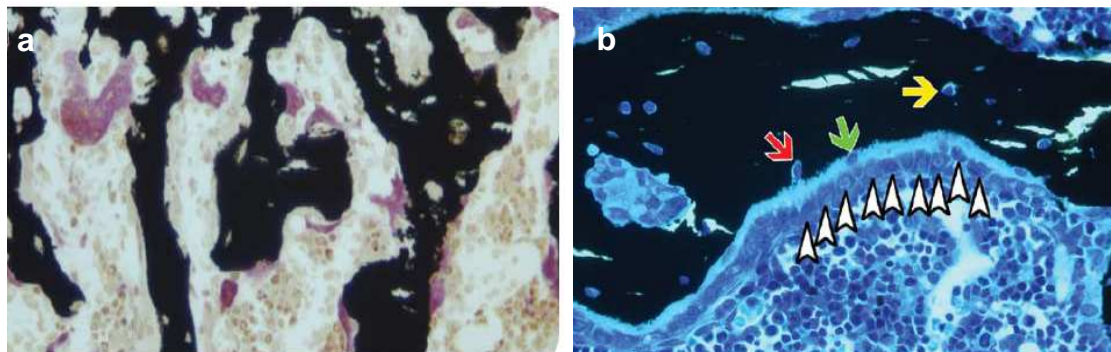
Figure 1: (a) Frontal thin section (4 µm) through a mouse proximal tibia, just beneath the growth plate (primary spongiosa), illustrating the presence of active osteoclasts (*stained pink*) resorbing mineralised cartilage and bone (*stained black*). (b) Frontal thin section (4 µm) through a rat proximal tibia, in the secondary spongiosa, illustrating the process of bone formation by a team of osteoblasts (*white arrowheads*). Bone is stained black, soft tissue and cells are stained blue. Intervening between the mineralised bone and the row of osteoblasts is a pale blue strip of tissue (osteoid) which represents freshly deposited matrix that has not yet incorporated mineral. As the osteoid seam advances behind the osteoblasts, some of the osteoblasts get trapped in their own osteoid matrix (*green arrow*), which subsequently accumulates mineral (*red arrow*), eventually leading to a former osteoblast completely surrounded by mineralised bone (*yellow arrow*), which is now considered an osteocyte (Robling et al., 2006).

2.1.1. Cancellous Bone Architecture

The trabecular arrangement in cancellous bone is obviously not random. Some regions are very dense, whereas others have only sparse trabeculae. In some regions the trabeculae are consistently coarse, whereas other regions consist of finer trabeculae. The mean orientation and degree of anisotropy are

also variables that obviously change between anatomical sites and between individuals.

The variation in trabecular architecture formed the basis for the formulation of *Wolff's law* (Wolff, 1870), which links trabecular architecture to mechanical usage by adaptation and mechanical properties to trabecular architecture by solid and, possibly, fluid mechanics. This explains the interest in cancellous bone architecture. *Wolff* (1870) stated that the architecture related to the mechanical usage "in accordance with mathematical laws", but did not further specify these laws. Much has been learned over the last decades about how the architecture influences mechanical properties, but the influence of a number of architectural features is still uncertain. One of the problems in explicit formulations relating to the cancellous bone architecture is defining and delimiting the architecture variables to be included.

The most important parameter which has been suggested to characterise cancellous bone architecture is the bone volume fraction, which is the volume of bone tissue per unit volume and is dimensionless. A similar scalar quantity is the total mass per unit volume of bone, which is called the structural density or apparent density and which measures the degree of mineralisation as well.

A variety of methods for quantification of cancellous bone architecture has been proposed, including: (1) basic stereological methods, (2) methods based on three-dimensional (3D) reconstruction, (3) traditional two-dimensional (2D) histomorphometry methods, and (4) ad hoc 2D methods (Cowin, 2001).

2.1.2. Bone Modelling and Remodelling

Nearly 40 years ago, *Frost* (1963) began describing two distinct mechanisms by which different types of bone cells team up or work individually to achieve skeletal formation and/or renewal. These processes are bone modelling and remodelling. Both work together in the growing skeleton to define the appropriate skeletal shape, maintain proper serum levels of ions, and repair structurally compromised regions of bone. Bone modelling is a process that works in concert with bone growth and functions to alter the spatial distribution of accumulating tissue presented by growth (Frost, 1986; Jee and Frost, 1992). For example, a growing child's muscle mass increases at a rate that

outpaces accumulation of bone mass (Frost, 1997). Therefore, the tissue being deposited on a bone experiencing an increased or altered loading environment from (a) the growing and increasingly powerful muscles, (b) increasing body mass, and (c) a lengthening diaphysis must be positioned to optimally meet these rapidly evolving mechanical demands (Frost, 1986; Hillam and Skerry, 1995).

This is accomplished by modelling drifts, through which bone is selectively added or removed from existing surfaces with the goal of optimising the geometry of the bone (see Table 1 for the comparison of modelling and remodelling characteristics). Thus modelling can alter the size, shape, and position in tissue space of a typical long bone cross section by selectively inhibiting or promoting cellular activity at the resorptive and appositional surfaces accordingly. Bone modelling at any surface involves osteoclast activation and subsequent resorption of bone, or it involves osteoblast activation and subsequent formation of bone, but not both at the same location. Once skeletal maturity is reached, modelling reduces to a trivial level compared with that which occurs during development (Frost, 1973; Garn, 1970; Lazenby, 1990a; Lazenby 1990b). However, renewed modelling in the adult skeleton can occur in some disease states and in cases where the mechanical loading environment has been altered significantly.

Unlike modelling, which involves either resorption or formation (but not both) at a locus, bone remodelling always follows an activation → resorption → formation sequence (Parfitt, 1979). Remodelling removes and replaces discrete, measurable "packets" of bone. On the intracortical envelope, these replacement packets of bone, or bone structural units (BSUs), comprise secondary osteons. Bone is remodelled by teams of cells derived from different sources which are collectively called the basic multicellular units (BMU). The BMU is a mediator mechanism bridging individual cellular activity to whole bone morphology (Frost, 1986). Intracortical BMUs maintain a distinctive 3D structure as they move through long bone diaphyses in a nearly longitudinal orientation (Hert et al., 1994; Parfitt, 1994). The leading region of the BMU is lined with osteoclasts, specialised cells capable of bone resorption.

Behind the mononuclear cells, rows of osteoblasts (bone-forming cells) adhere to the reversal zone and deposit layers of osteoid (unmineralised bone matrix) centripetally. The size of the remodelling space constricts as more concentric osteonal lamellae are deposited and mineralised. At a specified point, deposition ceases leaving a Haversian canal in the centre of the newly formed osteon. Remodelling on the trabecular and endocortical surfaces follows the same sequence of cellular events as described for the Haversian envelope, except that the cells do not dig and refill tunnels. Rather, they remove and replace pancake-like packets of bone scalloped from these surfaces (Parfitt, 1994). Because of the morphology of the remodelling BMU, where the osteoblast teams trail behind osteoclast teams and the entire structure moves as a unit, the resorption and formation processes are said to be coupled to one another. Coupling is a strictly controlled process in remodelling, ensuring where bone is removed and where new bone will be restored (Parfitt, 2000). The net amount of old bone removed and new bone restored in the remodelling cycle is a quantity called the bone balance. While coupling rarely is affected, bone balance can vary quite widely in many disease states. For example, in osteoporotic patients, resorption and formation are coupled but there is a negative bone balance, i.e. more bone is resorbed than is replaced by the typical BMU (Eriksen et al., 1985).

Table 1: Comparison of modelling and remodelling.

a: of available surface.

b: MES=minimum effective strain.

	Remodelling	Modelling
Location	Spatially related	Different surfaces
Timing	Cyclical	Continuous
Extent	Small (<20%)[a]	Large (>90%)
Apposition rate	Slow (0.3-1.0 µm/day)	Fast (2-10 µm/day)
Balance	No change or net loss	Net gain
MES threshold[b]	<200 microstrain	>1500 microstrain

Cortical bone has a mean age of 20 years and cancellous bone of one to four years (Weibel, 1980). The periodic replacement of bone (bone turnover) helps to maintain load bearing and the capacity of the skeleton to regulate calcium hemoeostasis and haematopoiesis and to repair structural damage.

Remodelling has positive and negative effects on bone quality on the tissue level. It serves to remove microdamage, replace dead and hypermineralised bone, and adapt microarchitecture to local stresses. Remodelling of cancellous bone may perforate and remove trabeculae, and remodelling of cortical bone increases cortical porosity, decreases cortical width and possibly reduces bone strength (Cowin, 2001).

2.1.3. Bone Remodelling and Mechanical Stimuli

The ability of the human skeletal system to adapt to meet the structural demands placed upon it, has intrigued and perplexed the minds of scientists since a long time. Even though numerous theories have been put forward to explain the phenomenon of bone remodelling, a study of the relevant literature shows that a universally accepted theory of the fundamental mechanism or mechanisms which regulate bone resorption and deposition is still a very long far away to be achieved.

Several different theories have been postulated to explain the phenomenon of bone resorption and deposition. The earliest is that proposed by *Wolff* (1870) and further elaborated by him in a monograph (1892). *Wolff's law*, as it is now commonly called, stated that bone responds to the mechanical demands placed upon it. That is to say, for an increase in function or demand the bone responds with deposition and for a decrease in function or demand it responds with resorption. Although *Thompson* (1952), in his classic work "on Growth and Form", and most other subsequent authors have accepted *Wolff's law*, certain doubts concerning this theory do exist. For example, there is strong clinical evidence to suggest that bone "melts way" from around certain orthopaedic screws and implants where "excessive" stress concentrations are expected to occur. This therefore tends to suggest that bone may either be sensitive to the type of demand placed upon it or may possess an upper demand cut-off level above which it changes its response.

Bassett's (1971) interpretation of *Wolff's law* is "the form of bone being given, the bone elements place or displace themselves in the direction of the functional pressure and increase or decrease their mass in order to reflect the amount of functional pressure". This statement suggests that the mechanical demand implied by *Wolff's law* is the pressure, or in other words the stresses, acting on the bone during function. *Bassett* (1971) also states that it is known both clinically and experimentally that a concave region of bone will be built up and a convex region removed.

Frost (1987) proposed in his mechanostat theory that bone responds to a complex interaction of strain magnitude and time. As bone strains are typically very small, it is common to use the term µε (10^{-6}). Conceptually, the interfacial bone maturation, crestal bone loss and loading can be explained by the *Frost* mechanostat theory (Frost, 1987) which connects the two processes of modelling (new bone formation) and remodelling (continuous turnover of older bone without a net change in shape or size). In accordance with the theory, bone acts like a "mechanostat", in that it brings about a biomechanical adaptation, corresponding to the external loading condition.

Frost described four micro-strain zones and related each zone to a mechanical adaptation (Figure 2). The four zones include: The disuse atrophy, steady state, physiologic overload and pathologic overload zones. Both extreme zones (pathologic overload zone and disuse atrophy zone) are proposed to result in a decrease in bone volume. When the peak strain magnitude falls below 50-250 µε, disuse atrophy is proposed to occur. Physiologic overload zone covers the range between 2,500 and 4,000 µε, and is suggested to result in an increase in bone mass. The new bone formed is woven bone (immature bone) that is less mineralised, less organised and consequently weaker than the lamellar bone. It is probable that bone mass will continue to increase, until the bony interface accommodates these changes, and the load strain values then fall back into the range of the steady state zone. This could explain ridge resorption after tooth loss. In the pathologic overload zone, peak strain magnitude of over 4,000 µε may result in net bone resorption. The steady state zone comprises the range between disuse atrophy and physiologic overload zone, and is associated with organised, highly mineralised lamellar bone.
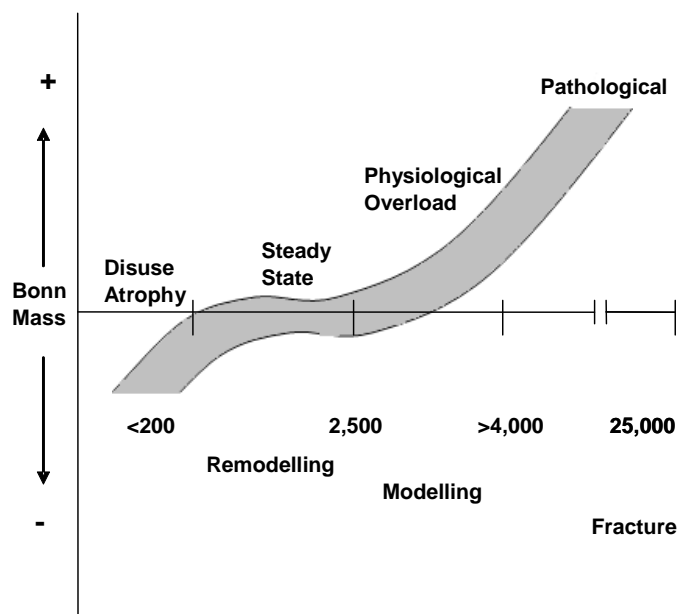
Figure 2: *Frost's* mechanostat theory. Minimal effective strain (MES) of 50 to 250 µε is necessary to prevent net loss in bone mass (disuse atrophy), whereas steady state level of normal remodelling exists between 50 and 250 and 2,500 to 4,000 µε. Shaded area represents range of response in terms of change in bone mass. Peak load magnitudes creating strains above 2,500 to 4,000 µε MES, lead to new bone formation (modelling) that continues until increased bone mass decreases strain values below modelling MES. Peak load levels above 25,000 µε lead to rapid catastrophic fracture (Stanford and Brand, 1999).

2.1.4. Experimental Investigation of Bone Remodelling

The first systematic series of experiments designed to investigate the mechanism of functional adaptation in bone tissue was that conducted by *Hert et al.* (1969) and his coworkers using artificial loads applied to the tibias of rabbits (Hert et al., 1969; Hert et al., 1971; Liskova and Hert, 1971). Experiments in which bones have been subjected to controlled dynamic loads have used sheep (Churches et al., 1979; O'Connor et al., 1982), chickens (Rubin and Lanyon, 1981; Rubin and Lanyon, 1984), and turkeys (Rubin and Lanyon, 1985). In addition to these studies, reports have appeared from static loading experiments which, contrary to *Hert's* finding, suggest that there is an

association between static load and remodelling activity (Hart et al., 1983; Hassler et al., 1980; Meade et al., 1981). In all these static loading studies mathematical models were also developed which appeared to support the existence of a relationship between the remodelling observed and the static stresses produced within the bone tissue. In any artificial loading experiment in vivo, there are two major drawbacks:

1)   Bone remodelling is sensitive to many factors other than mechanical ones and so, the direct and indirect effects of trauma and vascular disturbance can easily obliterate any remodelling related to physiological changes in the bone mechanical situation.

2)   When a continuous load is applied to a bone which is also being functionally loaded, it not only induces static strains, but it may also modulate the superimposed pattern of dynamic strain produced by functional activity.

The first of these dangers can be avoided, or at least reduced, by developing preparations in which the sites of surgical interference are kept remote from those where the remodelling is assessed. The second can be overcome by the use of models in which artificial loads are applied to a bone which is retained in vivo but which is isolated from alternative (natural) sources of loading.

Pearce et al. (2007) studied the similarity between animal and human bone in terms of macrostructure, microstructure, bone composition and bone remodelling rate in dogs, sheep/goat, pigs and rabbits. They concluded that pigs have the most similar bone remodelling behaviour to that of humans followed by dogs and sheep/goat and least similar it was in rabbits.

2.1.5. Computer Simulation of Bone Remodelling

Although global study of bone remodelling through simulation is fundamentally unable to address the actual biologic events which form and resorb bone, an accurate simulation of bone remodelling is an important practical and theoretical tool. Such a simulation could identify prosthetic designs and design features which are likely to lead to problems due to stress shielding, and can show situations in which bone remodelling results in stresses within the prosthesis which could cause failure (Carter, 1987; Carter et al., 1989;

Huiskes et al., 1987; Huiskes et al., 1991; Orr et al., 1990). These simulations can also help in the studies of bone remodelling mechanisms, by indicating the mechanical relationships between bone stress and formation which result in a stable structure which accurately mimics actual bones (Carter et al., 1989; Cowin, 1984; Hart and Davy, 1989; Hart et al., 1984b; Orr et al., 1990). Computerised simulations of bone remodelling thus potentially offer both a theoretical limit on the relationships between stress and bone response to it, and a practical tool for the design of bone repairs and total joint replacements. The process of bone remodelling uses an interrelationship between the microstructure of bone and global stiffness characteristics of the whole bone under load. The mechanism of bone remodelling is one where the stress at a particular site in the bone causes bone tissue to be deposited or removed, yielding a change in the local stiffness of the bone or a change in the shape of the bone. The macroscopic shape and structure of the bone in the human skeleton are as variable as humans themselves are, but they also share the degree of similarity that people share. Thus the microscopic processes which form and resorb bone yield a stable structure which adapts to the variable and common features which humans display.

Numerical modelling applied to bone has primarily been aimed at simulating the bone remodelling concepts as proposed by the early anatomists. These studies are usually aimed at assessing whether the structure of bone can be predicted or developed using a particular mathematical remodelling rule. Considerable success has resulted from many of these studies; the density distribution of bone near joints, and the shape of the long bone diaphyses can be predicted in a qualitative sense using the models developed so far. Thus these studies confirm the correctness of the original qualitative postulates made by the early anatomists.

A bone remodelling scheme based on continuum-level variables (such as tissue volumetric density and strain energy density) cannot model tissue deposition and removal on a cellular level. However, exploring such models offers a chance to assess the stability and the optimising characteristics of these remodelling schemes. By assessing stability and optimising issues, we can assess the influence of local tissue responses on the overall structure, and this can help in identifying the important effects at the cellular level.

For qualitative predictions, it is necessary that the internal mechanical load in the bone structure can be determined accurately in terms of stresses and strains, for which the finite element method (FEM) is an effective tool (Huiskes, 1980). By combining mathematical bone remodelling descriptions with finite element (FE) models, quantitative predictions about bone formation and resorption in realistic bone structures can be made (Fyhrie and Carter, 1986; Hart et al., 1984a; Weinans et al., 1989; Weinans et al., 1990). These models are all based on the principle that bone remodelling is induced by a local mechanical signal which activates the regulating cells (osteoblasts and osteoclasts). This process can be described with a generic mathematical expression, using the apparent density as the characterisation of the internal morphology. The rate of change in the apparent density of the bone at a particular location $d\rho/dt$, with $\rho=\rho(x,y,z)$, can be described as an objective function F, which depends on a particular stimulus at location (x,y,z). It is assumed that this stimulus is directly related to the local mechanical load in the bone and can be determined from the local stress tensor $\sigma=\sigma(x,y,z)$, the local strain tensor $\varepsilon=\varepsilon(x,y,z)$, and the apparent density $\rho=\rho(x,y,z)$:

$$\frac{d\rho}{dt} = F(\sigma, \varepsilon, \rho) \qquad\qquad 0 < \rho \le \rho_{cb}, \qquad\qquad (1)$$

where ρ_{cb} is the maximal density of cortical bone. When the objective function F reaches zero, the system is in equilibrium and the net bone-density rate of change is zero. Such a generic relationship can be specified to be as

$$\frac{d\rho}{dt} = B(S - k) \qquad\qquad 0 < \rho \le \rho_{cb}, \qquad\qquad (2)$$

where B is a constant, $S=S(x,y,z)$ is the daily mechanical stimulus and $k=k(x,y,z)$ is the reference stimulus. When combined with a FE model, S is usually expressed per element. In that case it is, in fact, assumed that there is precisely one sensor point per element. Equation (2) shows that the stimulus strives to become equal to the reference value k, which can either be site-specific $[k=k(x,y,z)]$ or non-site-specific ($k=$constant).

2.1.6. Bone Remodelling Theories

It is widely accepted that bone material has the ability to respond to changes in its mechanical loading environment (i.e. changes in the stress and strain field) by adapting its shape and/or its internal micro-structure. These two aspects are commonly referred to as surface and internal remodelling (Frost, 1964). Bone material is resorbed in regions exposed to small load levels, whereas in highly stressed zones deposition of new bone material sets in. This process of functional adaptation is thought to enable bone to perform its mechanical function with a minimum of mass. However, as clinical practice shows, it can often be detrimental to the long-term success of prostheses and implants used in orthopaedic or dental surgery.

Though significant research has been undertaken to identify possible physical and biochemical phenomena which transform mechanical stresses and strains into actual bone cell processes (for a comprehensive overview see e.g. [Martin and Burr, 1989]), these mechanisms remain not fully understood. Considerable attention has been focused on the development of phenomenologically based numerical simulation tools for predicting the results of the natural adaptation process (Carter et al., 1987; Carter et al., 1989; Cowin and Hegedus, 1976). Most of these approaches assume bone material to show isotropic linear elastic behaviour and reflect the remodelling process by adaptation of the bone apparent density and introducing appropriate stiffness-density relations, by adaptation of the Young's modulus. Up to now, only a limited number of attempts have been undertaken to expand these models to more complex material symmetries, which better reflect the anisotropic behaviour of actual bony tissue (Buchjek, 1990; García et al., 2001; Reiter, 1996).

2.1.6.1.   Bone Remodelling based on the Concept of Micro-Damage

Recent concepts connecting bone mechanics and bone biology not only relate bone remodelling to the adaptation of the internal structure to load, but also to the need to remove fatigue damage (Lee et al., 2002). Microdamage in bone was first described by *Frost* (1960) and is the epiphenomenon of fatigue,

creep, or other accumulative mechanical processes that permanently alter the micro-structure (Martin, 2003). Microdamage is increased by fatigue loading at physiological strains and is associated with the activation of remodelling and osteocyte apoptosis (Verborgt et al., 2000). Remodelling activated by, and in close proximity to, microdamage is described by some authors as "targeted" remodelling as opposed to "random" remodelling that could serve other functions, such as calcium homeostasis (Boyce et al., 1998; Burr, 2002).

Martin (2003) described four types of microdamage:

1) Microcracks, commonly found in cortical bone, which extend approximately 100 μm and is frequently limited by osteonal cement lines,

2) diffuse damage, more commonly found in sectioned trabeculae, appears as patches of more intensely strained mineralised matrix that have apparently been disrupted by locally intense deformations,

3) when small cracks appear in trabeculae as localised networks they are described as cross-hatching cracks, and

4) microfractures are described when trabecular structures are completely fractured.

The principle mechanisms of matrix failure, according to *Boyce et al.* (1998), are strongly dependent on local strain. In regions subjected to tensile strains the bone has diffuse microdamage, whereas in compressive strain regions the tissue develops linear microcracks. However, this concept of bone remodelling is commonly used to describe the remodelling procedure associated with orthodontic treatment.

2.1.6.2.   Strain Theory of Adaptive Elasticity

Cowin and Hegedus (1976) developed the theory of adaptive elasticity to explain the remodelling behaviour of cortical bone. This theory primarily attempts to describe the adaptive nature of the bone from one loading configuration to another, rather than to predict the optimal structure of normal bone. In this theory, it is assumed that the cortical bone tissue has a site-specific natural (or homeostatic) equilibrium strain state. A change of load or an abnormal strain state will stimulate the bone tissue to adapt its mass in such a way that the homeostatic strain state is again obtained (as closely as

possible). The rate of adaptation is coupled to the difference between the homeostatic and actual strain rates. The internal (structural) and the surface (external) remodelling were separately modelled by the authors using the following equations. The elastic modulus (related to density) was made to adapt according to:

$$\frac{dE}{dt} = A_{ij}(e_{ij} - e_{ij}^{o}),$$

(3)

where E is the local modulus of elasticity, e_{ij} is the actual strain tensor, e_{ij}^{o} is the equilibrium strain tensor, and A_{ij} is the matrix of remodelling coefficients. For the external remodelling, the bone was assumed to add or remove material on the periosteal and endosteal surfaces, stimulated by the strain state at those surfaces, according to:

$$\frac{dX}{dt} = B_{ij}(e_{ij} - e_{ij}^{o}),$$

(4)

where X is a characteristic surface coordinate perpendicular to the surface and B_{ij} is a matrix of coefficients for external remodelling.

The first application of the theory of surface remodelling was to highly idealised models of the mid-section of a long bone in the shape of right circular concentric cylinders resembling a thick walled pipe. *Cowin and Firoozbakhsh* (1981a, 1981b) analytically predicted the remodelled shape of the hollow cylinder subjected to constant compressive loads. *Hart et al.* (1982, 1984a, 1984b) determined the remodelled shape for the above problem by using the FEM. Their findings were that both the endosteal and periosteal surfaces moved as a result of remodelling. *Cowin et al.* (1985) also applied the surface remodelling theory to actual bone shape adaptation processes and established preliminary values for the remodelling rate parameters from the literature, quantifying net bone remodelling in animals.

2.1.6.3.   Strain Energy Density Theory of Adaptive Remodelling

Huiskes et al. (1987) used a strain energy density (SED)-based theory as the feed-back control variable to determine the adaptive external and internal remodelling of bone to changing functional requirements. The homeostatic SED distribution was assumed as the remodelling objective.

SED is a scalar measure representing the combined effect of stress and strain. The accumulated energy can provide a means to address the global behaviour of the object. Because of its dual characteristics, SED is widely used in the analysis of damage mechanics of biological materials.

The SED is defined as strain energy per unit volume at any region inside a stress field and can be written as:

$$U = \frac{1}{2} e_{ij} s_{ij} \, ,$$ (5)

where e_{ij} is the strain tensor and s_{ij} is the local stress tensor. The difference between the actual SED, U, and a site-specific homeostatic equilibrium SED, U_n, is assumed as the driving force for adaptive activity. For the internal remodelling, the mathematical formulation of the theory can be written as:

$$\frac{dE}{dt} = C_e (U - U_n) \, ,$$ (6)

and for external remodelling as:

$$\frac{dX}{dt} = C_x (U - U_n) \, ,$$ (7)

where dE/dt is the rate of change of elastic modulus, E; dX/dt is rate of surface growth; and C_e and C_x are remodelling rate coefficients. The above equations can be transformed into finite difference formulations as follows. For internal remodelling:

$$\Delta E = \Delta t C_e (U^i(t) - U_n^i) \qquad i=1,\ n, \tag{8}$$

where n is the number of elements for internal remodelling, ΔE is the change in the elastic modulus in one time-step, and Δt is the period of one time-step. For external remodelling:

$$\Delta X = \Delta t C_x (U^i(t) - U_m^i) \qquad i=1,\ m, \tag{9}$$

where m is the number of surface nodal points considered, ΔX is the growth of the surface nodal point normal to the surface, and Δt is the period of one time step. The constants C_e and C_x determine the remodelling rate. As the values of these constants are not well established, arbitrary values are assigned. Hence, only the final results of the remodelling process are considered realistic. The authors applied internal remodelling simulation to the classical problem of predicting density distribution in the proximal femur (internal or structural remodelling). The remodelling theory was used in conjunction with a 2D FE model. The apparent density (ρ, g/cm^3) of the bone was related to the Young's modulus (E, MPa) as E=3,790 ρ^3. The initial FE Model of the proximal femur had a uniform density distribution, and hence uniform elastic modulus. The elastic modulus was subjected to an upper bound of E=2.5 (10^4) MPa. The remodelling theory suggested by *Huiskes et al.* (1987) in its alternate form takes into account an assumed "lazy" behaviour of bone. This theory incorporates certain threshold levels before the bone starts remodelling due to changes in the SED levels (U) compared to the homeostatic SED levels (U_n). Figure 3 shows the remodelling nature in the presence of a lazy zone. However, the authors do not present an example based on the use of the lazy zone concept.
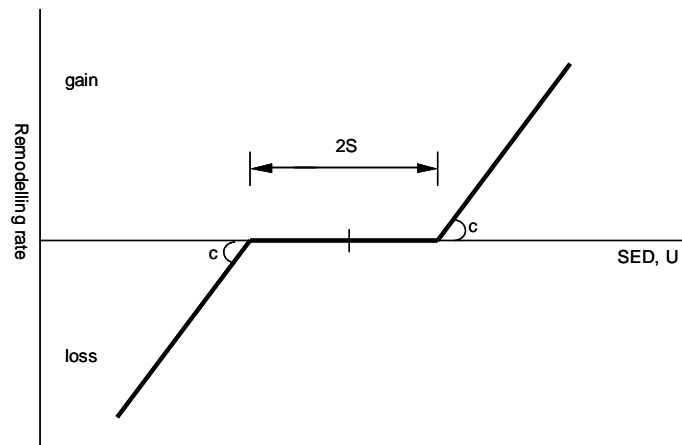
Figure 3: Remodelling concepts based on the SED distribution and the lazy zone adapted from *Blunn and Wait* (1991).

2.1.6.4.   Theory of Self Optimisation

Carter et al. (1989) proposed a single optimisation principle in which bone anisotropy (trabecular orientation) and apparent density (internal remodelling) were adjusted to optimise a function based on strength and stiffness criteria. This principle was implemented using the FE technique to predict the bone density distribution in the femoral head and neck for the single-limb-stance phase of gait. The results revealed a density distribution consistent with that found in the normal femoral head.

Later, *Carter et al.* (1987) expanded the single load approach for predicting bone density changes to encompass the multiple-loading history of the femoral bone over a specified time period. The bone loading histories during an average day were characterised in terms of stress magnitudes or cyclic SED and the number of loading cycles. In other words, the feed back control variable used was the effective stress derived from the SED. Relationships between local bone apparent density and loading history were developed which assumed that bone mass was adjusted in response to the strength and energy considerations. The authors hypothesised that the local apparent density of spongy bone could be approximated by the relationship:

$$\rho \propto \left[\sum n_i s_i^m\right]^{(\frac{1}{2}m)} \qquad , \textit{i=1,c,} \tag{10}$$

where the daily loading history is summarised as c discrete loading conditions and subscript i designates a specific loading condition, n is the number of loading cycles, s is the continuum model cyclic *peak* effective stress (scalar quantity), ρ is the apparent density, and m is constant.

The effective stress (S_{eff}) is related to the SED as:

$$S_{eff} = (2EU)^{\frac{1}{2}}, \tag{11}$$

where E is the continuum model elastic modulus, and U is the continuum model SED. The relation between the elastic modulus and the apparent density of spongy bone is given by:

$$E = 3{,}790\rho^3, \tag{12}$$

The bone is considered to be an isotropic and homogeneous structure in which the apparent density and modulus subsequently vary as the remodelling process is carried out. Initial properties of bone assumed were: E=1,000 MPa (or ρ=0.64 g/cm^3), and U=0.2. The SED and the effective stress were calculated for each loading case. The remodelling was carried out for single and multiple loading histories and the resulting bone density distribution was predicted. The solutions have shown the consolidation of the bone density that created a dense cortical diaphysis and a strong column of cancellous bone in the femoral head. The results were found comparable to that of actual femoral bone architecture. It is important to note that these studies dealt with the prediction of bone morphology (internal modelling) in long bones, namely the femur.

2.2.   Bone Quality and Verifying Methods

The quality or density of bone adjacent to dental implants is an important consideration in the success of dental implants. There are four established bone qualities in the oral cavity as described by *Lekholm and Zarb* (1985). *Quality 1* consists of primarily dense cortical bone that is usually located in the anterior mandible. *Quality 2* has a thick layer of compact bone that surrounds a core of dense cancellous bone that is usually associated with the posterior mandible. *Quality 3* has a thin layer of cortical bone that surrounds a core of dense cancellous bone, which is usually associated with the anterior maxilla. *Quality 4* has a thin layer of cortical bone that surrounds a core of lower density cancellous bone. The posterior maxilla is customarily composed of this least dense quality of bone. This classification system has been used to characterise bone quality during surgical procedures for implant placement. Since this classification can be subjective, other investigators have proposed an extension of this idea by comparing the surgical resistance of the bone during osteotomy preparation (Engquist et al., 1988; Friberg, 1994; Misch, 1993; Trisi and Rao, 1999). However, a study by *Misch* (1993) states that bone quality 1 and 4 can easily be differentiated, but quality 2 and 3 are not as easily discerned (Trisi and Rao, 1999).

The long-term clinical success of titanium dental implants is reported to be highly influenced by both the quality and quantity of available bone (Bahat, 1993; Engquist et al., 1988; Friberg et al., 1991; Higuchi et al., 1995; Jaffin and Berman, 1991; Jemt and Lekholm, 1995; Johns et al., 1992; Mericske-Stern, 1994). For example, better bone quality and quantity in the anterior mandible are usually offered as the main reasons for higher survival rates of dental implants in lower jaws (Bass and Triplett, 1991; Friberg et al., 1991; Jaffin and Berman, 1991). The percentage of bone-implant contact is higher in cortical bone than in cancelleous bone, which provides greater initial stability to the implant during the healing period following insertion. The direction, magnitude and repetition rate of biomechanical forces can influence the modelling and remodelling processes in bone surrounding endosseous implants. Bone can resist rapidly applied loads and bone quality is increased under repetitive forces. If the simulation is within physiologic limits, it may

produce an increase in osseous density at the implant-bone interface (Arpak et al., 1995; Carter and Caler, 1983; Carter, 1984; Misch, 1990; Morris et al., 1995). From this comes the advantage of the immediately loaded implant systems, keeping in mind the importance of maximising the spread and distribution of contacts and to recheck the occlusion during the first days and weeks after immediate/early loading. Therefore, rigid splinting of the prosthesis can provide an advantageous force distribution to all abutments.

Bone quality can be assessed before surgery by computerised tomography using Hounsfield values, by estimation of arch location or during surgery by the tactile sense of the surgeon, or by the torque indicator in the handpiece system (Jemt and Strid, 1994; Misch, 1999).

By measuring the cutting resistance of the jaw bone, the insertion torque (measured in Ncm) can be performed intraoperatively (Friberg et al., 1995a; Friberg et al., 1999; Johansson and Strid, 1994; Meredith, 1998). This measurement, since it is available during or after implantation, cannot be used for surgical planning. From the other hand, quantitative CT-image offers the possibility to measure bone mineral density (BMD) values of cortical and cancellous bone separately (Lindh et al., 1996), although the outcome depends critically on the method used for discriminating these two compartments (Beer, 2000). Furthermore, measurement of average BMD values for both segments does not contain the information sought for assessing implant positions, since BMD values vary locally to a high extent (Friberg et al., 1995b; Ulm et al., 1992). Thus, evaluation of BMD locally or averaged over small regions of interest, comparable in size with the implants, are likely to reflect local bone properties more appropriately.

2.3.   Fracture Healing and Bone Repair around Implants

The interactions in the bone implant interface are initiated from the time of implant insertion. The complex physiologic processes, comparable to those of fracture healing, are regulated by numerous different factors and involve participation of several cell types (Davies et al., 1991). The biological

response can according to fracture healing be divided into primary and secondary healing (Einhorn, 1998).

Primary healing involves a direct healing without formation of callus. Primary healing seems to occur only when optimum conditions exist, i.e. mechanical stability and no presence of gaps; in fracture healing anatomical restoration of the bone fragments is needed. When such conditions are present, the remodelling unit (cutting cones) with osteoclasts will reestablish the haversian canals between the bone ends while the osteoblasts form bone. *Secondary fracture healing* which is supposed to take place around cementless implants occurs when optimum conditions for repair are absent and involves the formation of callus. Histologically, several phases in the process of secondary fracture healing and at the bone-implant interface have been described (Buckwalter et al., 1995a, 1995b; Dhert et al., 1998; Einhorn, 1998). Initially, a haematoma is formed and the inflammatoric response commences. The haematoma is suggested to be a source of signalling molecules which are released from platelets and inflammatoric cells. The haematoma will be invaded by cells and vessels, and callus formation begins after 7–14 days (Dhert et al., 1998; Sennerby et al., 1993). During *stable mechanical conditions* without gaps, intramembraneous bone formation will take place directly after the inflammatoric response (Brånemark et al., 1969; Dhert et al., 1998). The presence of a gap over a certain size creates a different situation. It seems that small defects less than 0.5 mm in diameter heal by direct intramembraneous bone formation, whereas larger gaps will heal through the cartilage stage and an initial scaffold of woven bone which subsequently turns into lamellar bone. In both situations, the newly formed bone adapts itself to the new situation by orienting to the bone architecture. During *unstable mechanical conditions*, the inflammatoric response is prolonged and a fibrous tissue membrane might develop (Søballe et al., 1992a, 1992b). The magnitude of continuous micromotion in combination with the local environment will decide whether the inflammatoric response turns into the formation of chondrocytes and endochondral ossification (secondary fracture healing) (Cameron et al., 1973).

Several research groups (Ament et al., 1994; Beaupré et al., 1992; Biegler, and Hart, 1992; Blenman et al., 1989; Carter et al., 1988; Cheal et al., 1991;

DiGioia et al., 1986) have analysed the local mechanical situation in the fracture callus or in the fracture gap by the FEM. *Claes and Heigele* (1999) developed three 2D axisymmetric FE models. Each model represented one specific healing stage. The first model reflected the morphology occurring two weeks after fracture. The second and third model described the eighth and sixteenth healing week, respectively. The basic overall geometry of the cortex and the callus region was identical for all three models. Tissue differentiation and gradual stiffening of the callus tissue were the fundamental processes of secondary fracture healing. These processes were simulated by changing the element material properties from one stage to the next. The characterisation of the histomorphological sequence of the healing process and the types of tissue involved were based on a previously described animal study (Claes et al., 1995a). Based upon the histologic sections they assumed that these three geometries represented typical ossification patterns.

To describe progressive stiffening of the callus, they assumed four tissue types differing in their elastic material properties. The tissue material properties were obtained from indentation tests on tissue sections from different callus regions (Augat et al., 1997) and were similar to values taken by others (Davy and Connolly, 1982).

In the initial healing stage, the callus consisted only of connective tissue. The second model contained callus of intermediate stiffness in a small region along the periosteum, and soft callus tissue adjacent to it, while the remainder consisted of initial connective tissue (about eight weeks postoperatively). In the third model the callus tissue contained three tissue types: Soft callus, intermediate stiffness callus and stiff callus.

2.4.   Replacing partially Edentulous Ridge by Fixed Prosthesis

2.4.1. Dental Implant Design

The standard implant diameter is 3.75 to 4.00 mm but may vary between 3.00 mm and 6.00 mm, dependent upon the manufacturer, and is to be used according to the location in the jaw and bone quality at the surgical site. The optimal length of dental implants is 10.0 mm or longer, however; shorter implants may be indicated dependent on anatomical structures. But with shorter implants there is a poorer prognosis (Friberg et al., 2000). Screw thread design varies greatly by manufacturer but all are to increase fixture stability and induce osseointegration. Many types of screw designs have been introduced claiming that substantive research to be unnecessary since the new designs are based upon the original well-documented Swedish Brånemark titanium implant. This reasoning is based on the opinion that oral implants represent generic products, a misconceived notion at this stage.

The various look-alike implants differ from one another with respect to titanium composition, thread configuration, and surface topography (Wennerberg et al., 1993). Indeed, the observed differences in surface topography alone are such that they will clearly influence the results in experimental studies. At present there is insufficient knowledge about what governs the incorporation of an oral implant and we lack a great deal of information about optimal composition of the biomaterial, the design and the surface finish of an implant. Therefore every oral implant must be supported by clinical documentation of the specific product without reference to any other implant of assumed similarity (Wennerberg, 1996).

2.4.2. Abutment Design in the Anterior Maxilla

When teeth are lost in the anterior maxilla, the pattern of bone loss cannot be accurately predicted (Atwood, 1962). This change in bone morphology often dictates placement of implants with the long axis in different and exaggerated angulations to satisfy space and aesthetic needs.

Pre-angled abutments have been introduced by implant companies as a prosthetic option for these situations. Abutment angulation is one of the many

biomechanical variables involved in implant dentistry that need a scientific evaluation.

Regardless of the occlusal philosophy, the palatal surfaces of the maxillary anterior teeth provide a vertical ramp for the mandibular anterior teeth to guide the mandible through protrusive and lateral excursions (McHorris, 1982). Thus, most occlusal loads applied to anterior teeth are at an angle to the long axis of the implants. Forces applied off axis may be expected to overload the bone surrounding single-tooth implants, as shown by *Papavasiliou et al.* (1996) by means of FE analysis. This created a controversy when evaluating clinical reports by *Eger et al.* (2000) and *Sethi et al.* (2000). These authors concluded that angled abutments may be considered a suitable restorative option when implants are not placed in ideal axial positions. Studies on the biomechanical behaviour of implants have concluded that the major concentration of stresses at the implant-bone interface usually occurs at the crestal bone level (Benzing et al., 1995; Borchers and Reichart, 1983; Canay et al., 1996; Geng et al., 2004; Geramy and Morgano, 2004; Kenney and Richards, 1998; O'Mahony et al., 2001; van Oosterwyck et al., 1998; Papavasiliou et al., 1996; Patra et al., 1998; Stegaroiu et al., 1998). Few investigators have studied the unavoidable situation of placing and loading implants at an angulation in the anterior maxilla. Furthermore, few conclusions have been drawn from the quantitative data obtained by most stress analysis studies, in terms of the criteria for the elastic limit or failure limit of bone, such as *Frost's* "Mechanostat," *Hill's* potential function, or the *Tsai-Wu* function (Ellis and Natali, 2003; Frost, 1987; Tsai and Wu, 1971).

2.4.3. Implant-supported Fixed Prostheses

Loss of anterior teeth is a compelling reason for prosthodontic treatment as an attempt to restore aesthetic and clinical functions, this can be achieved using conventional dentures which have often provided mixed results (Carlsson, 1998; Jones, 1976). This is particularly true in patients displaying advanced alveolar ridge resorption, which severely compromises the retention and stability of conventional dentures (Carlsson, 1998; Närhi et al., 1997). The development of endosseous dental implants has provided dentists with

exciting treatment options that have revolutionised the management of the partially and completely edentulous patients (Albrektsson, 1988; Kirsch and Mentag, 1986). Successful treatment with implant-supported prostheses requires the understanding and implementation of basic biomechanical principles coupled with the ability to satisfy the patient's function and aesthetic demands. Osseointegrated implant-supported prostheses were originally prescribed for edentulous patients and the success rates for them have been encouraging (Adell et al., 1981; Adell et al., 1990; Zarb and Schmitt, 1990).

This biotechnological breakthrough ushered in three important developments in prosthodontic treatment: (1) potential for stable and electively fixed prosthesis, (2) retardation in resorption of the residual ridge, and (3) minimal risk of pre-prosthetic surgical morbidity. It also offered scope to expand the management of edentulism to encompass partial edentulism as well as complete edentulism (Zarb and Zarb, 2002).

Following the success of implant-supported prosthesis in the edentulous arch, the use of implants for the treatment of partially edentulous patients increased (Lekholm et al., 1994). Because guidelines for treating partially edentulous cases did not exist, the same principles associated with completely edentulous prosthetic applications were employed (Zarb et al., 1987). Initially, success rates for partially edentulous implant restorations were somewhat less favourable (Smith, 1990). Partially edentulous ridge treated with implant-supported prostheses presented new complications and unique maintenance problems for the dentist to solve (van Steenberghe et al., 1990; Sullivan, 1986). Currently, partially edentulous success rate improved and, in some cases, equalled those reported for the completely edentulous arch (Lindh et al., 1998).

As a concession of the fact that the jaw bone character, as defined and classified by *Lekholm and Zarb* (1985), differs between the maxilla and the mandible, the observation of the implant-supported prosthesis in the mandible cannot automatically be considered applicable also in the maxilla.

Chapter 3

3.   Materials and Methods

3.1. Mechanical Investigation of Different Implant and Abutment Designs: Experimental, Numerical and Clinical Aspects

This chapter describes the materials and methods used to study the primary stability of immediately loaded dental implants with two different geometries and the relation of the abutment design to the crestal bone resorption. A detailed description of sample preparation and measurement set-up of the experiment is presented, in addition to the construction of the corresponding numerical models and their analyses by means of FEM.

Later on, the development of the numerical models of implant-supported FPP in the anterior maxillary region with two different abutment designs is described. Finally, the clinical protocol for studying the relation of abutment design to the crestal bone resorption around immediately loaded and osseointegrated dental implants used for FPP is presented. The criteria of patient selection are mentioned followed by the analysis method of the data.

3.1.1. Implant Design and Geometry

3.1.1.1.   Tiolox® Implants

Tiolox® implants are conical titanium screw-implants that are not self-tapping because of their passive thread design. The implant surface is ceramic blasted in the endosteal area and 1.0 mm highly polished at the gingival part which is believed to provide a tight formation of soft marginal tissue and optimum hygiene (Figure 4a).

3.1.1.2.   tioLgic© Implants

tioLgic© Implants have a conical ceramic-blasted surface design with a 0.3 mm cervical chamber of implant shoulder and crestal fine threads at the neck region of the implant that is in contact with the cortical part of the avleolae, while there is a progressive coarse thread and thread flanks with lengthwise

grooves along the threads of the implant part that is in contact to the cancellous bone to prevent postoperative pressure necrosis (Figure 4b).

1 mm

Fine thread region

Progressive coarse thread region

(a)   **(b)**
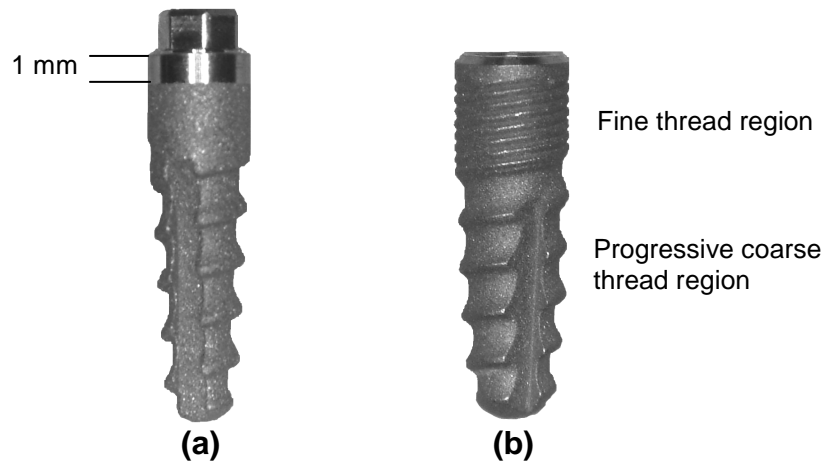
Figure 4: Implant design: (a) Tiolox$^®$ and (b) tioLgic$^©$ system.

3.1.2. Abutment Design

Abutments are the prosthetic components through which the final fixed restoration is attached to the implant. Tiolox$^®$ and tioLgic$^©$ abutments are manufactured from titanium and available in straight and 20°-angled shapes with different gingival height. The abutment is connected to the implant by means of a screw with a torque of 20 Ncm. Figure 5 illustrates the detailed dimensions of the available abutments.
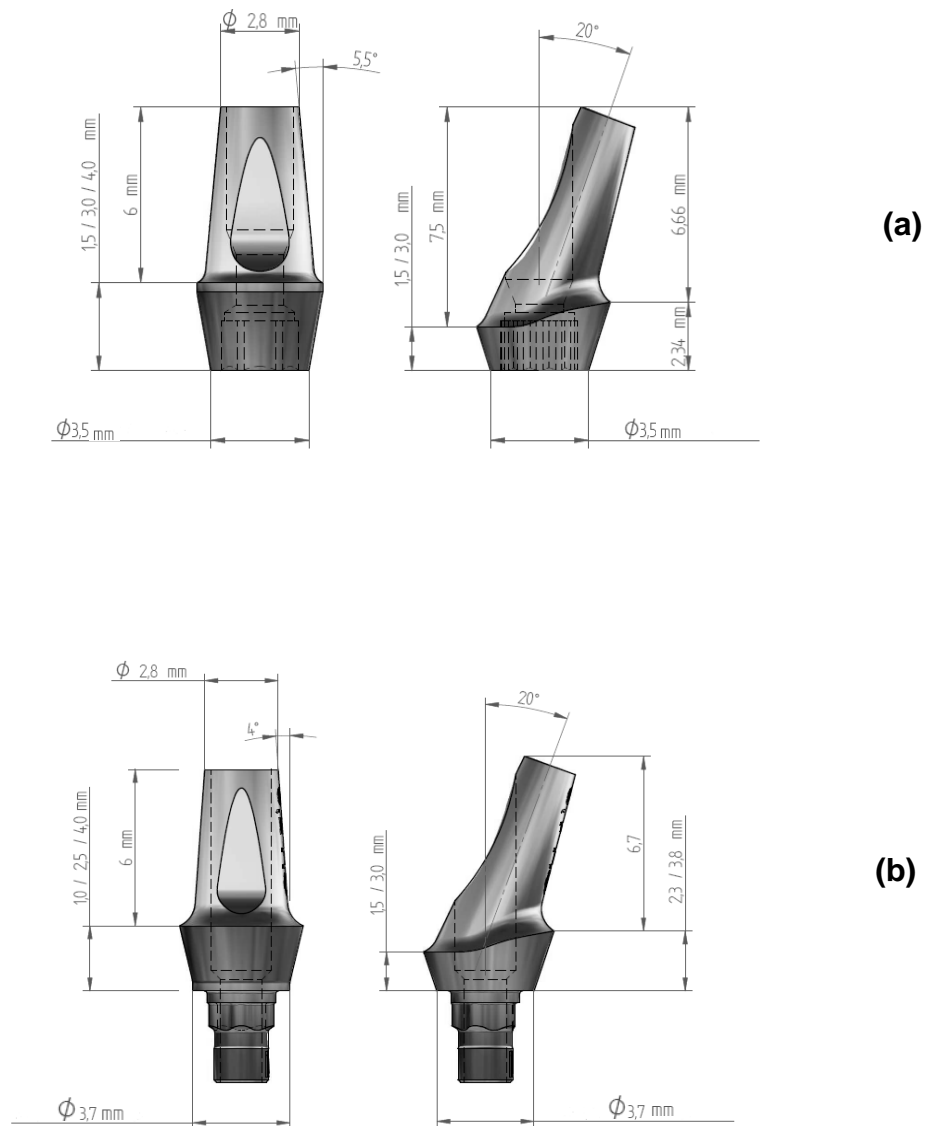
Figure 5: Titanium abutments that were used in this study with the detailed dimensions (Dentaurum Implants, GmbH): (a) Tiolox® abutment system and (b) tioLgic© abutment system.

3.1.3. Fixed Partial Prosthesis Models

This section includes four FE-models of four-unit FPP supported by two endosseous implants in the premaxilla to study the distribution of stresses and strains around dental implants in immediate loading and osseointegrated cases. This is a qualitative and quantitative study of the influence of the abutment design on the stresses and strains in the bone.

The following three-dimensional FE models were constructed using the FE package Marc Mentat 2007 (MSC. Software, Santa Ana, CA-USA) representing two clinical situations: (1) A four-unit FPP supported by two endosseous implants in the incisal region of the maxilla connected to straight abutments and (2) an identical model in which the implants were connected to 20°-angled abutments with a modification in the ori entation of the implants. A total of six models were developed, details of the studied models are summarised in Table 2.

The maxillary bone was modelled using the anterior part of an idealised model of a fully dentulous maxilla. The crowns of the maxillary incisors were modified to be used as the units of the fixed prosthesis and have the benefit of preserving the normal position of the final prosthesis.

The maxillary bone was modelled using the data set of the anterior part of an idealised model of a fully dentulous maxilla (Viewpoint Data Labs, UK) to eliminate individual variations. The crowns of the maxillary incisors of the model were modified for use as the units of the fixed prosthesis. Their position and orientation was maintained according to the original data set in order to define the normal position of the final prosthesis. The bone in the anterior maxilla was classified as quality 2 bone, described by *Lekholm and Zarb* (1985) as a thick layer of cortical bone surrounding a core of dense cancellous bone. A layer of cortical bone with a thickness of 1 mm was modelled on the labial and palatal parts of the alveolar bone model. FE models of tioLogic[©] implants (dimension: 3.7x11 mm, Dentaurum Implants GmbH, Germany) were imported into the bone model. These implants proved to be suitable for the given loading case, based on the uniform loading and homogeneous distribution of the stress and strain as shown in a previous study (Rahimi et al., 2009). Geometries of the implants were taken from the corresponding

CAD data and oriented within the bone model based on the position of the corresponding crowns and abutments in the lateral incisor regions.

Both implants in each model were connected either to straight or 20° angled abutments. The abutments were designed using cylinder models with the diameters given by the manufacturer (Dentaurum Implants GmbH). Since it was not the primary goal of the present study to investigate the stress distribution at the implant-abutment interface, the implant-abutment complex was modelled as a rigid structure.

Differences in the models were as follows: For the first two models (angled and straight abutments), the final prosthesis was considered to build up a rigid structure with the underlying abutment to exclude the influence of the prosthesis on the final results of the strains and stresses. In further two models, a contact analysis between the abutments and the FPP was performed. Contact analysis between the implant and the implant bed was performed in these four models to simulate immediate loading. In the last two models, the osseointegrated situation was simulated by a rigid connection between bone and implant surface. Figures 6a and 6b illustrate the main components of the FE models.

Table 2: Analysis conditions of the six FPP models.

Model with	Description
Straight abutments (SAM)	Immediate loading situation, abutment and prosthesis are one piece.
Straight abutments (SAM)	Immediate loading situation, abutment and prosthesis are in contact.
Angled abutments (AAM)	Immediate loading situation, abutment and prosthesis are one piece.
Angled abutments (AAM)	Immediate loading situation, abutment and prosthesis are in contact.
Straight abutments (SAM)	Complete osseointegration situation, abutment and prosthesis are one piece.
Angled abutments (AAM)	Complete osseointegration situation, abutment and prosthesis are one piece.
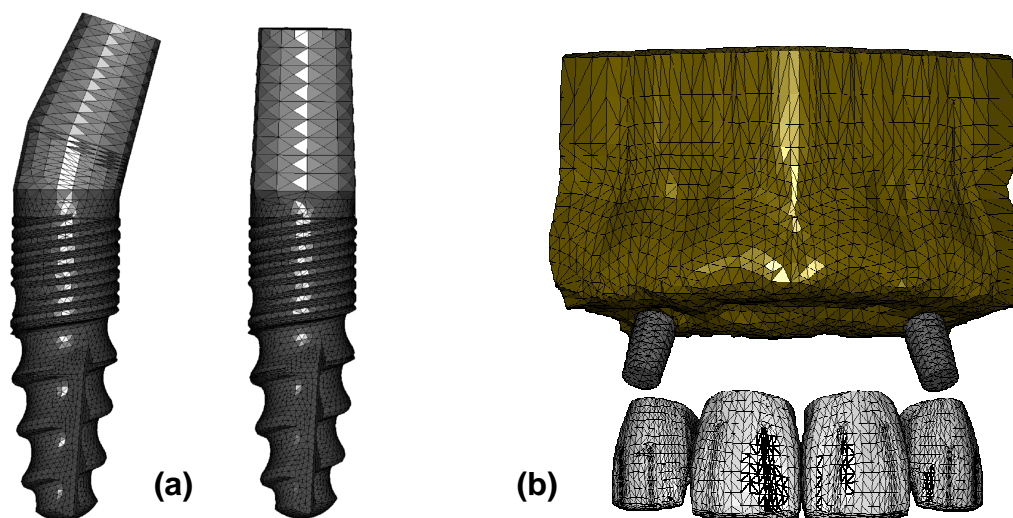
Figure 6: FE models of the four-unit fixed partial prosthesis supported by two endossous tioLogic© implants. (a) Implant connected to straight and angled abutments and (b) FE model of FPP with straight abutments.

The outer surfaces of the maxilla were constrained in all three degrees of freedom. For comparison reasons, the four units of the prosthesis were loaded with clearly predefined forces at an angle of 45° to the long axis of the abutment, palatally at the cingulum area in palato-labial direction. The magnitude of the force applied on each unit was 37.5 N, i.e. the total load applied to the prosthesis was 150 N, corresponding to bite forces determined in earlier studies (Helkimo et al., 1977). This single loading condition was selected, as it was not the intention of this part of the study to analyse the loading behaviour of one predefined FPP under various force systems, but to compare the loading behaviour of the different implant-abutment systems. Figure 7 illustrates the boundary conditions applied in the analysis.
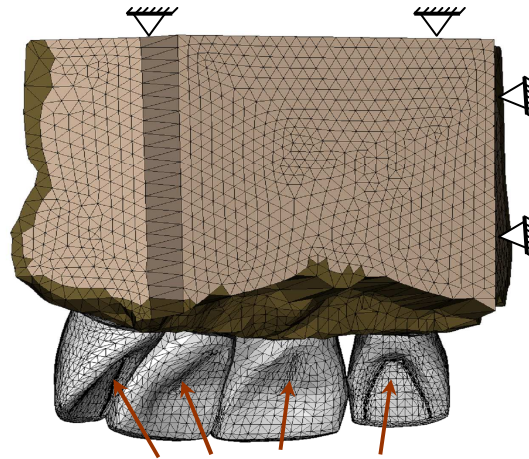
Figure 7: Static and kinematic boundary conditions of the FPP models. The arrows indicate the position of the applied load on each unit of the prosthesis.

The element type used was a four-noded tetrahedral element. The final models had a total number of 199,235 elements and 47,606 nodes for the model with the straight abutments (immediately loaded, one piece abutment prosthesis), 199,238 elements and 48,012 nodes for the model with the straight abutments (abutment prosthesis in contact), 199,238 elements and 37,508 nodes for the model with the straight abutments (osseointegrated, one piece abutment prosthesis), 204,032 elements and 48,618 nodes for the model with angled abutments (one piece abutment prosthesis), 204,032 elements and 49,333 nodes for the model with the angled abutments (abutment prosthesis in contact) and 204,032 elements and 38,472 nodes for the model with angled abutments (osseointegrated, one piece abutment prosthesis).

Again, in order to reduce the influence of individualised geometrical or material parameter variations, bone has been considered as an isotropic and homogeneous material (van Oosterwyck et al., 1998). The material properties of the four different types of materials (cortical bone, cancellous bone, titanium alloy and zirconium) used for the different components of the models are listed in Table 3.

Table 3: Material properties of FPP models.

Material	Young's modulus (MPa)	Poisson's ratio
Cortical bone	20,000	0.30
Cancellous bone	1,000	0.30
Titanium alloy	110,000	0.30
Zirconium	205,000	0.30

3.1.4. Experimental Protocol

In this part of the study bovine ribs were used as implant bed. The segments were selected to have a 2 to 3 mm thick layer of cortical bone that surrounds a wide core of cancellous bone. The segments had a length of approximately 15 mm and a height of around 30 mm (see Figure 8).

Two implant geometries were used, the first with 1 mm highly polished area at the gingival part and roughened neck region (Tiolox[®] implants, Dentaurum Implants GmbH, Germany) and the second with crestal fine threads at the neck region of the implant that is in contact with the cortical part of the alveolus (tioLogic[©] implant, Dentaurum Implants GmbH, Germany). Both implant systems are conical, screw-shaped with passive threads (Figures 4a and 4b). Tow different abutment designs were considered in the study, straight and 20°-angled abutments (Figures 5a and 5 b).

As the major goal of this part of the study was to determine the primary stability of the implants that were used to support the FPP, the implants with or without the abutment were subjected to a force of 75 N at an angle of 45° (Lundgren et al., 1987; Schaeffer, 1949) from the long axis of the abutment on its upper most part using the Hexapod Measurement System (see section 3.1.3.1. for details). The force was not applied near the cingulum area to avoid the complexity of the measuring set up.

Figure 9 illustrates schematically the loading of the implant in the anterior maxillary region with an angled abutment. The total number of specimens was 30, that received 16 tioLgic[©] implants (Ø 3.7 mm, L 15 mm), 14 Tiolox[®] implants (Ø 3.5 mm, L 16 mm) with 15 straight abutments and 15 angled abutments for both implant systems.

Figure 8: Bovine rib segment with cortical thickness of about 3 mm.
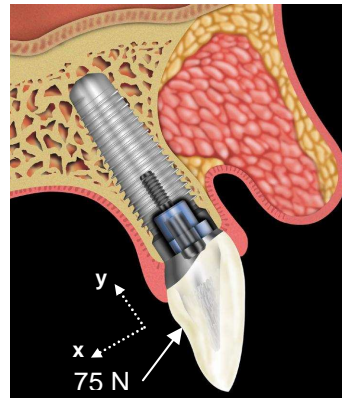
Figure 9: Schematic representation of the loading on the implant in the normal occlusion with the opposing tooth/implant.

Figure 10: Angled abutment mounted onto a Tiolox® implant.

3.1.4.1.　　　　Implant Insertion and Measurement Set-up

Bovine rib segments that had a 2–3 mm thick cortical layer surrounding a wide core of cancellous bone were selected and sawed with continuous lubrication to avoid excessive heating during the cutting procedure. Later on, tioLogic© and Tiolox® implants were inserted according to the surgical protocol of the manufacturer, that included preparing the surface, where the implants were planned to be inserted using a surface cutter, followed by drilling the implant position by a depth drill and conical former. Subsequently, implants were inserted into the place manually with the aid of a torque ratchet. Ten implants from each system received titanium prosthetic abutments (five straight and five angled abutments) that were fixed to the implants by applying a torque of

20 Ncm. Figure 10 shows a specimen with an angled abutment connected to a Tiolox[®] implant.

The segments were then mounted into the specimen-holder such that the axial components of the applied load were parallel to the long axis of the abutment. The stability of the specimens within the holder was achieved by embedding them up to the half into a resin (Technovit 4004, Heraeus Kulzer GmbH & Co. KG). As a next step, implant displacements and rotations were measured using the self-developed biomechanical Hexapod Measurement System (HexMeS) which is composed basically of three components: optical, force controlling, and loading units where the force can be applied by defining a certain distance that the hexapod has to move (for detailed description of the measuring system please see Keilig et al., 2004). The total distance for the hexapod movement was given to be between 0.5 mm and 1.5 mm. Figure 11 summarises the measurement set-up of the study.
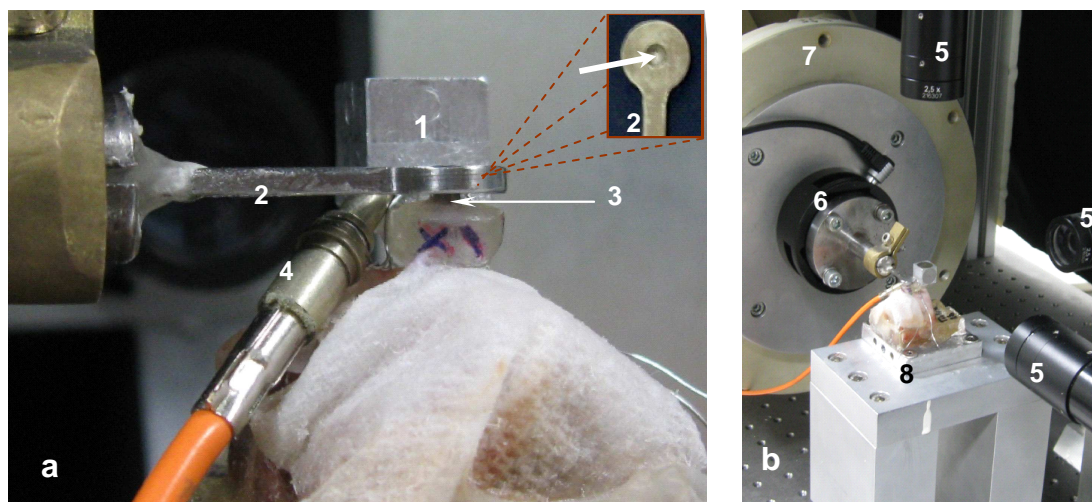
Figure 11: (a) Measurement set-up of the experimental study: The cube (1) is equipped with three pin-holes that are back-illuminated by a laser (4). The spots are registered by three high-resolution video cameras (b, 5). The lever arm (2) was adjusted in such a way that the half spherical shape (arrow) was positioned directly in contact with the abutment (3). The laser beam is guided by an optical fibre (4).

(b) Overall view of the apparatus with the three CCD cameras (5), a force/torque transducer (6), the hexapod (7) and a specimen holder (8).

3.1.4.2. Reconstruction and Development of Numerical Models

A total of eight samples, two for each abutment design, were finally selected for geometrical reconstruction and numerical analysis, respectively. The normal occlusal force of implants at the anterior region is around 75 N at an angle of 45° in labio-apical direction (Lundgren et al., 1987). Accordingly, samples selection for the numerical analysis was for those that were subjected to approximately the same loading components, i.e. the loading of the selected eight samples was within 30 to 36 N in transverse direction and 9 to 22 N in vertical direction. The selected samples are listed in Table 10 (section 4.1.2.).

The reconstruction of implant and bone geometry was done using the self-developed ADOR-3D software (Rahimi et al., 2005) based on μCT-images (self-developed apparatus with XRD 0840 AN digital x-ray detector, Zentralabteilung Technologie ZAT, Forschungszentrum Jülich GmbH, Germany). Following the reconstruction of implant and bone geometries, numerical models were developed. Bone was considered to be an isotropic homogeneous material. Three material properties were given, namely titanium for implant and abutment, cortical bone and cancellous bone. Table 4 lists the mechanical properties of the used materials. The final models had a total number of 150,872±625 tetrahedral elements and 36,240±225 nodes. The final models had a total number of 150,872±625 tetrahedral elements and 36,240±225 nodes.

Table 4: Material properties of the numerical models.

*_Makoto et al._ (2003) demonstrated the averages of longitudinal elastic moduli of bovine cortical bone to be 17.9±4.1 GPa.

**_Poumarat and Squire_ (1993) obtained an elastic modulus of 173±97 MPa for bovine bone.

	Young's modulus (MPa)	Poisson's ratio
Titatium	110,000	0.30
Bovine cortical bone	17,000*	0.30
Bovine spongeous bone	270**	0.30

The implant in each model was loaded in axial and transverse directions with the same force magnitudes measured in the experiments (see Table 11, section 4.1.2.). The end faces of the bone were constrained in three degrees of freedom in the position where bone has been embedded in the resin. Figure 12 illustrates the boundary conditions of the FE-models.

Figure 12: Boundary conditions of the numerical models.

3.1.5. Clinical Protocol and Study Design

The aim of this part was to follow the changes of crestal bone around dental implants in association with abutment design in nonsubmerged (immediately loaded) and submerged (osseointegrated) cases. Bone resorption by means of measuring probing depth was followed after six and twelve months from the placement of abutments to compare the obtained results with the experimental and numerical hypotheses that were discussed in sections 3.1.2. and 3.1.3.

Accordingly, patients were selected from August 2008 until August 2009. Patient data was anonymised and passed to the observer who was not the doctor. The selection was based on the protocol criteria that were as follows: The patients had an edentulous ridge in the anterior maxilla that required a FPP treatment, bone quality was 2. The patients in this study were in good health status. Patients with diabetes were not excluded provided their condition was well controlled. Although smoking was discouraged, smokers were not excluded.

The selected patients were divided, according to the treatment necessity, into two groups:

1.   *Study group*, patients received nonsubmerged dental implants, and

2.   *control group*, patients received submerged implants and underwent a healing period of five to six months.

Each group was further subdivided into two groups according to the received abutment design (whether straight or angled). The design of abutments used for each patient was documented.

Patients were recalled after six and twelve months from the date of abutment insertion for measuring the probing depth medially and distally. Probing depth was measured from the implant-abutment connecting line (as a reference line) until the first bone contact.

A total of 24 Patients were included in this study, 11 patients for the study group and 13 for the control group. The mean age of the patients was 63 years. The total number of implants was 110 (tioLgic©, Dentaurum Implants GmbH, Germany), 64 nonsubmerged implants for the study group and 46 submerged implants for the control group. The Implants had diameters of 3.3 to 4.2 mm and lengths of 9 to 17 mm.

The probing depth measured at the visit of abutment insertion was considered to be the zero measurement for the follow-up. Cervical resorption for the study and control groups was measured.

3.1.5.1.   Statistical Analysis

The differences of the mean bone probing depth after six and twelve months were analysed mesially and distally in association with straight and angled

abutments for statistical significance using the Mann-Whitney test (WinStat[®], version 2003 for Microsoft Excel). The data were grouped according to the abutment design (straight or angled) and implant treatment (submerged or nonsubmerged, Table 5).

The null hypotheses were as follows:

1. There is no significant difference of the crestal bone loss for the straight or angled abutments with the implant treatment protocol (submerged or nonsubmerged),

2. there is no significant difference of crestal bone loss with straight and angled abutments for both immediate loading and submerged implantation protocol.

A significance level of 0.05 was chosen.

Table 5: Characteristics of the groups of the study.

	Study group	**Control group**
Implant treatment	Nonsubmerged	Submerged
Number of straight abutments	36	24
Number of angled abutments	28	22
Number of patients	11	13
female: male	7:4	9:4
Average age	55	61
Implant type	tioLgic[©]	tioLgic[©]

3.2.   Bone Remodelling Theory

This section discusses the theory that has been selected to investigate the response of the bone around dental implants in fully osseointegrated case followed by testing the sensitivity of the applied simulation with various boundary conditions, bone material properties, loading magnitudes and directions, bone quality and implant macro-design. Later on, the validation of the tested remodelling model to a selected clinical case is presented. Finally, the influence of applying a soft tissue layer with different thicknesses on the simulation was tested. This step afterward was necessary to study the behaviour of bone around the implant throughout the healing phase under immediate loading conditions.

3.2.1. Bone Remodelling Simulation

Internal bone remodelling simulation has been done based on the theory developed by *Weinans et al.* (1992) and expanded by *Li et al.* (2007), where the change in bone density ρ is expressed as a function of the mechanical stimulus:

$$\frac{\mathrm{d}\rho}{\mathrm{dt}} = B(\frac{U}{\rho}-k) - D(\frac{U}{\rho}-k)^2 \qquad 0 < \rho \le \rho_{cb}, \tag{13}$$

where B and D are constants, U/ρ is the mechanical daily stimulus, k is the threshold value for the stimulus and ρ_{cb} is the ideal density of bone without porosity.

The two roots of Equation (13), k and $B/D+k$, which are called the critical loads, divide the whole loading range into three regions: Underload resorption region, growth region and overload resorption region. By changing the parameters k, B, and D, we can adjust the shape and position of the quadratic curve to mach the mechanical behaviour of the different bone types. The dead (lazy) zone has been considered in this model:

$$\frac{d\rho}{dt} = \begin{cases} B(\frac{U}{\rho}-k+w)-D(\frac{U}{\rho}-k+w)^2 & \text{if} & \frac{U}{\rho}<(k-w), \\ \\ 0 & \text{if} & k-w\le\frac{U}{\rho}\le k+w, \\ \\ B(\frac{U}{\rho}-k-w)-D(\frac{U}{\rho}-k-w)^2 & \text{if} & \frac{U}{\rho}>(k+w), \end{cases} \quad (14)$$

where w is the half-width of the dead zone which represents a certain percentage of k.

Strain energy density U, is taken as the apparent strain energy density and there is no consideration for the stress history. Therefore, we can use current stress and strain to express the strain energy density. For uniaxial loading condition, $U=\sigma\varepsilon/2=\sigma^2/2E$. If the following empirical relationship between bone density and Young's modulus is also considered, i.e.

$$E=C\rho^3, \tag{15}$$

where C is a constant and has the value of 3,790 MPa (g cm^{-3})$^{-3}$ (Carter and Hayes, 1977), we can express the mechanical stimulus directly as a function of stress:

$$\frac{U}{\rho}=\frac{\sigma^2}{2E\rho}=\frac{\sigma^2}{2C\rho^4} \tag{16}$$

Euler method was used to solve the above ordinary differential equation numerically:

$$\rho_{n+1}^* = \rho_n + \Delta t\, f(\sigma,\rho_n),$$

$$\rho_{n+1}=\rho_n+\frac{\Delta t}{2}\left[f(\sigma,\rho_n)+f(\sigma,\rho_{n+1}^*)\right] \quad 0<\rho\le\rho_{cb}. \tag{17}$$

A small constant time step Δt (10^{-4} x time span) was selected to avoid large local and truncation errors. The initial density of the bone ρ_0 was calculated according to the obtained results of von Mises stress and strain energy density SED from the original FE model in the Marc Mentat FE package according to Equation (16). Figure 13 illustrates the block diagram of the used remodelling algorithm.
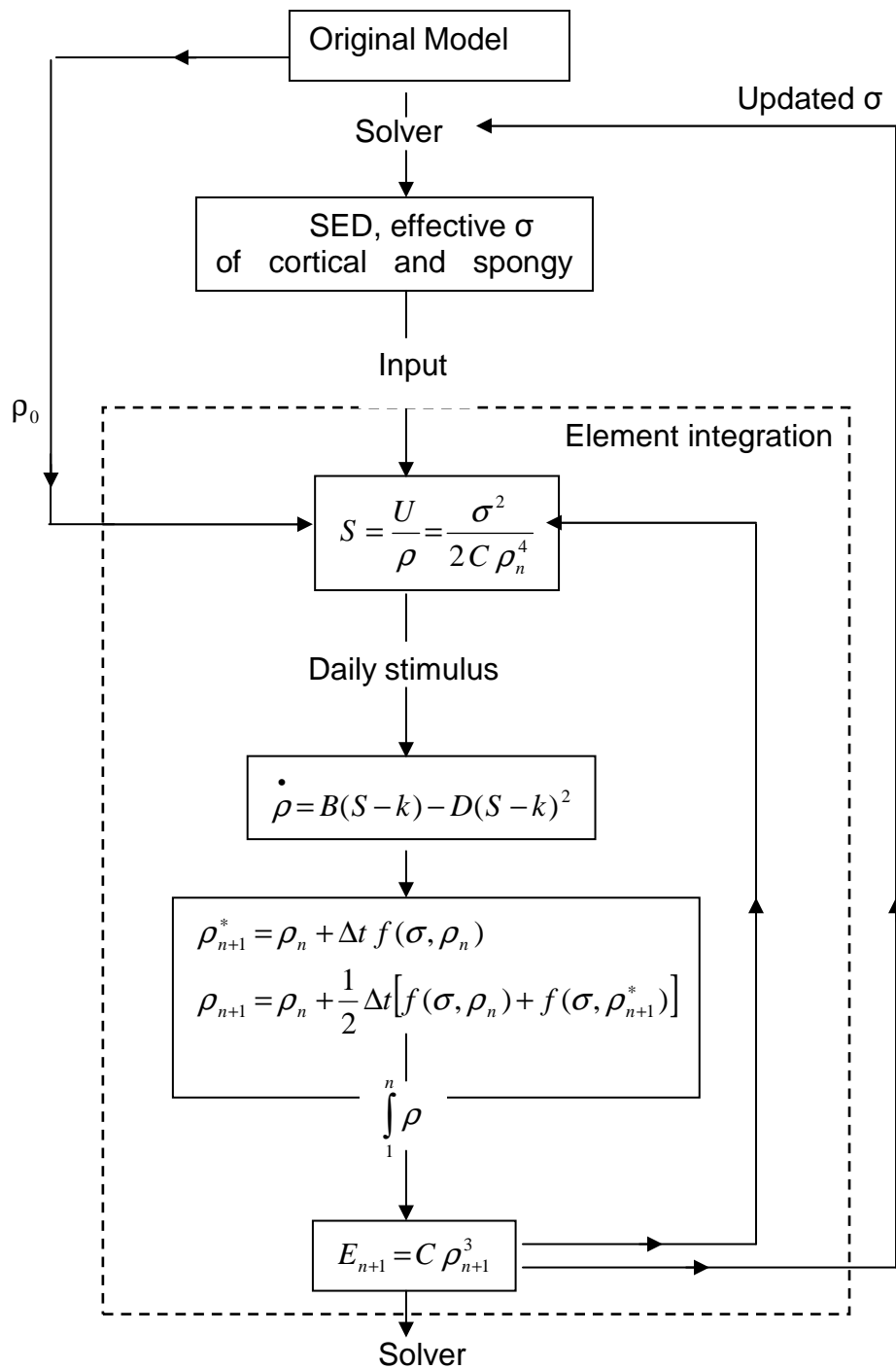

Figure 13: A block diagram of the algorithm of the remodelling model.

The identification of the critical loads (stimulus), namely the effective- and disuse-region strains were based on the mechanostat theory (Frost, 2003). *Frost* (2003) described a threshold MESr below which the mechanically-controlled disuse-mode remodelling function of decreasing a hollow load-bearing bone LBB's strength to maximally act, and above which it begins to decrease (conservation-mode remodelling may replace the disuse mode when typical peak bone strains rise to or above 400 με). The mechanically-controlled remodelling function of increasing bone's strain begins above the typical peak dynamic strains E and its activity would be increased as repeated strains increased in size toward bone's operational microdamage threshold range MESp, above which unrepaired microscopic fatigue damage MDx can begin to accumulate to the bone fracture strength Fx.

The values of the above mentioned thresholds, as suggested by *Frost* were:

MESr: 50-200 με,   1-4 MPa,

E: ~400 με,   8 MPa,

MESp: ~3,000 με,   60 MPa, and

Fx: 25,000 με,   500 MPa.

Stress values represent Hook's stresses that were calculated with bone stiffness of 20,000 MPa.

A simplified description of the threshold ranges in association with the remodelling process is illustrated in Figure 14.
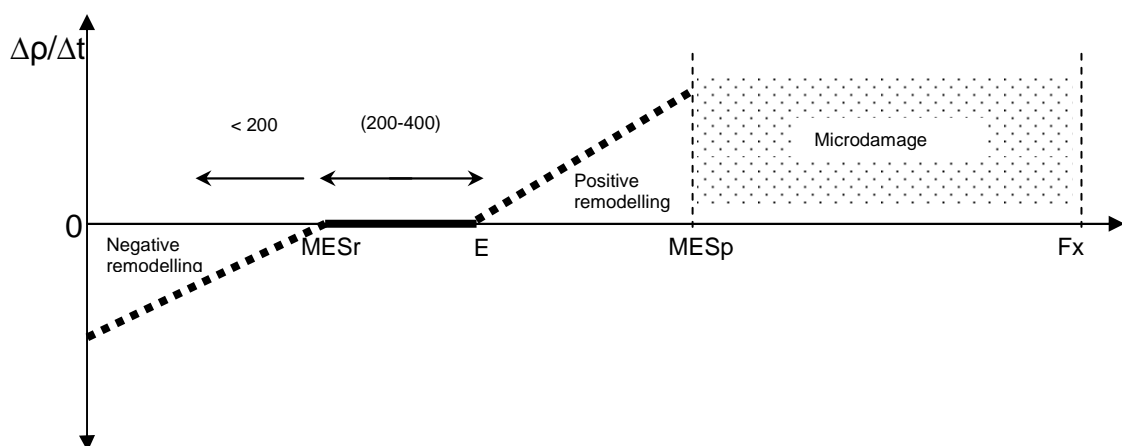

Figure 14: Stimulus thresholds, presented in με, in association with the remodelling regions.

As there is no change in bone density at the lower and upper critical stresses, where $U/\rho=k$ are assumed, and by substituting the lower critical stress σ_1 into Equation (16) and assuming a density of 1.74 g/cm^3 for cortical bone ρ_{cb} the constant k can be calculated:

$$\left|k^*\right|=\frac{\sigma_1^2}{2C\rho_{cb}^4},$$ (18)

and the constant D, by substituting the upper critical stress σ_2 into Equation (13):

$$\left|D\right|=\frac{2C\rho_{cb}^4 B}{\sigma_2^2-2C\rho_{cb}^4 k^*}.$$ (19)

Accordingly, the given value for constant k was 0.0004 Jg^{-1}, whereas the given value for constant D was 19.48 (gcm^{-3})^{3}MPa^{-2}(time unit)$^{-1}$. k was calculated with the strain magnitude of 325 $\mu\varepsilon$ taking the dead zone into consideration.

3.2.2. Sensitivity Test of the Applied Theory

To fully exploit its potential, the mathematical model for bone remodelling was implemented into the commercial FE software Marc Mentat. The bone was considered to be an isotropic and homogeneous material with Young's modulus of E_{co}=20,000 MPa for the cortical bone and E_{sp}=300 MPa for cancellous bone. Poisson's ratio was 0.3.

In this study a 3D FE model of an Ankylos A11 (Ø 3.5 mm, L11 mm) dental implant inserted in an idealised bone model with 1.5 mm cortical thickness was used to test the implemented algorithm. The simulation describes the remodelling process of the bone around the dental implant after full osseointegration to exclude the numerical influence of contact analysis on the implemented simulation. The daily load history was represented using a load case of an axial force of 100 N applied on the implant and face load of 2 MPa

as a fixed pressure on the outer periphery of the cortical bone to simulate the effect of jaw flexure. Density changes were observed after 100 cycles. After calculating the SED and stress fields in the initial isotropic, homogenous model for each bone element, the density was adapted to the observed SED and stress, respectively. Using the remodelling theory, the effective stress was used to calculate the actual daily stimulus U/ρ. The difference between the actual (daily) stimulus and the attractor state stimulus k provides the error signal that derives the remodelling response, generating a value for the rate of density change for each element. The apparent density of each element was then updated based on Equation (17) and the Young's modulus of each element was calculated as a cubic power function of the new apparent density (Equation 15). The new values of the material properties of each element were implemented in the next time increment and subsequent increments were analysed similarly. Bone elements were considered to be converged when the rate of density change is less than 10^{-5} between the iterations.

To optimise the applicability of the developed simulation, the sensitivity to various mechanical conditions was tested. These included:

1.   Different element size.

2.   Various boundary conditions of the surrounding bone including different constrain areas and degrees of freedom, in addition to the modification in the direction and magnitude of the applied load on the dental implant.

3.   Applying the suggested remodelling parameters based on Mechanostat theory and the corresponding dead zone width.

4.   Modification of the stiffness of the cancellous bone.

5.   Modification of the thickness of the cortical bone.

6.   Different implant geometries.

3.2.2.1.   Sensitivity Test: Element Size

In order to explore the influence of the element size on the behaviour of the implemented simulation, the test model was developed with numerous element edge lengths (EELs), namely: 0.2, 0.3, 0.4, 0.6, 0.8 mm.

Homogenous element size from bone periphery to the implant-bone interface was considered.

In this analytical part, the bone was considered to be an isotropic homogenous material with E_{co}=20,000 MPa and E_{sp}=300 MPa. Remodelling parameters were: k=0.0001 Jg^{-1}, D=55.00 (gcm^{-3})^{3}MPa^{-2}(time unit)$^{-1}$, and B=1.0 (gcm^{-3})^{2}MPa^{-1}(time unit)$^{-1}$, w was 20% of the threshold stimulus k and the implant was loaded with a vertical force of 100 N. The values of the remodelling parameters were used as suggested by *Li et al.* (2007). A constant face load of 2 N on the periphery of cortical bone and end faces was applied. The bone was constrained in the lower most part (Figure 15).
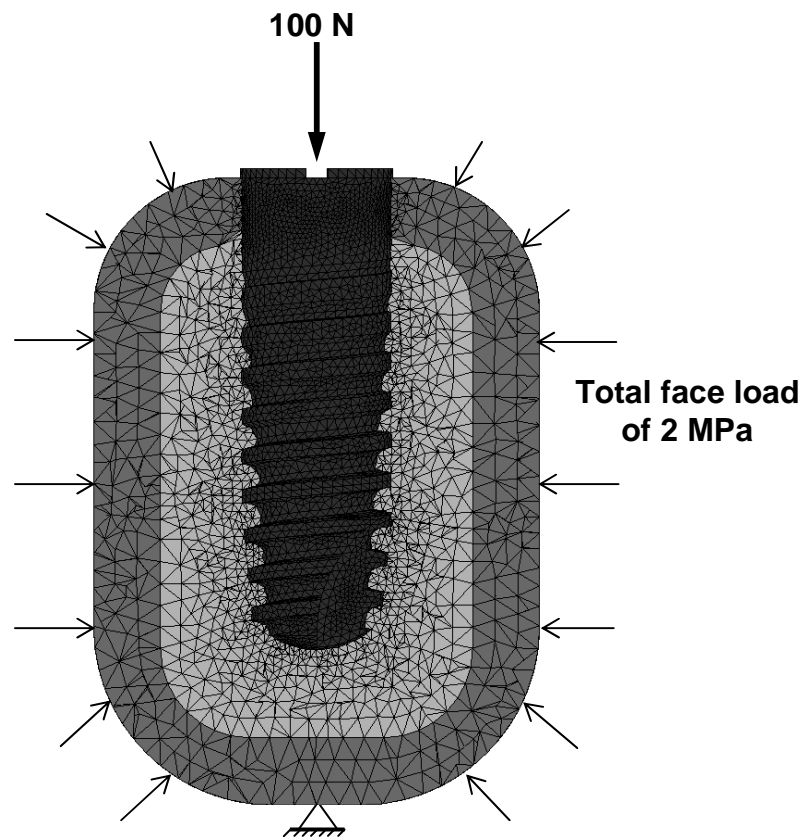

Figure 15: Boundary conditions that were used for testing the simulation with different element sizes. The presented model was meshed with EEL of 0.6 mm.

3.2.2.2.   Sensitivity Test: Boundary Conditions

In order to obtain optimal results of the remodelling simulation, different boundary conditions concerning surrounding bone were explored as follows:

1.   Constrain the end faces of the bone in three degrees of freedom.

2.   Constrain the end faces in axial direction.

3.   Facial load on the outer periphery of cortical bone as compression, keeping the end faces constrained in three degrees of freedom.

4.   Facial load on the outer periphery of cortical bone as well as the end faces as compression or tension.

5.   To simulate the action of jaw muscles in function, face load was applied on one half of the outer periphery of cortical bone as compression and as tension on the second half to represent the contraction and extension status of muscles. The end faces were constrained in three degrees of freedom.

The magnitude of the load applied in 3., 4., and 5. was selected in such a way that the resultant stress in the bone was within the boundary of the assumed half width of the dead zone w (20% of the threshold stimulus k). The selected values were: 0.5, 0.7, 1.0, 1.5, 2.0, and 2.5 MPa.

For this part, models with EEL of 0.4 mm and 0.6 mm were chosen because of the acceptable distribution of density by means of elements on one hand, and the total time required to calculate the density after 100 steps on the other hand. Material properties and remodelling parameters were identical to those used in 3.1.2.1. The implant was loaded with a vertical force of 100 N.

3.2.2.3.   Sensitivity Test: Applying Remodelling Parameters based on Mechanostat Theory

As described in section 3.2.1., the physiological strains are within the range of 200 to 4,000 με, accordingly the parameters k and D were calculated by considering the lower critical stress to be 5.2 MPa (Equation 18) and the upper critical stress 60 MPa (Equation 19), respectively. The half width of the dead zone w was considered as 60% of the reference stimulus k, correspondingly; no remodelling takes place within the stress range of 2.0–8.3

MPa within the cortical bone and 0.1–0.5 MPa within the cancellous bone (the stress was calculated considering Young's modulus of 20 GPa for the cortical bone and 500 MPa for the cancellous bone). The given value for constant k was: 0.0004 Jg^{-1}, D: 19.48 (gcm^{-3})^{3}MPa^{-2}(time unit)$^{-1}$ and B: 1.0 (gcm^{-3})^{2}MPa^{-1}(time unit)$^{-1}$.

Cortical bone was subjected to a tension load of 4.0 MPa on one half and compression load of 3.0 MPa on the other half keeping the end faces constrained in three degrees of freedom. The implant was loaded with a vertical force of 300 N.

3.2.2.4.   Sensitivity Test: Implant Loading Conditions

Three loading conditions were applied to test the remodelling model:
1.   Axial loads of 150, 200, 250, 300 N.
2.   Transverse loads with the same magnitudes described in the point above.
3.   Combined axial (150-300 N) and transverse (20 N) loads.

3.2.2.5.   Sensitivity Test: Cancellous Bone Stiffness

Different stiffness values of cancellous bone were considered starting from a very dense bone represented by a stiffness of 800 MPa to a very soft bone of 100 MPa.

3.2.2.6.   Sensitivity Test: Elastic Modulus-Density Relation

Up to now the elastic modulus was calculated according to the correlation suggested by *Carter and Hayes* (1977), where the modulus is proportional to the apparent density raised to the power of 3 (Equation 15). As an attempt to apply the different remodelling activities of the cortical and cancellous bone and their influence on the stability of the obtained density per element, the bilinear constitutive relationship suggested by *Orr et al.* (1990) was applied:

$$E= \begin{cases} 2{,}014\rho^{2.5} & \text{if} \quad \rho \le 1.2 \dfrac{g}{cm^3} \; , \\[2em] 1{,}763\rho^{3.2} & \text{if} \quad \rho > 1.2 \dfrac{g}{cm^3} \; . \end{cases} \qquad (20)$$

The modified relation was tested by applying two loading cases: First, an axial load of 100 N on the implant and second, with 300 N. Compression and tension face load of 0.3 and 0.7 MPa were applied on the peripheries of the cortical bone. The selection of the magnitude of the face load was based, on one hand, upon achieving the daily stimulus that stimulates the remodelling process, and on other hand, keeping the final bone stress after reaching the equilibrium condition within the range suggested by *Koseki et al.* (2005).

3.2.2.7.   Sensitivity Test: Bone Qualities

To investigate the behaviour of the time-dependent density change with different bone qualities, four 3D FE models were developed, as follows:

1.   Quality 1: 2.0 mm cortical bone of E_{co}=20 GPa surrounds a trabecular core of E_{sp}=10 GPa.

2.   Quality 2: 1.5 mm cortical bone of E_{co}=20 GPa surrounds a trabecular core of E_{sp}=7 GPa.

3.   Quality 3: 1.0 mm cortical bone of E_{co}=20 GPa surrounds a trabecular core of E_{sp}=300 MPa.

4.   Quality 4: 0.5 mm cortical bone of E_{co}=20 GPa surrounds a trabecular core of E_{sp}=100 MPa.

3.2.2.8.   Sensitivity Test: Implant Geometry

Two implant geometries were selected to test the simulation: Ankylos[®] A11 (Ø 3.5, L 11 mm) and tioLgic[©] (Ø 3.3, L 11 mm). Figure 16 demonstrates the macrogeometry of the two used implants. The remodelling parameters and boundary conditions used in 3.2.2.4., 3.2.2.5., 3.2.2.6., 3.2.2.7., and 3.2.2.8. were similar to that applied in 3.2.2.3.
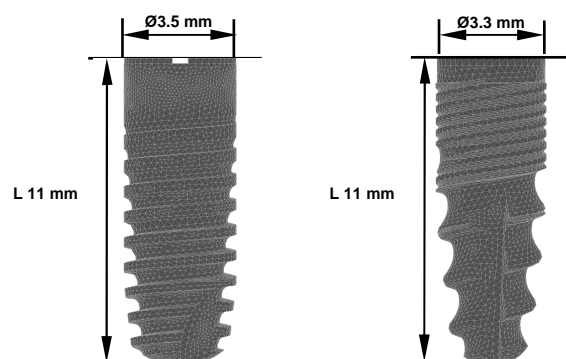
Figure 16: Implant geometries that were used in testing remodelling simulation: Ankylos® implant (left) and tioLgic© implant (right).

3.2.3. Validation of the Computational Trabecular Geometry around an Implant by Using 6-year CT-Images

To test the numerically obtained trabecular structure around the dental implant, CT-images of a patient taken after six years from the implant insertion were used. The implant was inserted in the region of upper right first incisor as a part of implant-supported FPP with a bar system. The cortical thickness was calculated from the CT-program and the position of the implant in the jaw as well by measuring the distance between the implant and the neighbour implants-bone borders in the different directions.

A segmental FE model of the anterior maxilla was developed. The dimensions of the bone segment were created according to the defined values from the CT-images (Figure 17). The numerical model consisted of an approximately 1.0 mm thick cortical layer (Young's modulus of 20,000 MPa) surrounding a core of cancellous bone (Young's modulus of 300 MPa). The implant was loaded by inciso-palatal forces of 60 N and 20 N, respectively (Helkimo et al., 1977). The end faces were fixed in three degrees of freedom. Cortical bone elements, except those at the cervical region, were excluded from the remodelling routine, as the cortical bone in these regions shows merely apparent changes after the placement of implants.

After running the remodelling simulation for 100 time steps, the distribution of elements by means of the change in apparent density were studied and compared to the bone structure in the CT-images.
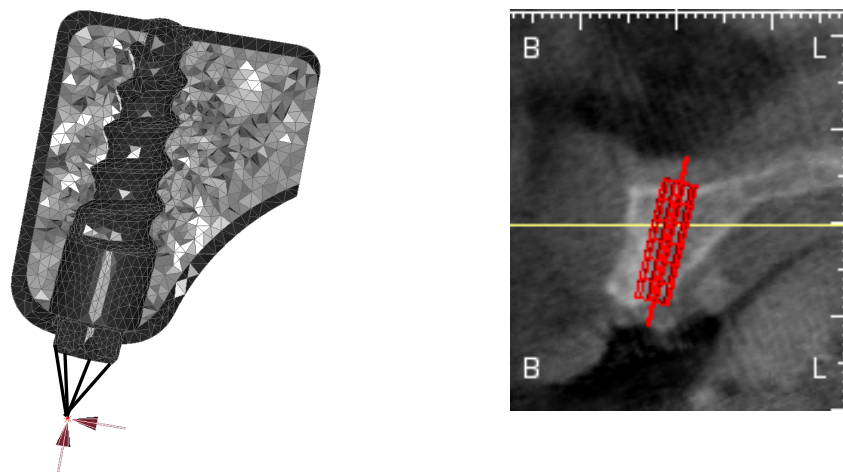
Figure 17: FE model of the maxillary bone segment with the dental implant (left), and the CT-image (right, later view). The slice thickness was 0.7 to 1.0 mm, with the preplanned position of the implant. For the FE model, the load was applied at the height level of the final restoration.

3.2.4. Influence of Soft Tissue Thickness on Bone Remodelling Simulation

To go a step forward in the investigation of the bone remodelling model, the behaviour of the bone elements by means of stress distribution and density change per unit time was studied by applying a soft tissue layer at the bone-implant interface. This analysis was essential for studying the healing process of the bone around dental implants under immediate loading condition that will be discussed later on in this section.

The previous results concerning density distributions with different EELs (section 4.2.1.1.) showed obviously the influence of the element size on the density distribution of the bone elements. Consequently, 3D FE models were developed with different thicknesses of the soft tissue layer around the dental implant (Figure 18). Table 6 illustrates the EELs of bone elements and the corresponding thicknesses of the soft tissue that were used in this part of the analysis.

The mechanical conditions including implant loading, boundary conditions and material properties were identical to those used in sections 3.2.2.3. to 3.2.2.8. Soft tissue elements that surround the implant within the cortical and cancellous bone zones were given the material properties of the cortical and

cancellous bone, respectively, i.e. the unique variation in the idealised model was adding the soft tissue layer that disturbs the homogeneous element size of the bone elements.
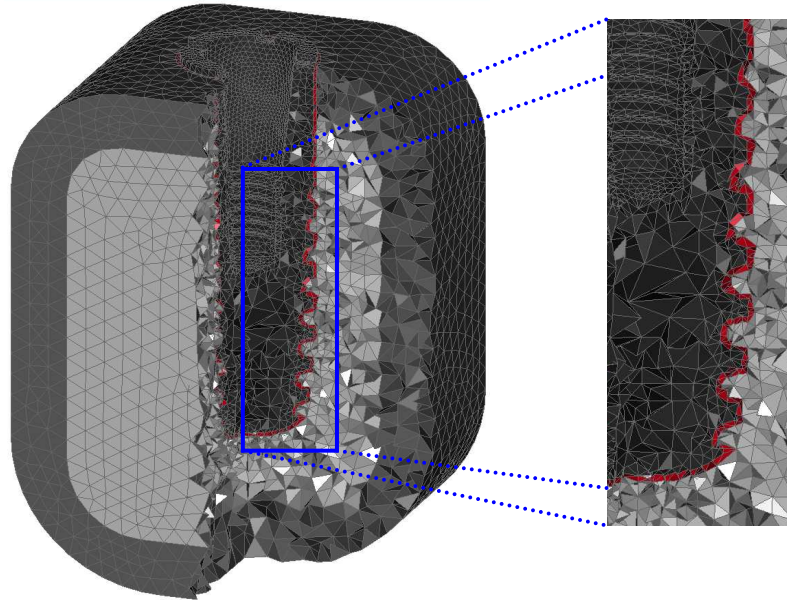
Figure 18: 3D FE model that describes the situation immediately after the insertion of the implant into the bone presented with 100 µm thick soft tissue layer around the implant.

Table 6: Element edge lengths EELs and soft tissue thicknesses that were used to develop the EF models.

*The soft tissue thickness of 400 µm and 600 µm are too far away from the realistic clinical situation immediately after the insertion of the implant. These thicknesses were selected only to study whether the homogeneous element size is essential for the stability of the remodelling model.

	Soft tissue thickness		**Soft tissue thickness**
EEL: 0.4 mm	40 µm	EEL: 0.6 mm	40 µm
	60 µm		60 µm
	80 µm		80 µm
	100 µm		100 µm
	200 µm		200 µm
	400 µm*		600 µm

3.2.4.1.   Remodelling Model Including Soft Tissue Interface

After obtaining the trabecular structure around the dental implant by running the simulation for implant model in osseointegrated condition, the response of the remodelling model during the healing phase after immediate implant loading was studied with the presence of tissue layer(s).

The 60 μm thick connective tissue (CT) was chosen to go further on in studying the advanced phases of the healing process (Cochran et al., 1998). This was implemented by dividing the 60 μm into three layers: Intermediate stiffness callus (MSC), soft callus (SOC) and CT, in the direction from bone to implant, respectively. This represents the situation after two months from implant insertion. Finally, a third model was developed, in which the 60 μm layer included three sub-layers of stiff callus (SC), MSC and SOC, from bone to implant, respectively. This case represents the condition after four months from the implantation.

In the current part, no contact condition was considered between the implant and the soft tissue(s). The remodelling model is illustrated in Figure 19. Material properties of the different tissues are presented in Table 7.

3.2.4.2.   Finite Element Models of Different Healing Phases

In order to reflect the remodelling process of the bone around the implant within different healing periods after immediate loading, three 3D FE models were developed. Each model represents one specific healing stage (Claes and Heigele, 1999): The first model reflects the healing foundation within the first two weeks of implantation/immediate loading. The second and third models represent the 8th and 16th healing weeks, respectively. Figure 20a describes schematically the implant-bone interface filled with the different callus tissues throughout the different healing stages.

Tissue differentiation and gradual stiffening of the callus tissue are the fundamental processes of secondary fracture healing. These processes were simulated by changing the element material properties from one stage to the next. Material properties that were used for the FE models are listed in Table 7.

FE model with connective tissue interface at the implant surface

Original FE model

Solver

Solver

SED and effective σ of cortical and spongy bone

SED and effective σ of cortical and spongy bone

Remodelling algorithm to obtain trabecular structure around the implant

Element integration

ρ_0

$$S = \frac{\sigma^2}{2C\rho_n^4}$$

$$\dot{\rho} = B(S-K)$$

$$\rho_{n+1}^* = \rho_n + \Delta t\, f(\sigma, \rho_n)$$
$$\rho_{n+1} = \rho_n + \frac{1}{2}\Delta t\left[f(\sigma, \rho_n) + f(\sigma, \rho_{n+1}^*)\right]$$

$$\int_1^n \rho$$

$$E_{n+1}$$

Solver
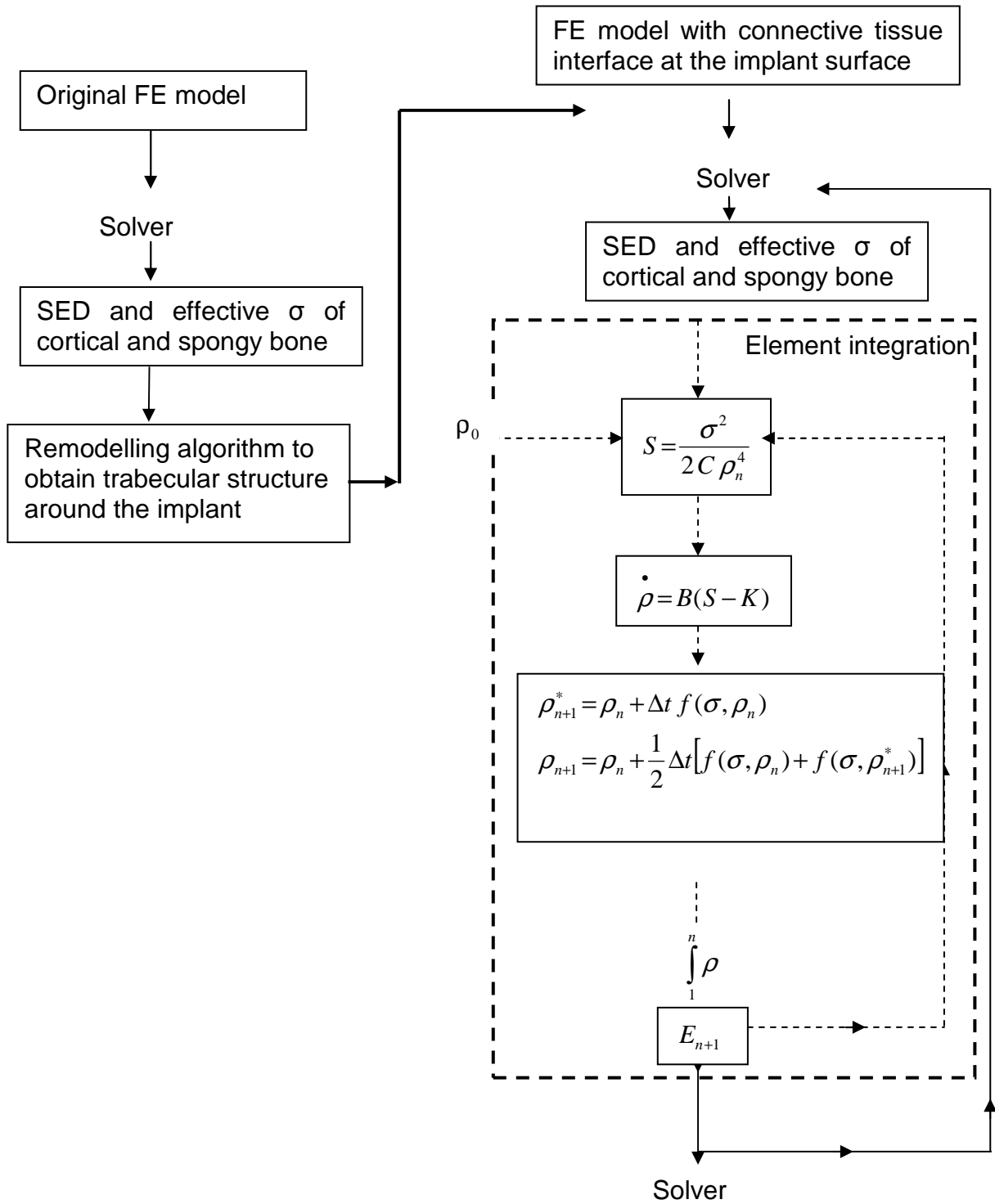
Figure 19: A block diagram of the algorithm with the soft tissue interface.

Table 7: Material properties of the FE models.

Material	Young's modulus (MPa)	Poisson's ratio
Initial connective tissue (CT)	1[*]	0.17[*]
Soft callus (SOC)	1,000	0.30
Intermediate stiffness callus (MSC)	6,000	0.30
Stiff callus (SC)	10,000	0.30

*(Jurvelin et al., 1997)

In the initial healing stage, the callus consisted only of initial CT (Figure 20a). The second model contained callus of MSC in a small region along the periosteum, and SOC adjacent to it, while the remainder consisted of CT (Figure 20b). In the third model the callus tissue contained three tissue types: SOC, MSC and SC (Figure 20c). Isotropic homogenous material behaviour was assumed for all tissue types.

3.2.4.3.   Radiographical Trabecular Structure at Different Healing Phases

To validate the numerical results concerning the trabecular distribution around the dental implant, Digital Volume Tomography (DVT) data of two patients were selected. The first patient received individual implant at the upper left canine region (23, tioLogic implant 3.7x13 mm), while the second patient received individual implant at the lower left first premolar region (34, tioLogic implant 3.7x11 mm). The bone quality was 2 for the maxilla and 3 for the mandible.

Bone foundation was documented before the operation, after one month and six months from the operation date as well (KODAK 9000 3D, Extraoral Imaging System). The analysis of the data were done using CeHaimPLANT software (med3D GmbH)
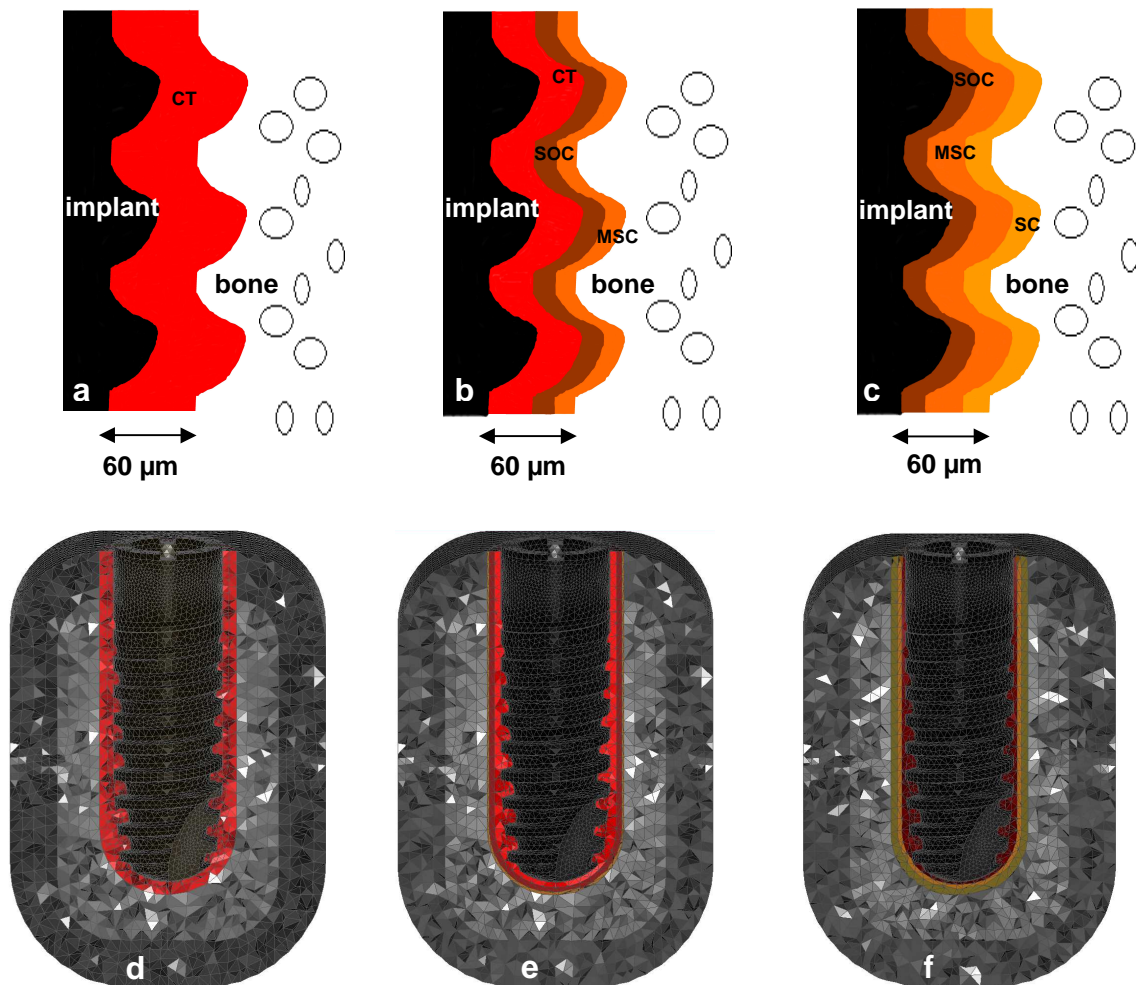
Figure 20: Schematic demonstration of the material properties of the callus tissues for the three modelled healing stages and the corresponding FE models: (a,d) After two weeks, (b, e) after eight weeks and (c, f) after sixteen weeks.

Chapter 4

4. Results

This section covers the results of the main issues of this work as follows:
First, the results of the mechanical investigation of the abutment design influence on the reaction of the bone for FPP. Second, the results of the applied remodelling theory and the corresponding sensitivity analysis, thirdly; the application of the remodelling theory to a clinical case, and finally; the results of the remodelling simulation including soft tissue during the healing phase.

4.1. Mechanical Investigation of Different Implant and Abutment Designs: Experimental, Numerical and Clinical Aspects

In this section the experimental results concerning implant displacement and rotation under immediate loading are presented. Moreover, qualitative and quantitive analyses of stress and strain distributions that were associated with the use of straight or angled abutment will be presented, in addition to comparing the numerical results regarding implant displacements with those that were obtained from the experiments. Furthermore, the numerical results of investigating the effect of the abutment design on the distribution of the stress and strain in the alveolar bone around the implants used in implant-supported partial prosthesis are discussed. Finally, the obtained results of the clinical evaluation of cervical bone loss in implant-supported prosthesis after six and twelve months are presented together with their association with the abutment design.

4.1.1. Fixed Partial Prosthesis Models

4.1.1.1.   Immediately Loaded Condition

The magnitude of the obtained strains and equivalent von Mises stresses are summarised in Table 8. Both, straight- and angled-abutment models in which the abutment and the corresponding prosthesis unit were considered as one rigid piece showed almost the same stress magnitudes. On the other hand the angled-abutment model (AAM) showed a higher strain value (6,000 µε) than the straight-abutment model (SAM, 5,300 µε). The displacement of the supporting implants, calculated as the average of the displacement of the two fixtures, was higher with the angled abutment (4.0 µm) than with the straight one (3.4 µm).

The pattern of stress distribution associated with the AAM was, generally, spread over a wider area of the cortical bone surrounding the implants than with the straight abutments (Figures 21a and 21b). Strain distributions for both models were concentrated at the most upper coronal portion of the fixture within the cancellous bone and the coarse thread areas showed a noticeable wider distribution of the strain with the angled abutments than with the straight ones (Figures 22a and 22b). The maximum values were higher in models with contact analysis than in those without contact (Table 8).

4.1.1.2.   Osseointegrated Condition

In the completely osseointegrated case, a decrease in the magnitudes of the implant displacements, stresses and strains associated with SAM and AAM was observed as follows: For SAM the drop was 43%, 47% and 80% of the implant displacements, stress and strain and for AAM 61%, 42%, and 78% respectively (Table 9).

Compared with the non-osseointegrated situation, a tendency towards a more homogenous stress distribution around the coronal portion of the dental implant was observed (cortical bone region in Figures 23a and 23b). Furthermore, the strain was basically concentrated along the coarse threads at the distal sides and more in the apical direction (Figures 24a and 24b).

Table 8: Obtained values of the total strains and equivalent von Mises stresses of the four FPP models with a total applied force of 150 N.

*The abutment and the corresponding unit of the prosthesis were modelled as one part.

**The abutment and the corresponding unit of the prosthesis were modelled as two bodies in contact.

	SAM one piece*	AAM one piece	SAM contact**	AAM contact
Stress (MPa)	57.0	54.0	53.0	56.0
Strain (με)	5,300	6,000	5,600	6,300
Displacement (μm)	3.40	4.00	4.1	4.90

Table 9: Obtained values of the total strains, equivalent von Mises stresses and implant displacements of the four FPP models with a total applied force of 150 N in immediately loaded and osseointegrated conditions.

* imm: Implants in immediate loading case.

**osseo: Implants in osseointegrated case.

|	SAM-imm*	SAM-osseo**	AAM-imm	AAM-osseo
Stress (MPa)	57.0	30.0	54.0	31.0
Strain (με)	5,300	1,026	6,000	1,313
Displacement (μm)	3.40	1.95	4.00	1.60
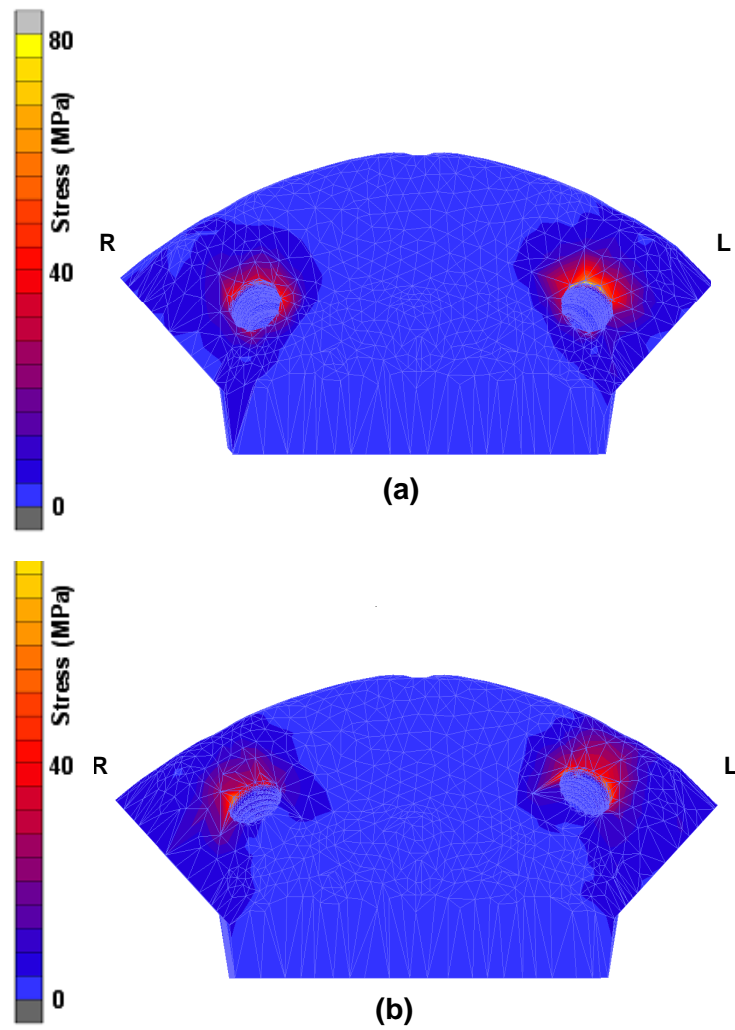
Figure 21: Occlusal views showing the distribution of the equivalent von Mises stresses within the bone surrounding the implants (immediately loaded case): (a) SAM and (b) AAM.

(a)

(b)
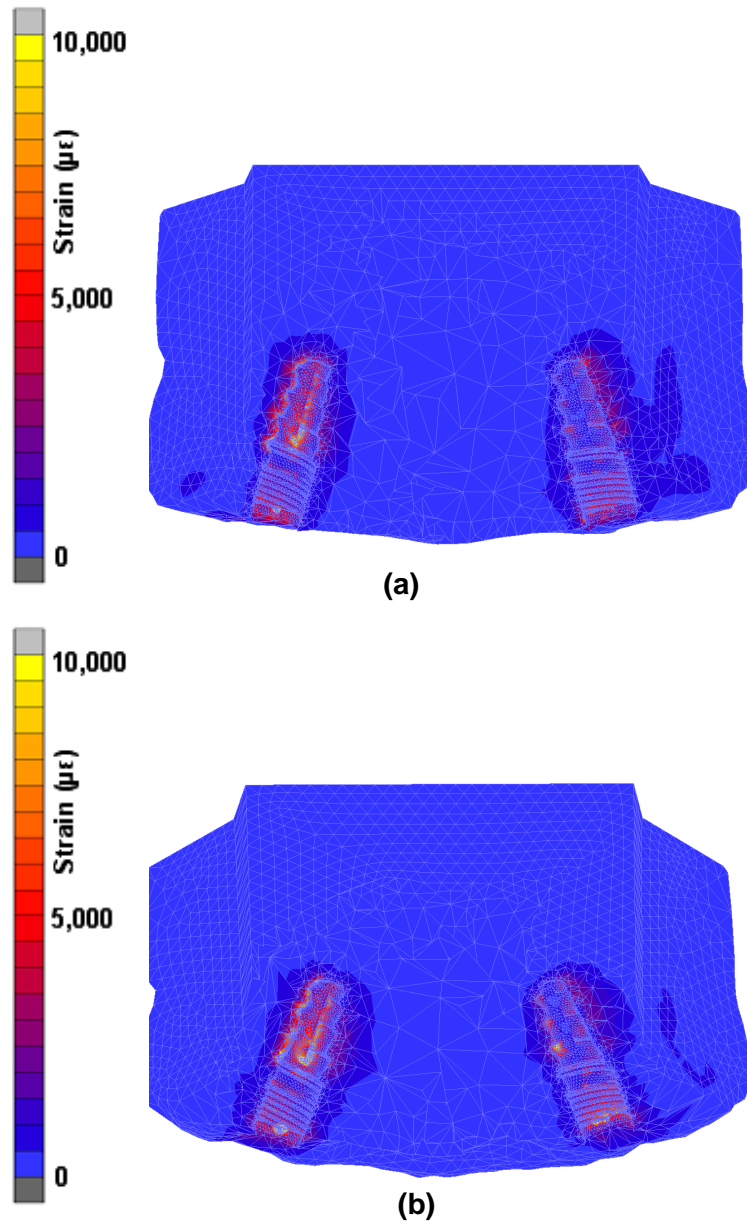
Figure 22: Palatal views showing the distribution of the total strains within the bone surrounding the implants (immediately loaded case): (a) SAM and (b) AAM.
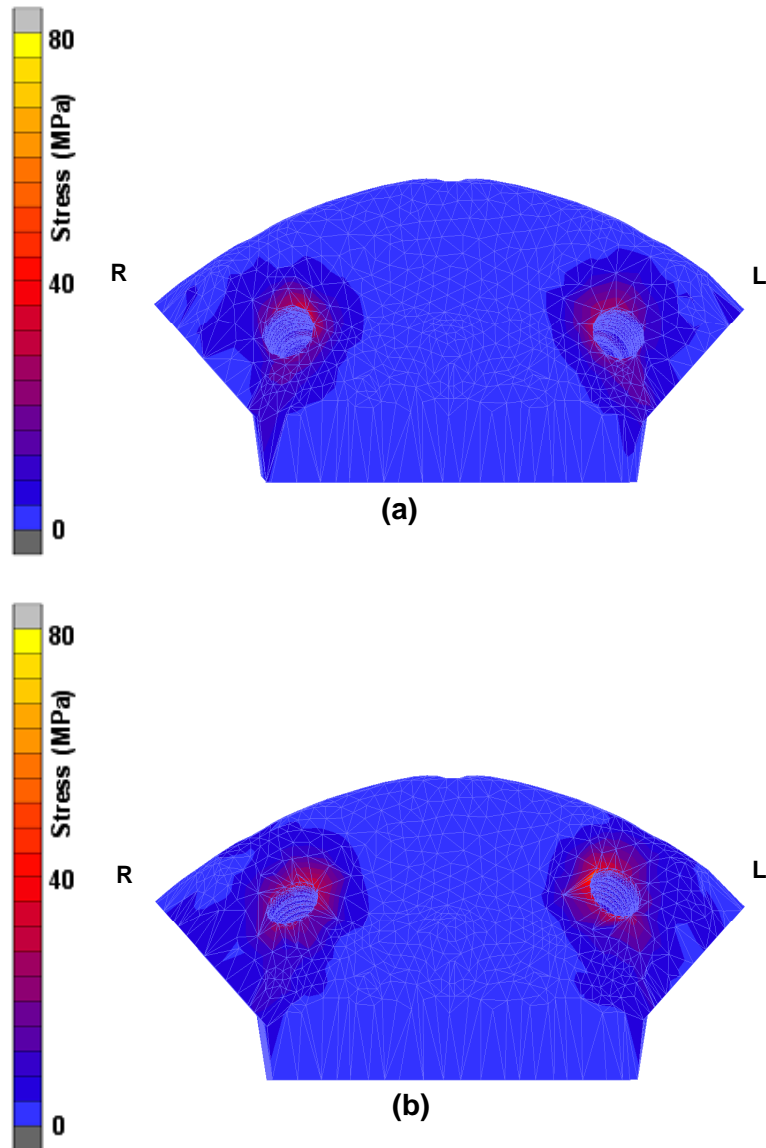
Figure 23: Occlusal views showing the distribution of the equivalent von Mises stresses within the bone surrounding the implants (osseointegrated case): (a) SAM and (b) AAM.
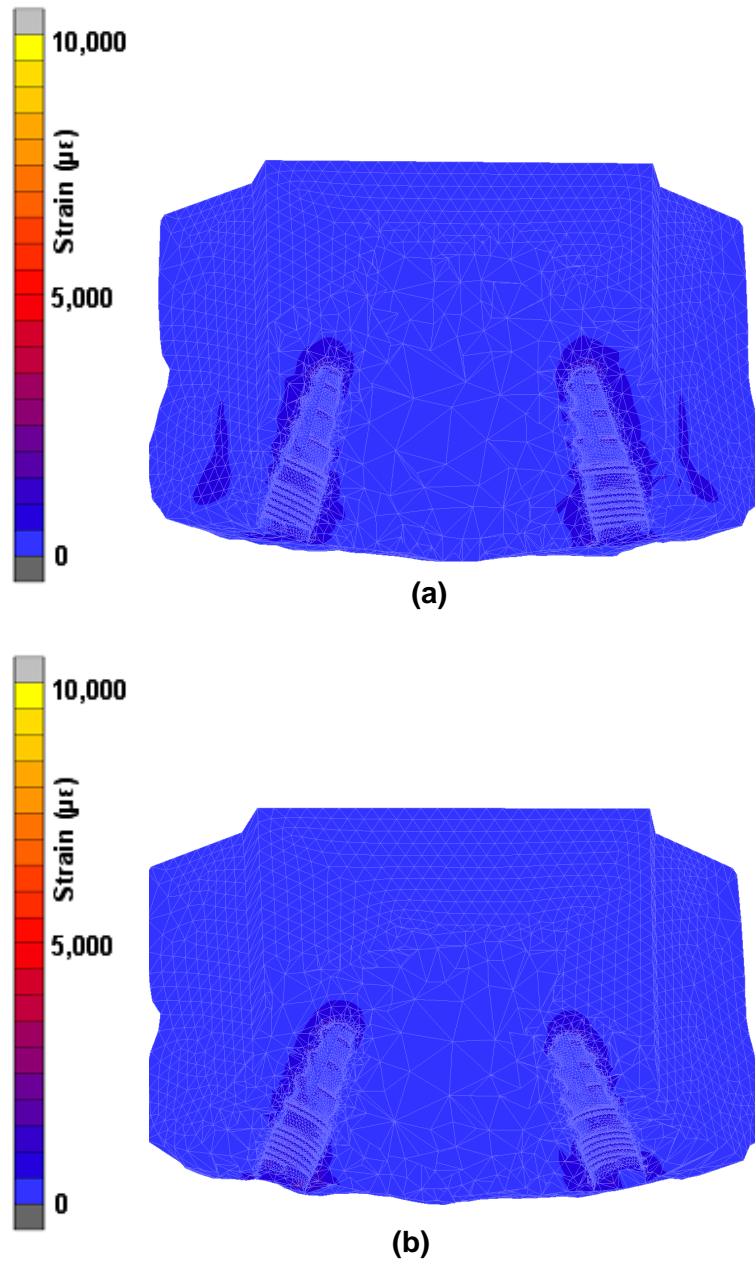
**Figure 24:** Palatal views showing the distribution of the total strains within the bone surrounding the implants (osseointegrated case). (a) SAM and (b) AAM.

4.1.2. Experimental Study of the Relation of Implant Primary Stability to the Implant Geometry and Abutment Design

22 specimens were finally selected for the evaluation of the primary stability. Eight specimens were considered as failure because of improper loading of the specimen resulting from improper positioning of the lever arm on the abutment.

Total distance of the hexapod's movement was selected to be within 0.5 to 1.5 mm, the resulting force applied by the loading unit was within 33 to 100 N. Correspondingly, measurements were analysed at a force of 40 N.

Displacements and rotations of implants in the following graphs are presented with the total force that was calculated from the components in x- and z-directions. For evaluation, a total force of 33 to 38 N, and implant displacement in x- and z-directions and rotation around y-axis were considered (Tables 10 and 11).

Table 10: Measured displacements and rotations of Tiolox$^{®}$ and tioLgic$^{©}$ implants with forces applied in x- and z-directions (i.e. palato-labial direction). The total applied force in (N) is presented below and displacements in (µm) in x- and z-directions and the rotation in (°) around the y-axis were considered. The measurements were done using straight abutments on which the forces have been applied.

*sx represents **s**traight abutment and Tiolo**x** implant.

sc represents **straight abutment and tioLgi**c** implant.

Tiolox$^{®}$ implants					tioLgic$^{©}$ implants				
	F_{total}	D_z	D_x	R_y		F_{total}	D_z	D_x	R_y
Sample 1sx*	33.4	41.7	170.2	2.2	Sample 1sc**	36.4	7.3	120.0	2.3
Sample 2sx	36.7	3.4	26.0	1.6	Sample 2sc	37.7	51.6	155.0	3.2
Sample 3sx	36.4	24.5	88.0	1.5	Sample 3sc	33.7	1.8	14.2	0.4
Sample 4sx	37.6	34.4	217.0	3.2	Sample 4sc	37.7	60.3	228.0	5.8
Sample 5sx	37.9	58.1	190.5	3.1	Sample 5sc	38.0	38.9	181.5	3.3
Sample 6sx	33.9	30.8	108.4	2.4	Sample 6sc	39.8	75.1	193.0	2.9
Sample 7sx	39.8	54.2	214.9	4.1	Sample 7sc	39.3	44.6	197.5	3.8
---------------	----	----	----	----	Sample 8sc	33.8	4.7	171.3	1.6

Implants with smooth cervical region (Tiolox[®]) showed higher displacements and rotation with the angled abutments (420 µm and 11°) than with the straight ones (390 µm and 8°, Figures 25 and 26). O n the contrary, implants with fine threads (tioLogic[©]) showed smaller displacements and rotation with the angled abutments (260 µm, 6.5°) than with the s traight ones (380 µm and 9°, Figures 27 and 28).
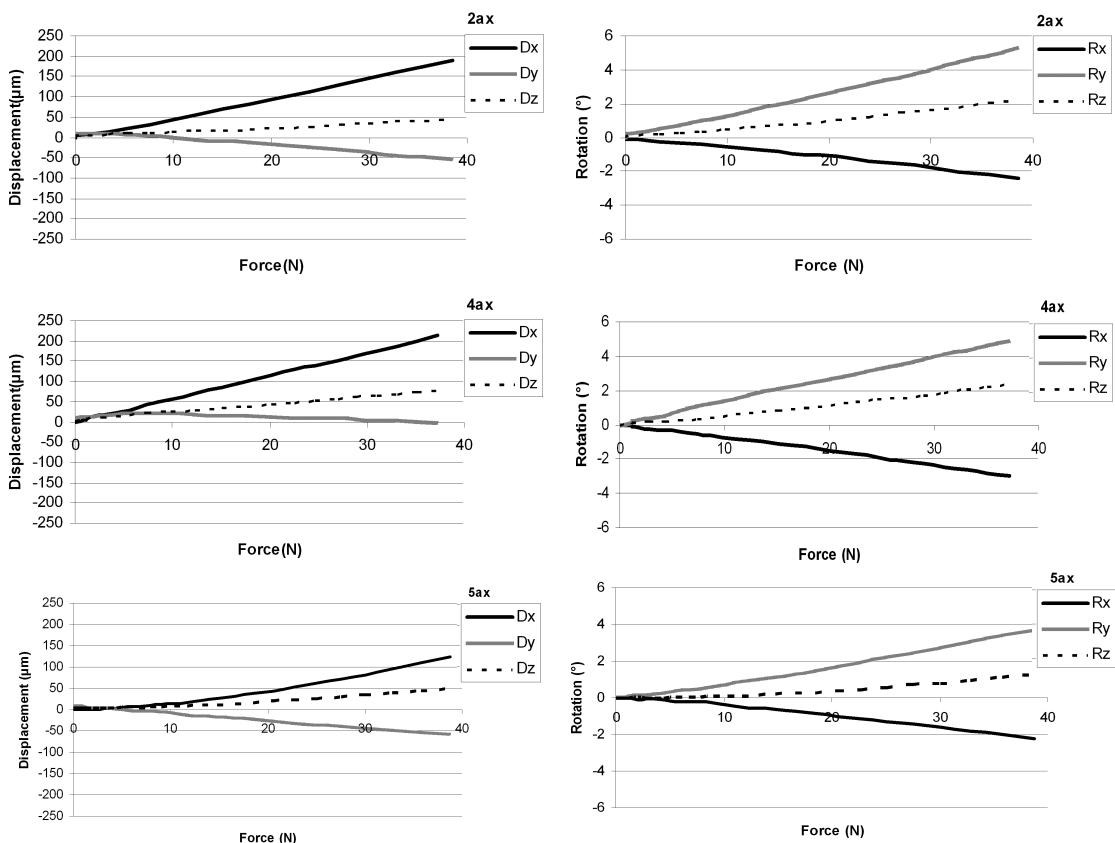
Figure 25: Displacement and rotation of Tiolox[®] implants connected to 20°-angled abutment in x, y, and z axes. The code 1ax represents the number of the sample followed by the type of the abutment used and finally the type of the implant (i.e. **1**[st] sample, **a**ngled abutment, Tiolo**x** implant).
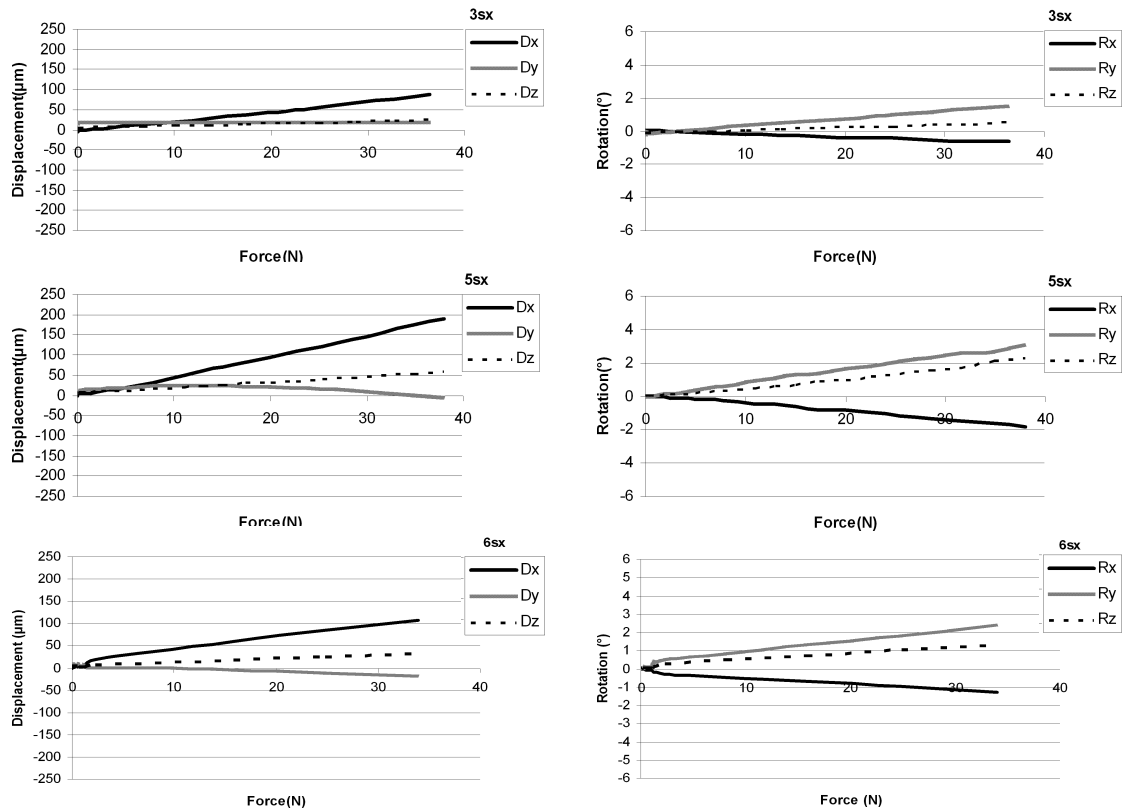
Figure 26: Displacement and rotation of Tiolox® implants connected to straight abutment in x, y, and z axes. The code 1sx represents the number of the sample followed by the type of the abutment used and finally the type of the implant (i.e. **1**st sample, **s**traight abutment, Tiolo**x** implant).
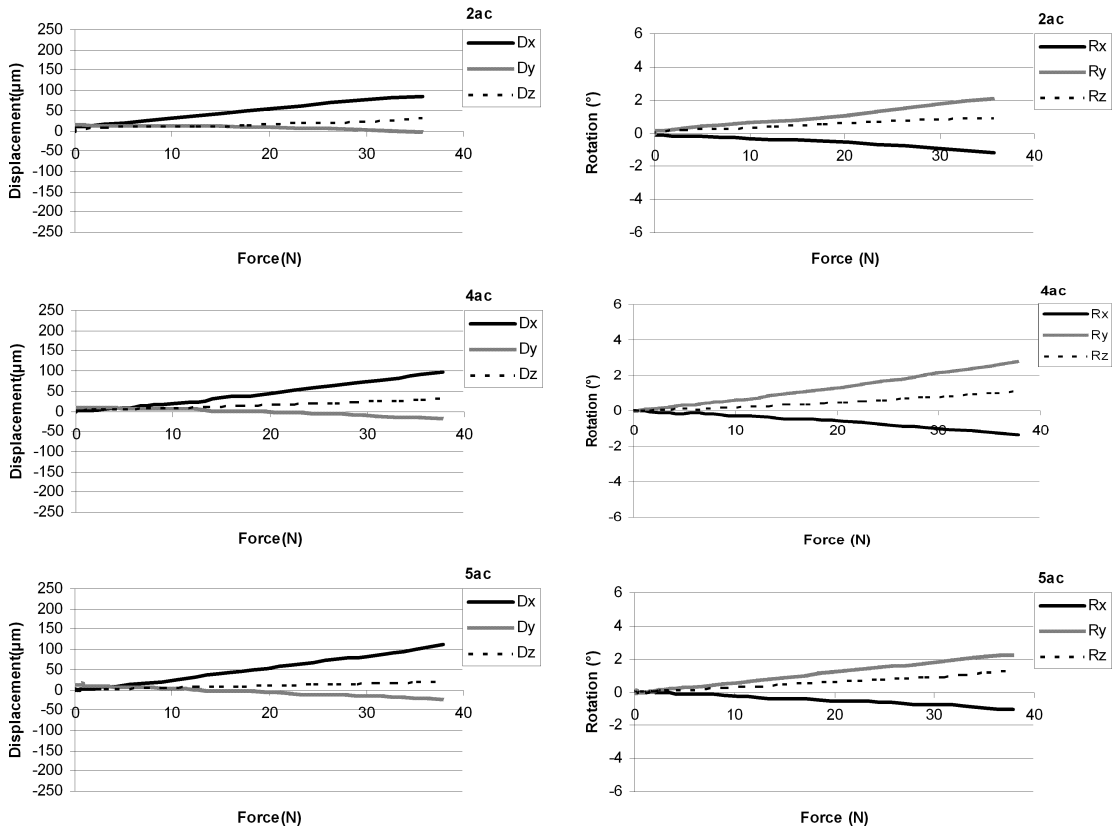
Figure 27: Displacement and rotation of tioLgic© implants connected to 20º-angled abutments in x, y, and z axes. The code 1ac represents the number of the sample followed by the type of the abutment used and finally the type of the implant (i.e. **1**st sample, **a**ngled abutment, tioLgi**c** implant).
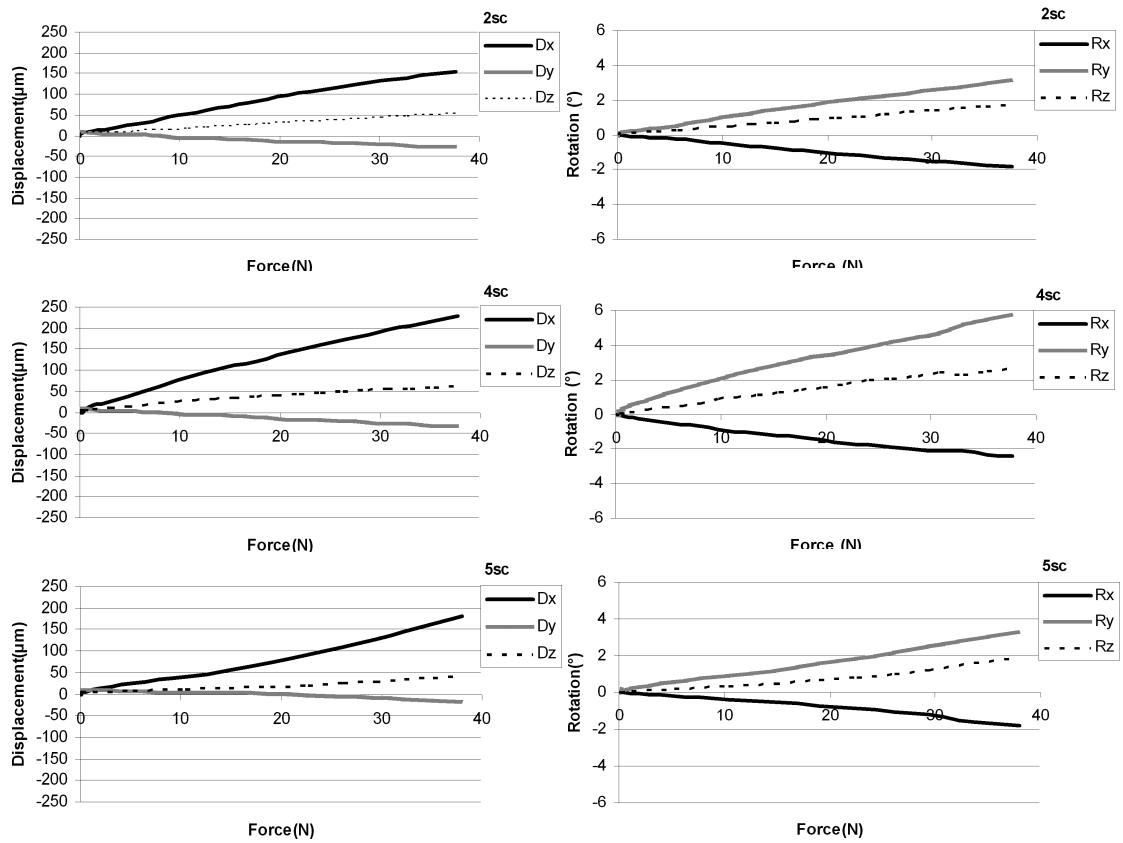
Figure 28: Displacement and rotation of tioLgic© implants connected to straight abutments in x, y, and z axes. The code 1sc represents the number of the sample followed by the type of the abutment used and finally the type of the implant (i.e. **1**st sample, **s**traight abutment, tioLgi**c** implant).

Table 11: Measured displacements and rotations of Tiolox® and tioLgic© implants with straight and angled abutments with forces applied in x- and z-directions. The components of the force in (N) in both directions are presented below. Displacements in (µm) only in x- and z-directions and rotation in (°) around y-axis are presented. The samples labelled in bold red were selected for the numerical analysis.

Tiolox® implants												
Straight abutments							**Angled abutments**					
	F_x	F_z	F_{total}	D_z	D_x	R_y		F_x	F_z	F_{total}	D_z	D_x	R_y
1sx*	12.2	31.2	33.4	41.7	170.2	2.2	1ax	9.1	36.9	38.0	6.9	76.8	2.1
2sx	10.2	35.3	36.7	3.4	26.0	1.6	**2ax**	**33.7**	**18.8**	**38.6**	**47.4**	**191.1**	**5.3**
3sx	**30.5**	**20.0**	**36.4**	**24.5**	**88.0**	**1.5**	3ax	13.2	11.7	18.0	39.5	78.2	1.4
4sx	34.3	15.5	37.6	34.4	217.0	3.2	**4ax**	**31.1**	**20.8**	**37.2**	**75.7**	**213.1**	**4.9**
5sx	**31.0**	**22.0**	**37.9**	**58.1**	**190.5**	**3.1**	5ax	31.7	22.4	38.7	48.0	124.7	3.7
6sx	31.7	12.2	33.9	30.8	108.4	2.4	6ax	28.6	22.8	36.6	83.7	328.1	4.5
7sx	33.2	22.1	39.8	54.2	214.9	4.1	7ax	33.3	20.7	39.0	35.9	136.9	3.1
------	------	------	------	------	------	------	------	------	------	------	------	------	------
tioLgic© implants												
Straight abutments							**Angled abutments**					
	F_x	F_z	F_{total}	D_z	D_x	R_y		F_x	F_z	F_{total}	D_z	D_x	R_y
1sc	13.5	33.9	36.4	7.3	120.0	2.3	1ac	21.9	28.7	36.0	25.3	43.1	1.4
2sc	**36.6**	**9.2**	**37.7**	**51.6**	**155.0**	**3.2**	**2ac**	**35.2**	**13.1**	**35.7**	**30.7**	**86.3**	**2.1**
3sc	9.6	32.5	33.7	1.8	14.2	0.4	3ac	31.6	18.4	36.6	32.2	122.9	2.6
4sc	36.4	10.2	37.7	60.3	228.0	5.8	**4ac**	**35.1**	**14.0**	**37.7**	**30.6**	**97.9**	**2.7**
5sc	**36.4**	**11.0**	**38.0**	**38.9**	**181.5**	**3.3**	5ac	35.7	13.1	37.8	21.7	111.0	2.3
6sc	34.9	19.5	39.8	75.1	193.0	2.9	6ac	35.6	16.4	38.6	61.4	167.7	2.8
7sc	32.0	23.2	39.3	44.4	197.5	3.8	7ac	32.7	20.4	38.4	47.9	146.2	3.2
8sc	26.9	20.8	33.8	4.7	171.3	1.6	8ac	14.6	16.1	21.7	20.7	114.1	1.9

4.1.2.1.   Numerical Results of Experimentally Studied Samples

Displacement of the nodes at the mid of the very upper layer of the abutment was considered in the evaluation and comparison of the experimental results. Maximum of total equivalent strain and equivalent stress were considered in the evaluation of the results presented below. Figures 7a and 7b show the calculated total implant displacement and rotation together with values obtained from the experiment at a force of 40 N for both implant systems.

Figure 29 shows the calculated total implant displacement and rotation together with those obtained from the experiment. The numerical linear increase of implant displacements with time coincides with the experimental behaviour of implant movement and was, in general, lower than those obtained experimentally. Table 12 shows the calculated implant displacement and rotation in their three components together with the corresponding experimental results.

The maximum equivalent stresses and strains were 34 to 39 MPa and 22,000 to 30,000 $\mu\varepsilon$ for Implants with smooth cervical region (Tiolox$^{®}$) with angled abutments and 40 to 55 MPa and 7,000 to 15,000 $\mu\varepsilon$ with straight abutments. Whereas the values for implants with fine threads (tioLogic$^{©}$) were 40 to 46 MPa and 18,000 to 21,000 $\mu\varepsilon$; and 42 to 49 MPa and 17,000 $\mu\varepsilon$, respectively (Table 13). Stresses were nearly the same for both implants with the two abutment designs, except for Tiolox$^{®}$ implants which showed less stress values with the angled abutments (Figure 30a). tioLogic$^{©}$ implants showed similar values for strains with straight and angled abutments. On the other hand, Tiolox$^{®}$ implants showed an obvious decrease in strains with straight instead of angled abutments (Figure 30b).
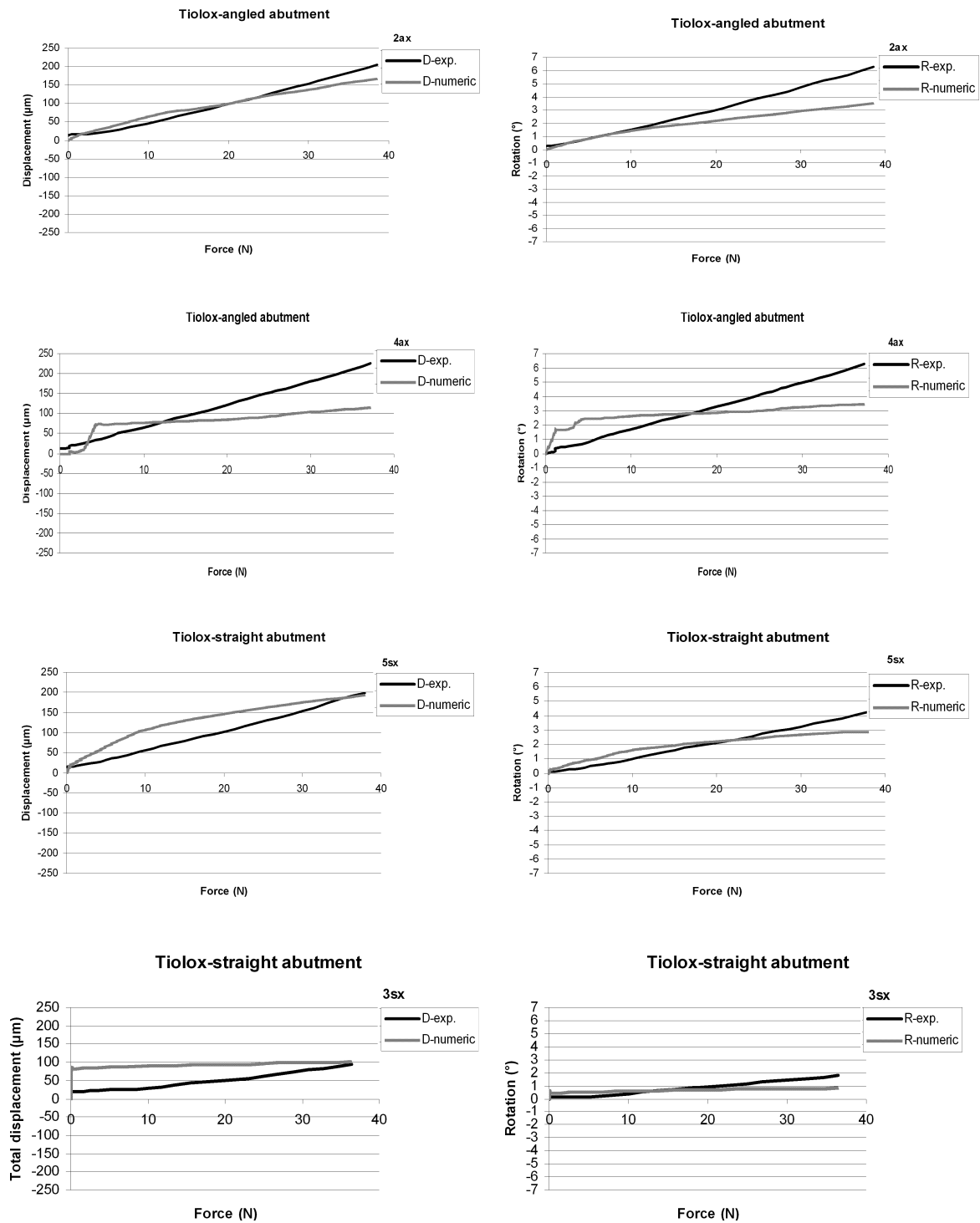
Figure 29a: Experimental and numerical total implant displacements and rotations of the selected eight specimens of Tiolox® implants.
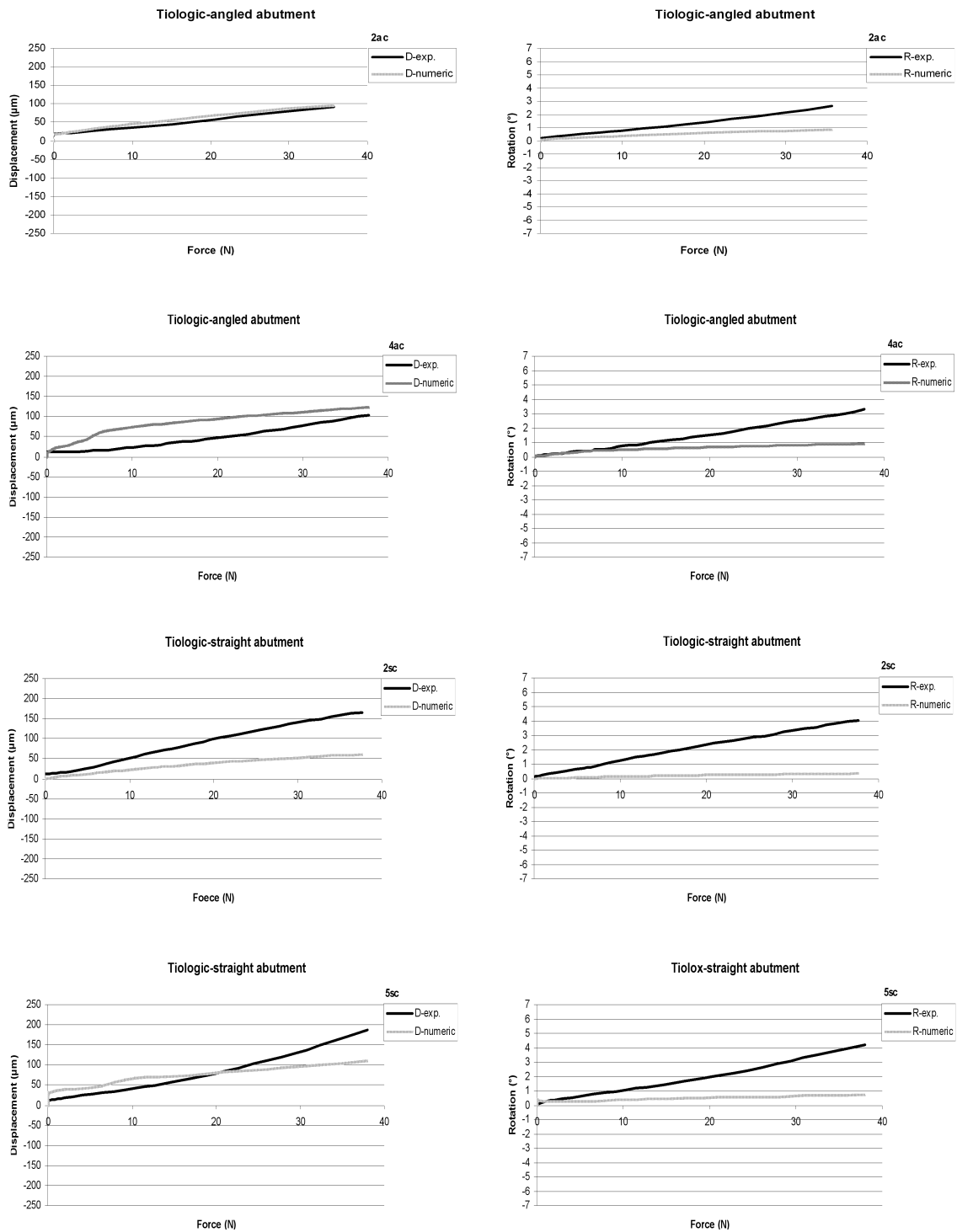
Figure 29b: Experimental and numerical total implant displacements and rotations of the selected eight specimens of tioLgic© implants.

Table 12: Numerical implant displacements (µm) and rotations (°) with the corresponding experimental values of the eight selected samples.

	Implant displacements						Implant rotations					
	D_x exp.	D_x num.	D_y exp.	D_y num.	D_z exp.	D_z num.	R_x exp.	R_x num.	R_y exp.	R_y num.	R_z exp.	R_z num.
3sx	88.0	100.9	18.5	18.5	24.5	5.6	0.6	0.1	1.5	0.7	0.5	0.5
5sx	190.5	188.5	3.5	42.3	58.1	13.2	1.8	0.6	3.1	2.9	2.2	0.4
2ax	191.1	160.0	53.8	20.0	47.4	40.0	2.4	0.3	5.3	2.8	2.1	2.1
4ax	213.1	64.9	1.3	93.7	75.7	8.1	2.9	0.5	4.9	2.3	2.4	2.5
2ac	86.3	90.0	2.9	40.0	30.7	20.0	1.2	0.9	2.1	0.4	0.9	0.7
4ac	97.9	120.0	16.2	0.9	30.6	18.0	1.3	0.1	2.7	0.5	1.1	0.7
2sc	155.0	61.8	25.5	2.7	51.6	9.0	1.8	0.3	3.2	0.4	1.7	0.5
5sc	181.5	109.0	15.6	7.0	38.9	12.5	1.8	0.4	3.3	0.5	1.8	0.5

Table 13: Calculated maximum values of Equivalent Total Stress and Strain in the bone around the implants for the eight selected specimens.

|	Stress (MPa)	Strain (µε)		Stress (MPa)	Strain (µε)
3sx	39.7	7,000	2sc	48.7	17,000
5sx	55.0	15,000	5sc	41.8	17,000
2ax	39.0	30,000	2ac	40.0	18,000
4ax	34.5	22,000	4ac	46.5	21,000
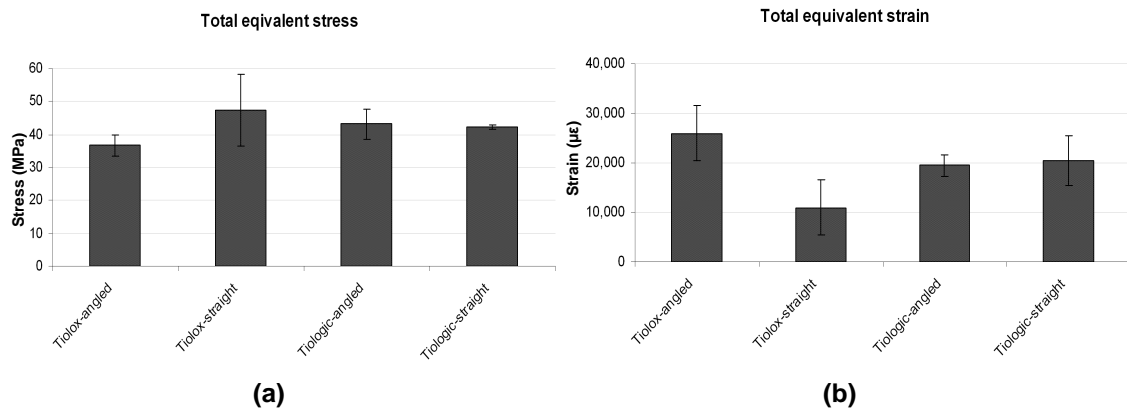
Figure 30: (a) Mean equivalent stresses and (b) mean equivalent total strains obtained from the numerical models of both implant systems with straight and angled abutments with a total force of 40 N.

4.1.3. The Relation of Crestal Bone Resorption to the Abutment Design Used with Implant-Supported Fixed Partial Prosthesis

4.1.3.1.   Statistical Analysis

Probing depths were statistically higher for the study subgroup with angled abutments in comparison to the control subgroup after six months and one year from the abutment insertion (P=0.0008 and P=0.01, respectively). The mean probing depth was 1.56 mm after six months and 1.70 mm after twelve months for the study subgroup with angled abutments and 1.00 mm and 1.30 mm for the control subgroup, respectively. A statistically significant decrease in probing depth for the control subgroup with angled abutments was noted in comparison to the control subgroup with straight abutments after six months and one year from the abutment insertion (P=0.003 and P=0.03, respectively).

The mean probing depth was 1.00 mm after six months and 1.30 mm after twelve months for the control subgroup with angled abutments and 1.50 mm and 1.6 mm for the control subgroup with straight abutments, respectively. However, no statistical significance was observed for the study subgroups with straight abutments and control subgroups with angled abutments (mean probing depth 1.7 mm, P=0.8 and P=0.4 for the probing depth after six months and one year).

Furthermore, no statistical significance was seen for the study subgroups with straight and angled abutments for both the measurement time points (mean probing depth 1.5 mm, *P*=0.8 and *P*=0.2 for the probing depth after six months and one year). Figure 31 presents the box diagrams of the mean probing depths of the study and control groups with straight and angled abutments for both measurement time points. An overview of the statistical significance can be seen in Table 14.
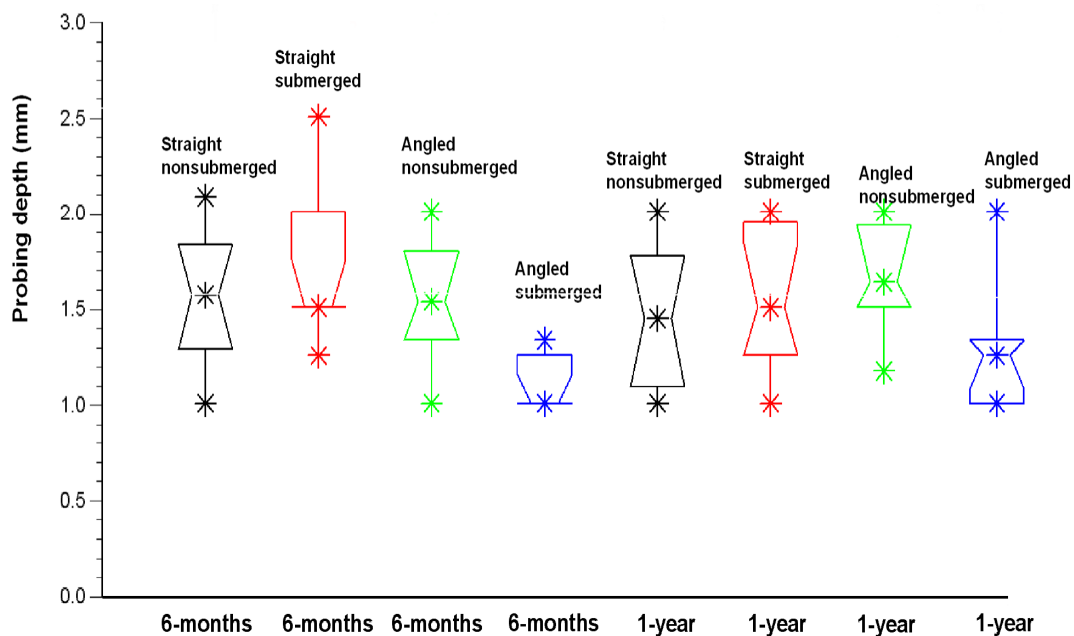
(a)

Figure 31a: Box diagram of the mean mesial probing depth for the study and control groups with the straight and angled abutments.

(b)

(c)
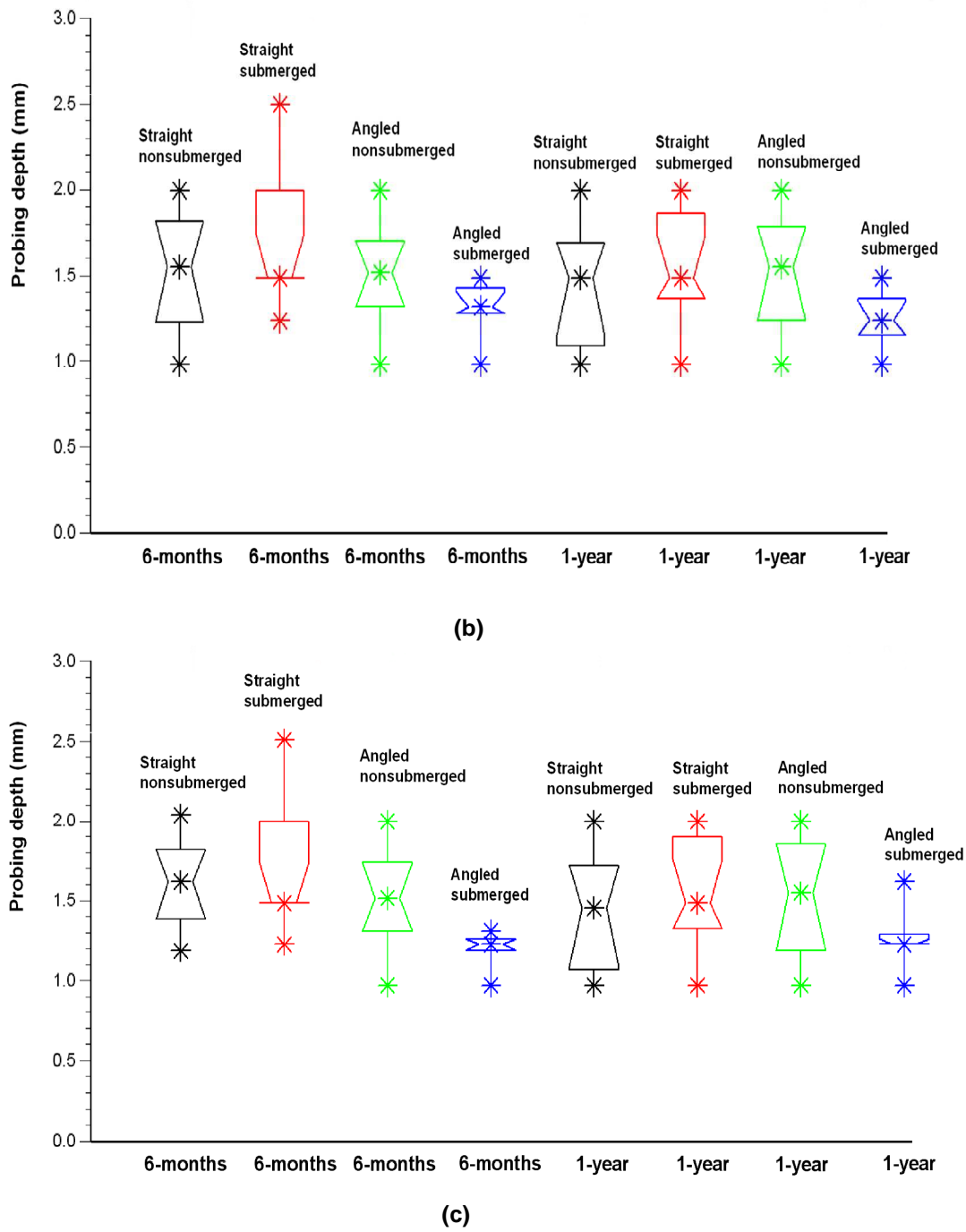
Figure 31 (cont.): Box diagrams of the mean probing depth for the study and control groups with the straight and angled abutments. (b) Probing depth measured distally, and (c) mean probing depth of the mesial and distal measurements.

Table 14: Probing depth significance level of the difference between the two abutment designs in nonsubmerged (study group) and submerged (control group) implant treatments at the 6th and 12th evaluation (Mann-Whitney test). The meaning of the signs below is as follows: (–) for $P > 0.05$ (not significant), (+) for $0.01 < P \le 0.05$, and (++) for $P \le 0.01$.

6-month

		Study group		Control group	
		Straight (N=36)	Angled (N=28)	Straight (N=20)	Angled (N=19)
Study group	Straight (N=36)			—	
	Angled (N=28)	—			++
Control group	Straight (N=20)				
	Angled (N=19)			++	

1-year

		Study group		Control group	
		Straight (N=36)	Angled (N=28)	Straight (N=24)	Angled (N=22)
Study group	Straight (N=36)			—	
	Angled (N=28)	—			+
Control group	Straight (N=24)				
	Angled (N=22)			+	

4.2. Bone Remodelling Theory

4.2.1. Sensitivity Test of the Applied Theory

In this part, the change in bone density by applying the developed remodelling model with different mechanical conditions are presented after 100 time steps. A 1 mm thick vertical slice through the mid of the implant and the surrounding bone was used to demonstrate the density distribution within the range of 0.4 to 1.74 g/cm^3.

4.2.1.1. Sensitivity Test: Element Size

Figure 32 (a-e) Illustrate the obtained bone densities with different EELs after 100 time steps. Only densities within the range of 0.4-1.74 g/cm^3 are presented below. Constant time step Δt of 10 (10^{-4} x time span) was selected. Small EEL showed very dense elements within the cancellous bone, while large EEL showed a minimal change in the density. The total time required to calculate the density changes after 100 time steps was: 60.30 hours., 17.30 hours., 9.30 hours, 6.00 hours, and 4.20 hours for the models with EEL 0.2, 0.3, 0.4, 0.6, and 0.8 mm, respectively.
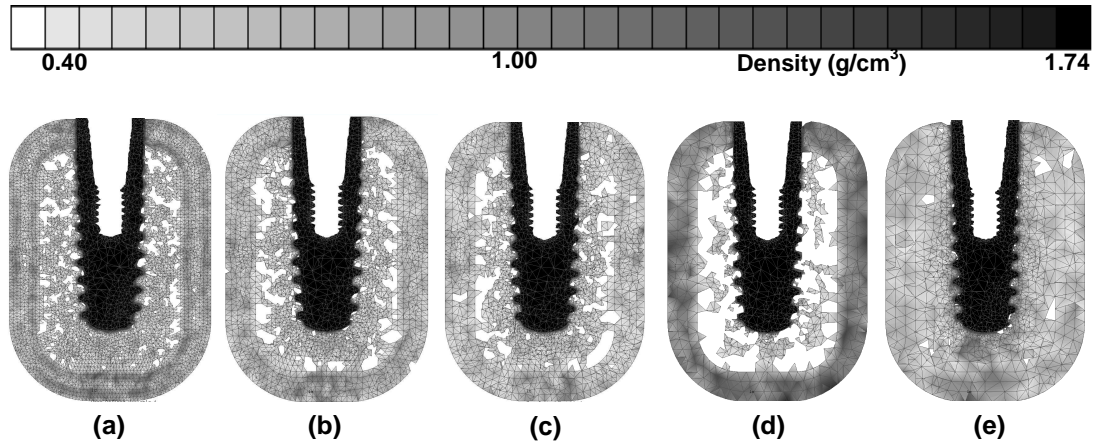
Figure 32: Longitudinal cross section of 1.0 mm thickness throughout the bone and associated implant part demonstrating density distribution of the bone elements around the implant after 100 time steps: With EEL (a) 0.2 mm, (b) 0.3 mm, (c) 0.4 mm, (d) 0.6 mm, and (e) 0.8 mm.

4.2.1.2.   Sensitivity Test: Boundary Conditions

The changes in the bone density with various boundary conditions are presented below in two different models: One model with EEL of 0.4 mm, and the second of 0.6 mm.

1.   Model Meshed with EEL of 0.4 mm

By fixing the cutting plane of the bone in three degrees of freedom or only in axial direction, the model showed unstable behaviour concerning the stress as well as the density per element. After 100 time steps almost all the elements had a density below 0.4 g/cm^3, i.e. below the density of the cancellous bone (Figure 33).
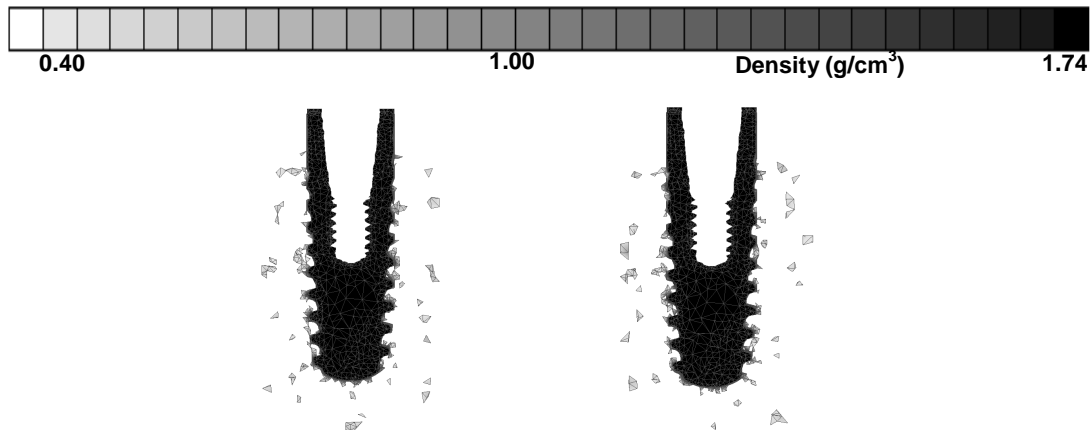
Figure 33: Densities obtained by fixing the cutting plane of the bone in three degrees of freedom (left) and in the axial direction (right) after 100 time steps.

The higher the load applied on the cortical bone peripheries, the more stable density distributions were obtained. This is observed with the gradual increase of the applied compressive load on the peripheries of the cortical bone (Figure 34 a-f). However, applying the compressive load all around the cortical bone including the end faces as well showed more stable behaviour of the elements, in particular within the cortical bone (Figure 35 a-f). Furthermore, a noticeable difference in the distribution of the density was obtained by converting the applied load on the bone from compressive to tensional one (Figure 36 a-f). Finally, almost all of the elements showed unstable behaviour by applying tension load on half of the peripheries of the cortical bone and compression load on the other half. The density was below 0.4 g/cm^3 (Figure 37 a-f).
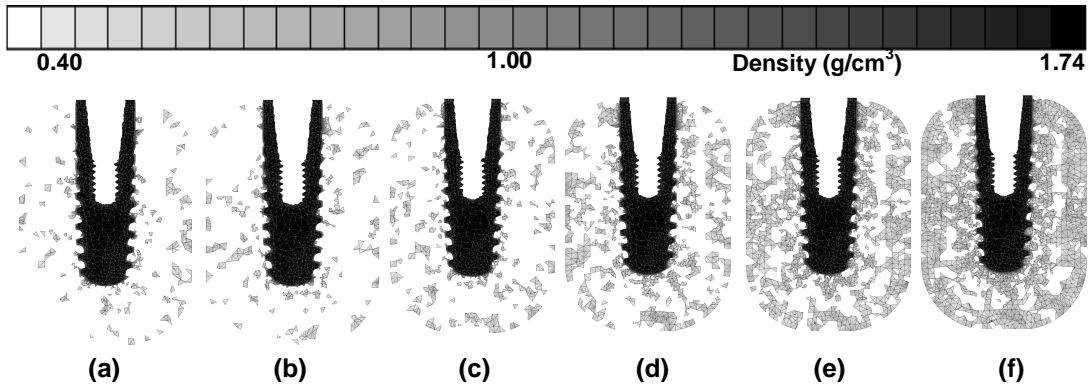
Figure 34: The densities obtained by applying compression face loads on the peripheries of the cortical bone keeping the end faces fixed in three degrees of freedom after 100 time steps: With (a) 0.5 MPa, (b) 0.7 MPa, (c) 1.0 MPa, (d) 1.5 MPa, (e) 2.0 MPa, and (f) 2.5 MPa.
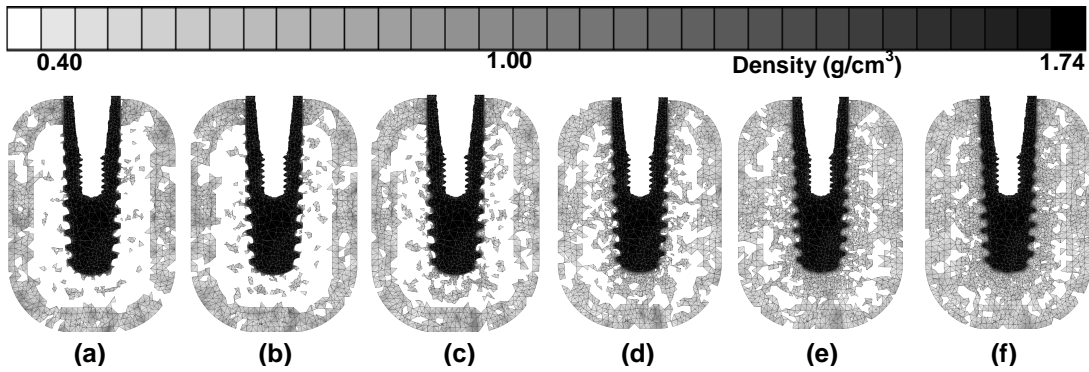

Figure 35: Densities obtained by applying compression face loads on the peripheries of the cortical bone and end faces as well after 100 time steps: With (a) 0.5 MPa, (b) 0.7 MPa, (c) 1.0 MPa, (d) 1.5 MPa, (e) 2.0 MPa, and (f) 2.5 MPa.
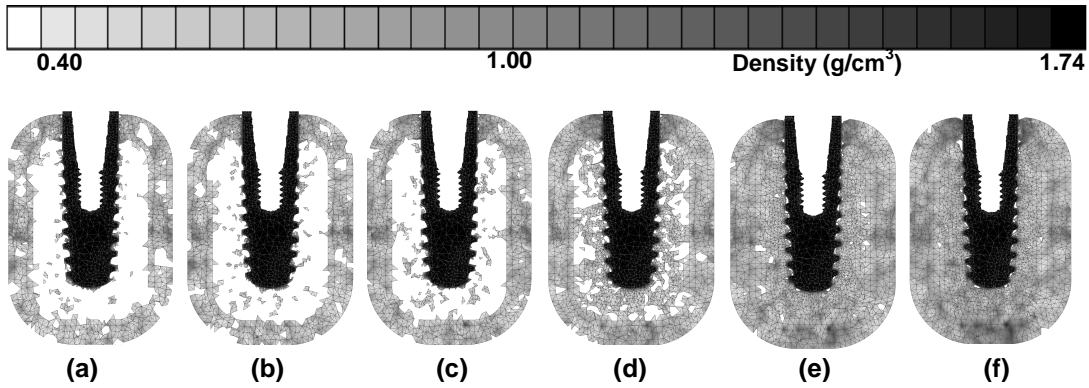
Figure 36: Densities obtained by applying tension face loads on the peripheries of the cortical bone and end faces as well after 100 time steps: With (a) 0.5 MPa, (b) 0.7 MPa, (c) 1.0 MPa, (d) 1.5 MPa, (e) 2.0 MPa, and (f) 2.5 MPa.
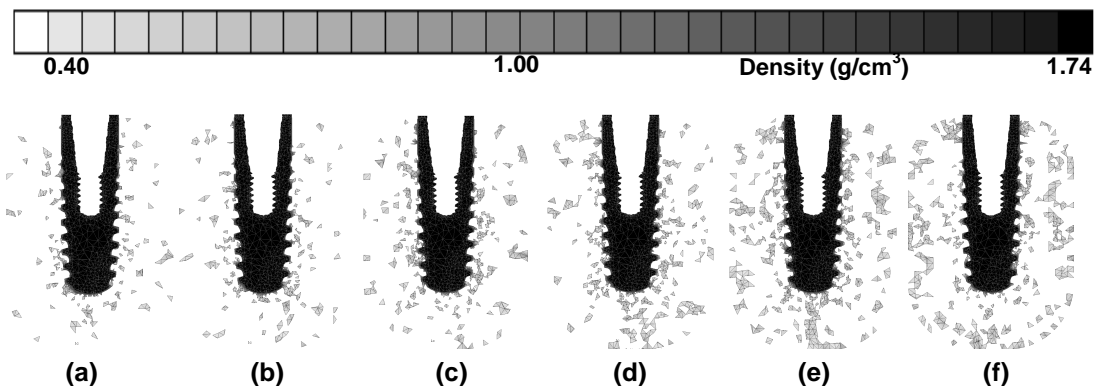

Figure 37: Densities obtained by applying tension face loads on one half of the peripheries of the cortical bone and compression loads on the other half keeping the cutting planes fixed in three degrees of freedom after 100 time steps: With (a) 0.5 MPa, (b) 0.7 MPa, (c) 1.0 MPa, (d) 1.5 MPa, (e) 2.0 MPa, and (f) 2.5 MPa.

2. Model Meshed with EEL of 0.6 mm

By fixing the cutting plane of the bone in three degrees of freedom or only in axial direction, the model showed unstable behaviour concerning the stress as well as the density per element. After 100 time steps most of the elements had a density below 0.4 g/cm^3, i.e. below the density of the cancellous bone (Figure 38). Anyhow, the results are slightly improved in comparison to those with EEL of 0.4 mm.
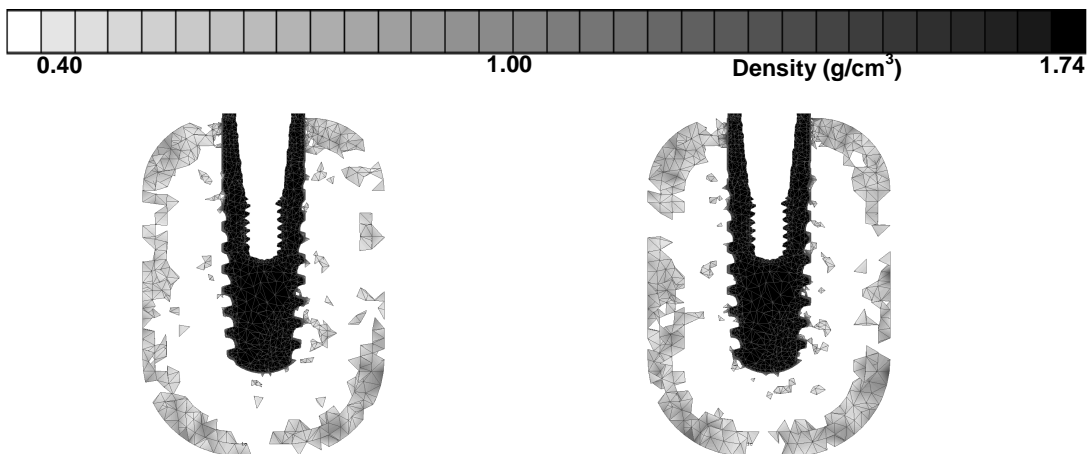

Figure 38: The densities obtained by fixing the cutting plane of the bone in three degrees of freedom (left) and in the axial direction (right) after 100 time steps.

The higher the load applied on the cortical bone peripheries, the more stable density distributions were obtained. This is observed by the gradual increase of the applied compressive load on the peripheries of the cortical bone (Figure 39 a-f). However, applying the compressive load all around the cortical bone including the end faces as well showed more stable behaviour of the elements, in particular within the cortical bone. In addition, a trabecular similar structure could be obtained with the compression load of 2.5 MPa (Figure 40 a-f). Furthermore, increasing the applied load as tension had an inverse effect on the density

distribution and element stability. Almost all of the elements showed a density below 0.4 g/cm³ when a tension load of 2.5 MPa was applied (Figure 41 a-f). Finally, the elements showed unstable behaviour by applying tension load on half of the peripheries of the cortical bone and compression load on the other half. The density was below 0.4 g/cm³ (Figure 42 a-f).

Stress distribution in the periphery of the cortical bone was evaluated for the models with compression-tension face load that represent the action of the jaw muscles. Figure 43 illustrates the obtained results for the six models.
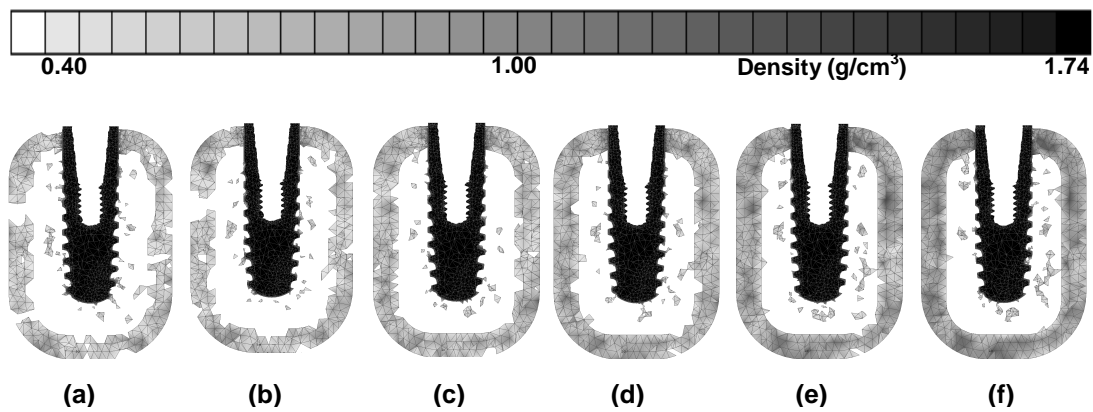

Figure 39: Densities obtained by applying compression face loads on the peripheries of the cortical bone keeping the end faces fixed in three degrees of freedom after 100 time steps: With (a) 0.5 MPa, (b) 0.7 MPa, (c) 1.0 MPa, (d) 1.5 MPa, (e) 2.0 MPa, and (f) 2.5 MPa.
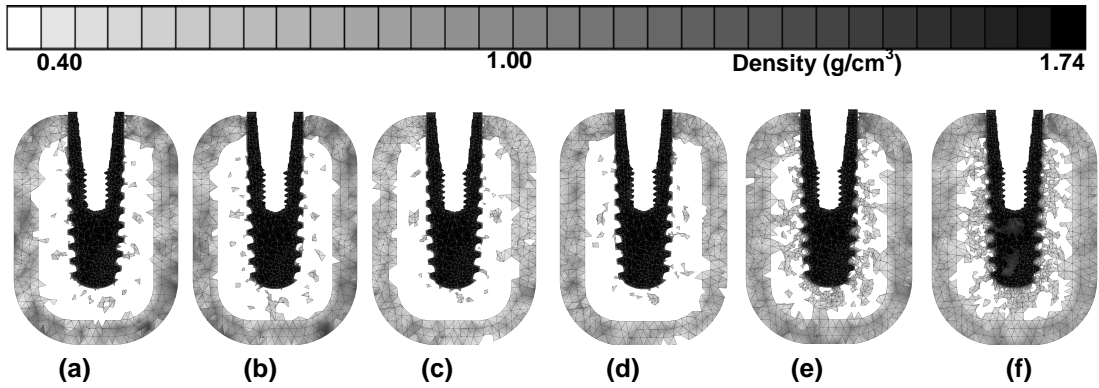
Figure 40: Densities obtained by applying compression face loads on the peripheries of the cortical bone and end faces as well after 100 time steps: With (a) 0.5 MPa, (b) 0.7 MPa, (c) 1.0 MPa, (d) 1.5 MPa, (e) 2.0 MPa, and (f) 2.5 MPa.
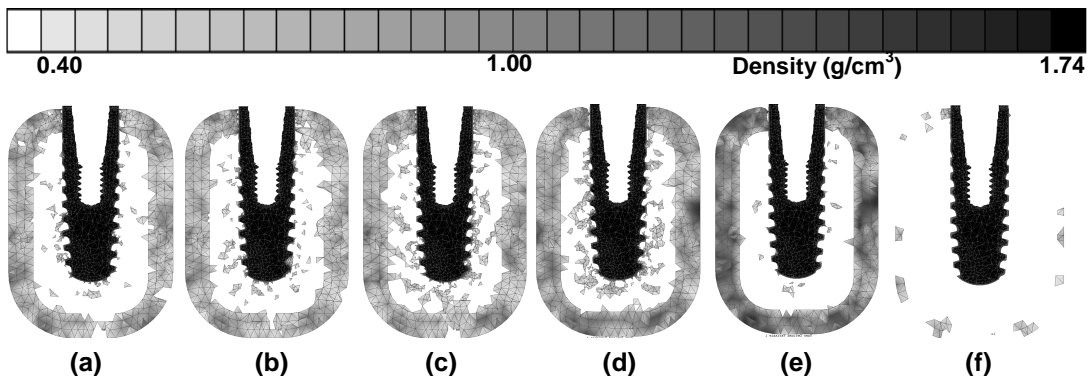
Figure 41: Densities obtained by applying tension face loads on the peripheries of the cortical bone and end faces as well after 100 time steps: With (a) 0.5 MPa, (b) 0.7 MPa, (c) 1.0 MPa, (d) 1.5 MPa, (e) 2.0 MPa, and (f) 2.5 MPa.
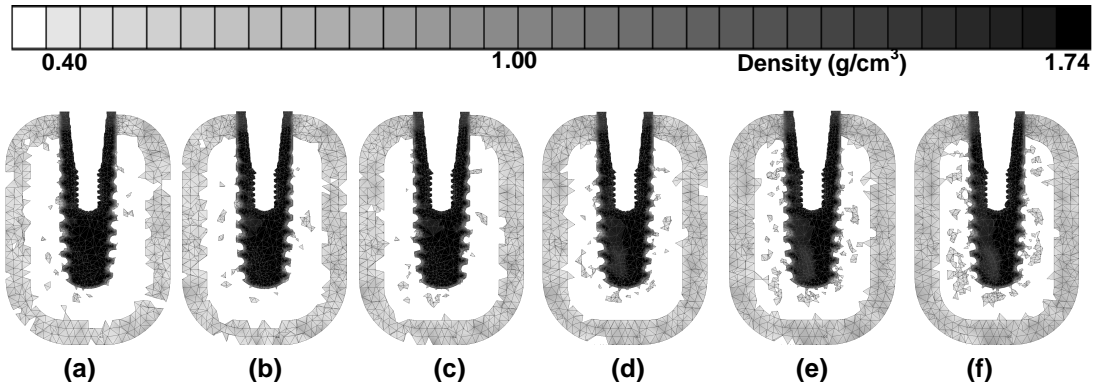
Figure 42: Densities obtained by applying tension face loads on half of the peripheries of the cortical bone and compression loads on the other half keeping the end faces fixed in three degrees of freedom after 100 time steps: With (a) 0.5 MPa, (b) 0.7 MPa, (c) 1.0 MPa, (d) 1.5 MPa, (e) 2.0 MPa, and (f) 2.5 MPa.
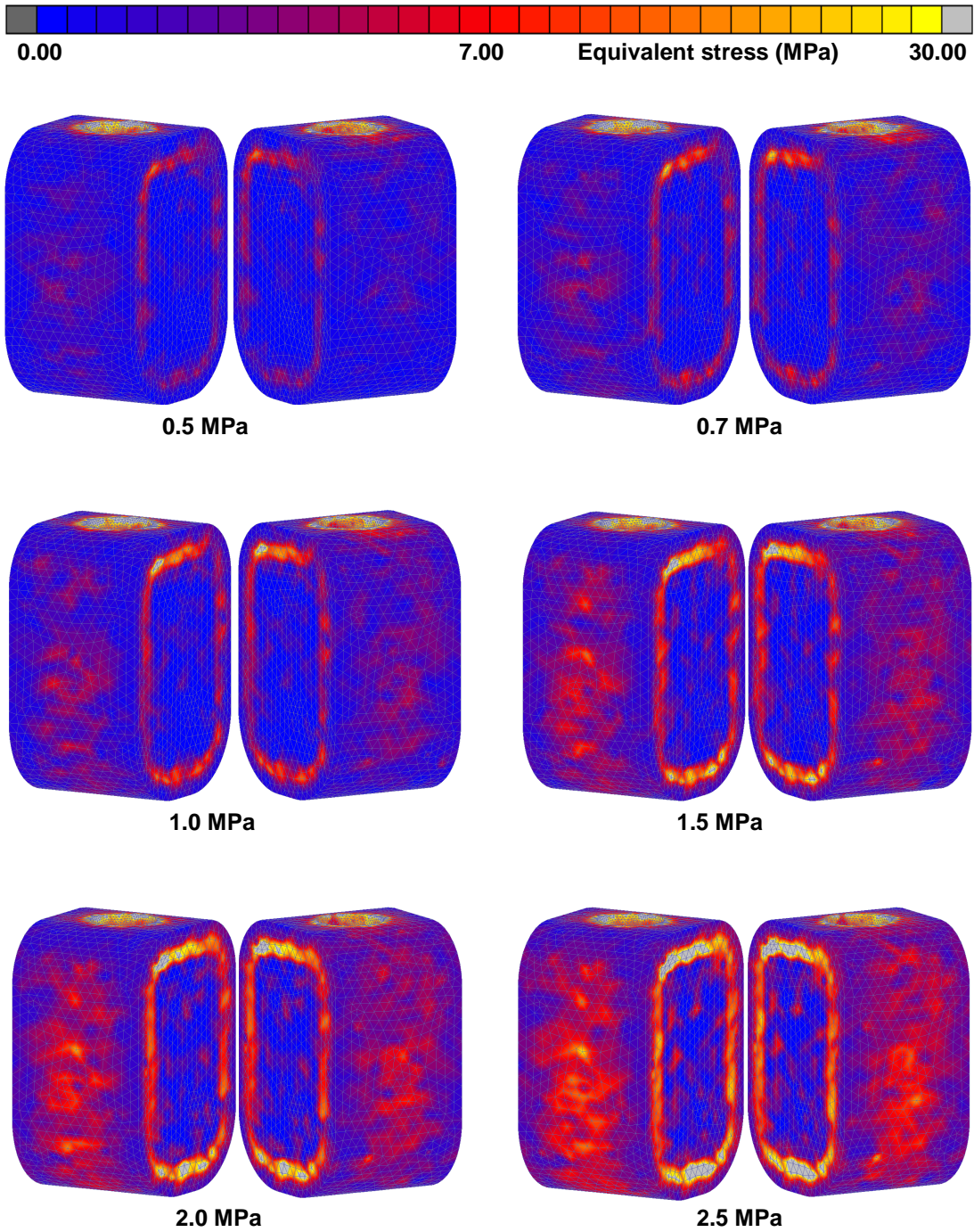
**Figure 43:** Stress distribution at the peripheries of the cortical bone on the push-loading (right of the coupled figures) and pull-loading (left of the coupled figures) sides.

In an attempt to reach the real situation of bone loading by the mastication muscles and achieve the suggested magnitude of the stress in the mandibular posterior region (Koseki et al., 2005), two models were developed. In the first, the peripheries of the cortical bone were subjected to a tension load of 2.5 MPa on one half and compression load of 1.5 MPa on the other half and the implant was loaded by vertical force of 100 N. The obtained equivalent stress was around 13 MPa on the tension side and around 6.0 MPa on the compression side.

In the second model, the peripheries of the cortical bone were subjected to a tension load of 4.0 MPa on one half and compression load of 3.0 MPa on the other half and the implant was loaded by vertical force of 300 N. The obtained equivalent stress was around 15 MPa on the tension side and around 8.0 MPa on the compression side. Figure 44 illustrates the obtained density and stress distributions after 100 time steps.

0.40　　　　**1.00**　　　**Density (g/cm^3)**　　**1.74**

Tension 2.5 MPa, compression 1.5 MPa, 100 N vertical force. Density distribution of the whole model (left), and in 1 mm vertical slice through the midline (right).

Tension 4.0 MPa, compression 3.0 MPa, 300 N vertical force. Density distribution of the whole model (left), and in 1 mm vertical slice through the midline (right).
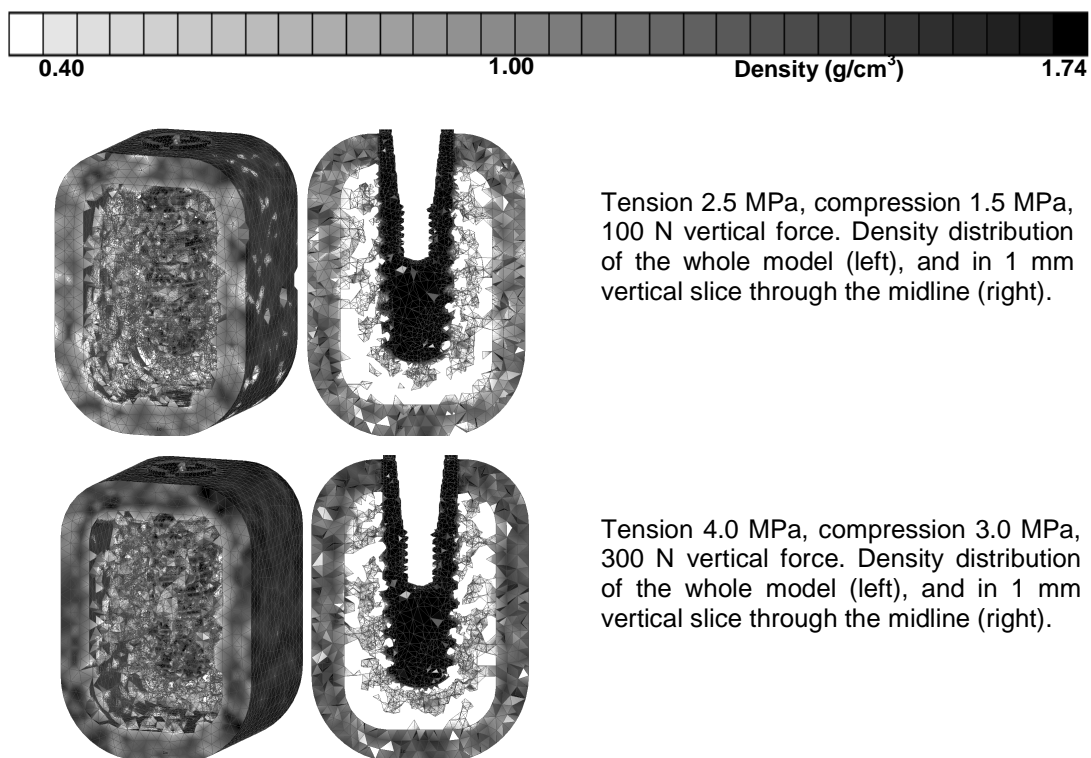
Figure 44a: Density distribution in 1 mm thick axial section after 100 time steps.

| 0.00 | | 7.00 | **Equivalent stress (MPa)** | 30.00 |

Tension 2.5 MPa, compression 1.5 MPa, 100 N vertical force

Tension 4.0 MPa, compression 3.0 MPa, 250 N vertical force
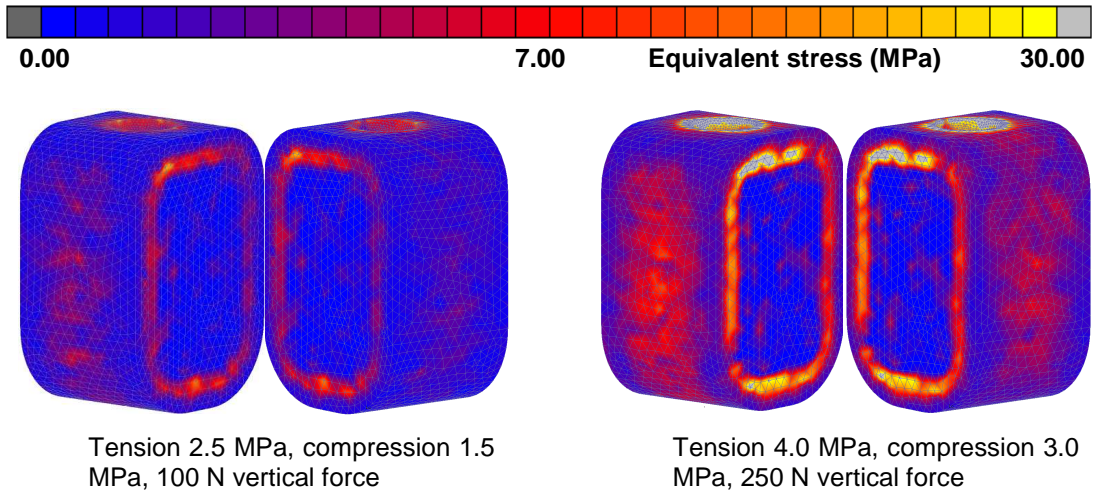
Figure 44b: (b) Distribution of the Equivalent von Mises stress after 100 time steps. Left: Tension side and right: Compression side.

4.2.1.3. Sensitivity Test: Applying Remodelling Parameters based on Mechanostat Theory

Figure 45 demonstrates density distribution after the adaptation of the remodelling parameters to match the ranges suggested by the mechanostat theory. The behaviour of the elements by means of the density change rate and the associated stress is presented as well. As the applied load on the dental implant was within the physiological range, a positive change in the density was stimulated until a stable condition was reached, where no native change in the density took place (steady state).

4.2.1.4.   Sensitivity Analysis: Occlusal Loads

Figure 46 shows the obtained density distribution with the gradual increase of the applied axial load on the Implant from 150 N up to 300 N.
More stable behaviour of the remodelling model was observed by increasing the applied axial loads on the implant. However, by applied 150 N axially on the implant, a large number of elements within the cortical bone region were

resorbed, i.e., having a density of less than 0.4 g/cm^3. Figure 47 shows the obtained density distribution with the gradual increase of the applied lateral load on the implant from 150 N up to 300 N in combination of later load of 20 N. A Similar distribution of the density was observed to that with increasing a pure axial loading on the implant. Figure 48 shows the obtained density distribution with the gradual increase of the applied lateral load on the Implant from 150 N up to 300 N.
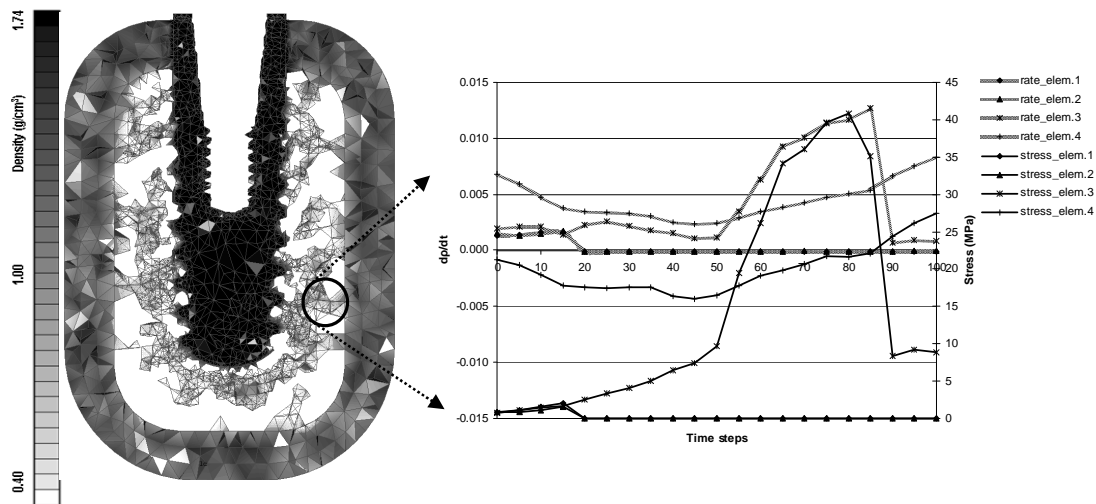
Figure 45: Obtained density distribution in a 1 mm thick vertical section though the implant/bone after 100 time steps (left). The behaviour of the elements by means of the density change rate and the associated stress is presented as well (right). The mean value of the density and stress of the elements that belong to the same node were selected to present the graphs.

On the contrary, increasing the magnitude of the applied lateral load on the implant resulted in overload resorption of the bone elements which is seen in its extreme form with 300 N.
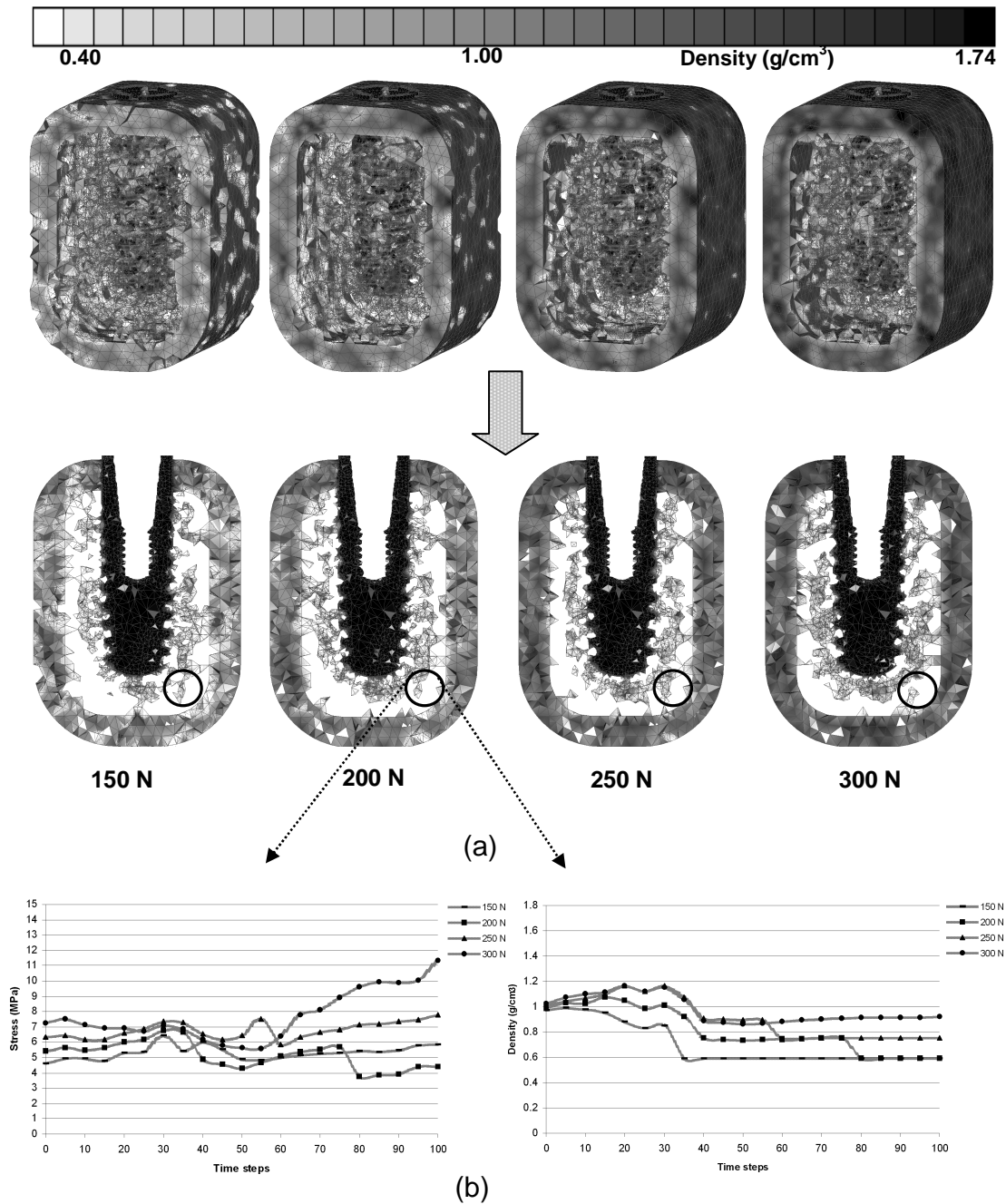
Figure 46: (a) The obtained density distribution with the gradual increase of the applied axial load on the Implant from 150 N up to 300 N, (b) the behaviour of the elements concerning the changes of the element stresses and the consequent adaptation of the density. The mean value of the von Mises stress and apparent density of some bone elements that make a bridge to the implant and that belong to the same node were selected for the graphical demonstration.
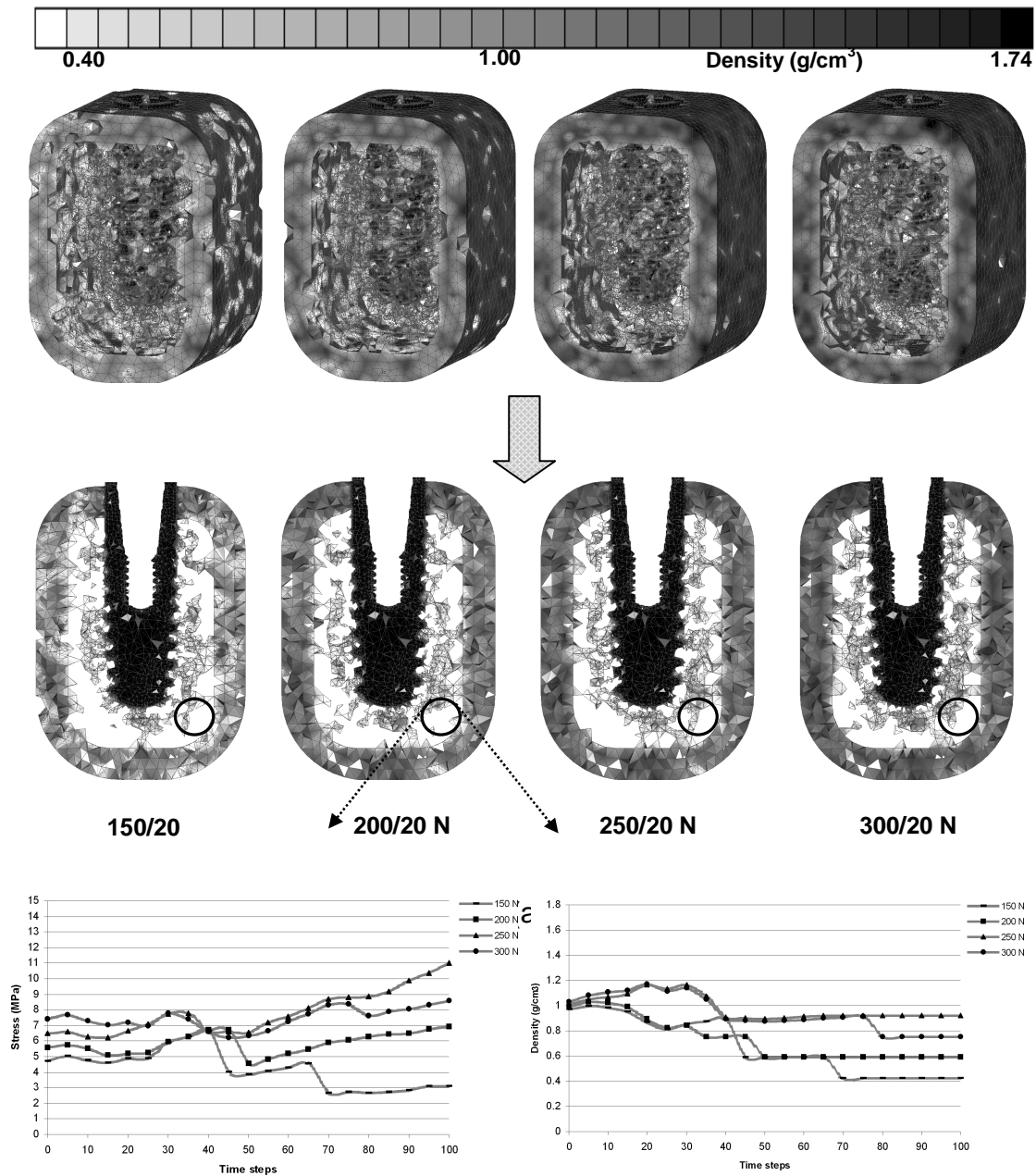
Figure 47: (a) The obtained density distribution with the gradual increase of the applied load on the Implant from 150 N up to 300 N axial combined with a lateral force of 20 N, (b) the behaviour of the elements concerning the changes of the element stress and the consequent adaptation of the density. The mean value of the von Mises stress and apparent density of some bone elements that make a bridge to the implant were selected for the graphical demonstration.
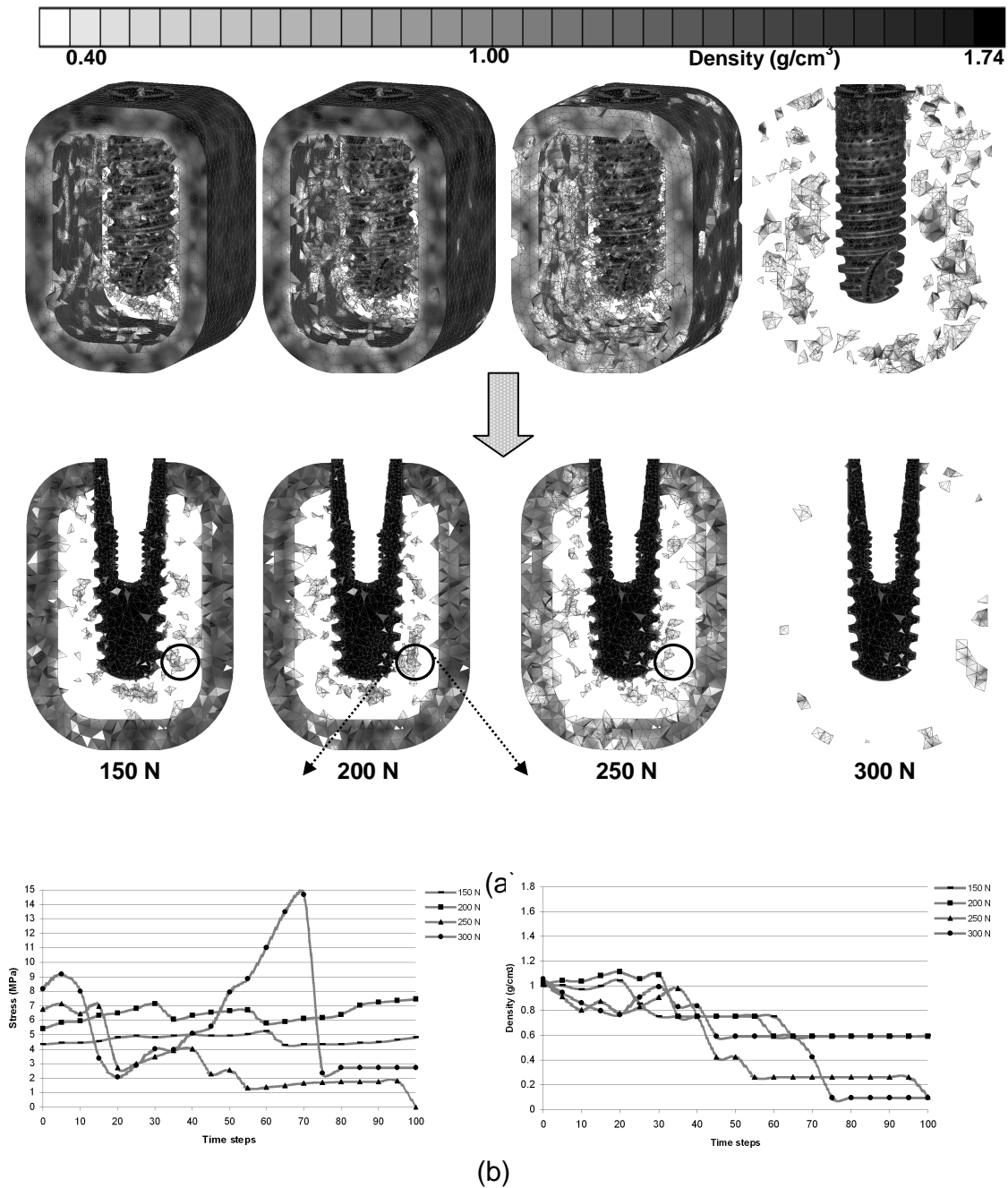
Figure 48: (a) The obtained density distribution with the gradual increase of the applied lateral load on the Implant from 150 N up to 300 N, (b) the behaviour of the elements concerning the changes of the elements stress and the consequent adaptation of the density. The mean value of the von Mises stress and apparent density of some bone elements that make a bridge to the implant and that belong to the same node were selected for the graphical demonstration.

Figure 49 shows the obtained density distribution by applying an axial load of 300 N and a lateral load of 20 N on the implant combined with tension face load of 4.0 MPa on one half of the periphery of the cortical bone and compression face load of 3.0 MPa on the other half, keeping the end faces constrained in three degrees of freedom. The obtained density distribution is compared with the real trabecular distribution in an undecalcified thin ground section of the lower jaw at the molar region (20 μm) of a baboon with a grit-blasted and acid-etched screw after 18 months of occlusal loading (Watzak et al., 2005), and a photograph of a 2 mm thick bone section from mental foramen region of edentulous mandible of a human cadaver (Kingsmill and Boyde, 1998). The obtained distribution of the elements after applying the remodelling model showed a similarity to the histological slices, in particular at the tips of the implant threads, where the highest strains are concentrated.
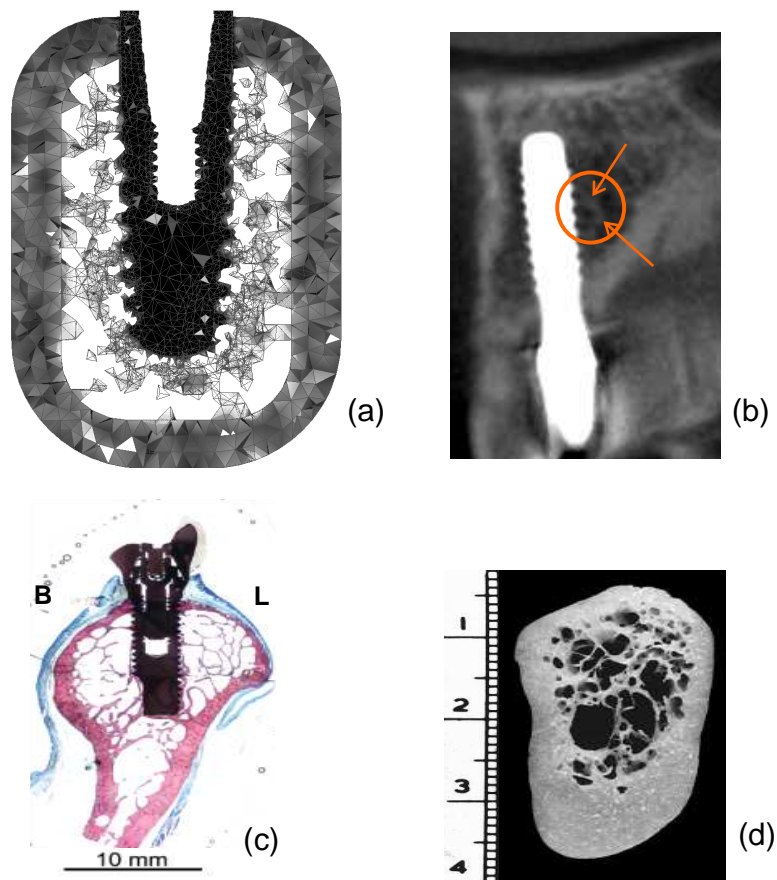
Figure 49: (a) Calculated density distribution. (b) Lateral view of a DVT-image (about 1.0 mm thickness) of a dental implant at the upper premolar region after complete osseointegration. (c) Trabecular distribution in undecalcified thin ground section of the lower jaw at the molar region (20 µm) of a baboon with a grit-blasted and acid-etched screw after 18 months of occlusal loading. (d) Photograph of a 2 mm thick bone section from mental foramen region of an edentulous mandible of a human cadaver.

4.2.1.5.   Sensitivity Test: Cancellous Bone Stiffness

Starting from very low initial stiffness of the cancellous bone (100 MPa) up to 300 MPa resulted in a wide remodelling range and reached a final maximum Young's modulus of 11 GPa. However, continuous increase of the initial stiffness of cancellous bone (400 MPa) up to 800 MPa caused shifting of the remodelling to a lower range to obtain a final maximum Young's modulus of 9 GPa (Figure 50).
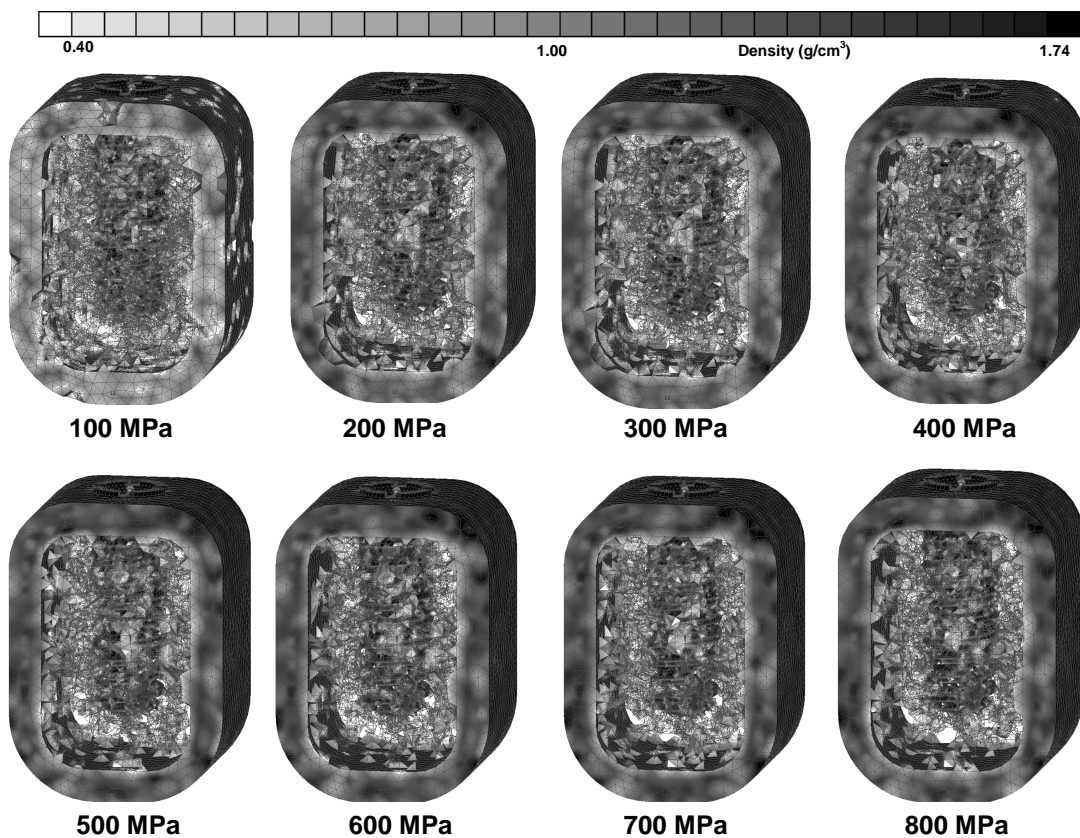
Figure 50a: Density distribution after 100 time steps with the variation of the stiffness of cancellous bone.
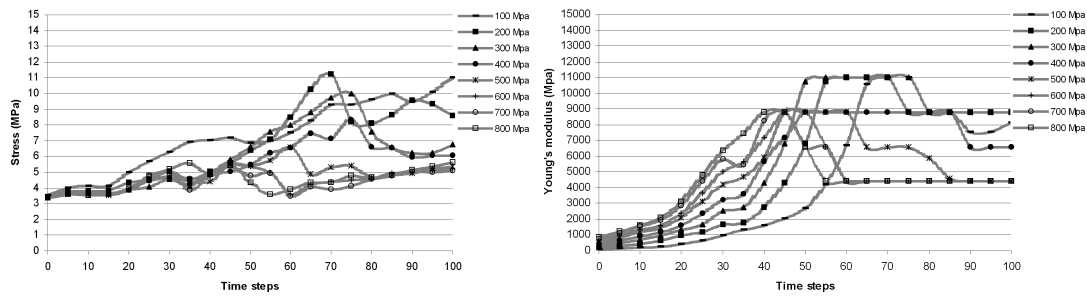
Figure 50b: (b) Obtained Young's modulus of the cancellous bone throughout the run of the simulation and the corresponding effective stresses by varying the initial stiffness of cancellous bone. A number of elements that belongs to the same node with the trabecular zone were selected to present the graphs.

4.2.1.6.   Sensitivity Test: Young's Modulus-Density Relation

By applying the bilinear constitutive relationship suggested by *Orr et al.* (1990), a stable behaviour of the bone elements, concerning density and stress distributions was observed even with implant loading of 100 N. This behaviour with the Young's modulus-density relation suggested by *Carter and Hayes* (1977) was only obtained with 300 N (Figure 51).

0.40   1.00   Density (g/cm³)   1.74

(a)   (b)
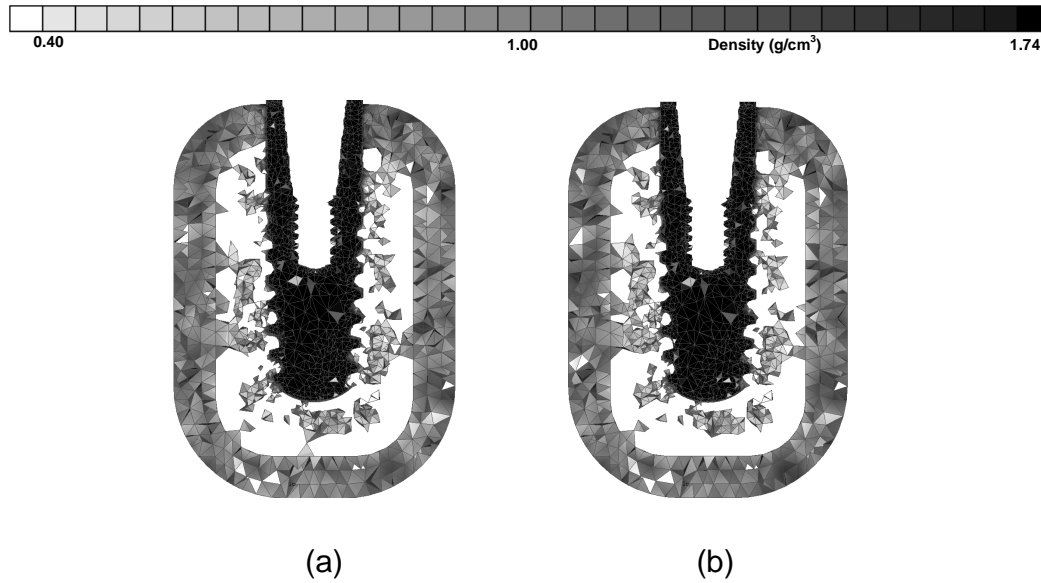
Figure 51: Density distribution after 100 time steps using the bilinear constitutive relationship suggested by *Orr et al.* (1990). (a) With 100 N implant axial load, and (b) 300 N.

4.2.1.7. Sensitivity Test: Bone Qualities

Applying the applied remodelling model to bone quality 2 showed realisable bone structure, while testing the remodelling model bone quality 3 and 4 showed minimal changes from the initial situation. However, almost all the cancellous bone elements were resorbed when the remodelling model was applied to bone quality 1 which is clinically not relevant (Figure 52).

Quality 1 Quality 2 Quality 3 Quality 4
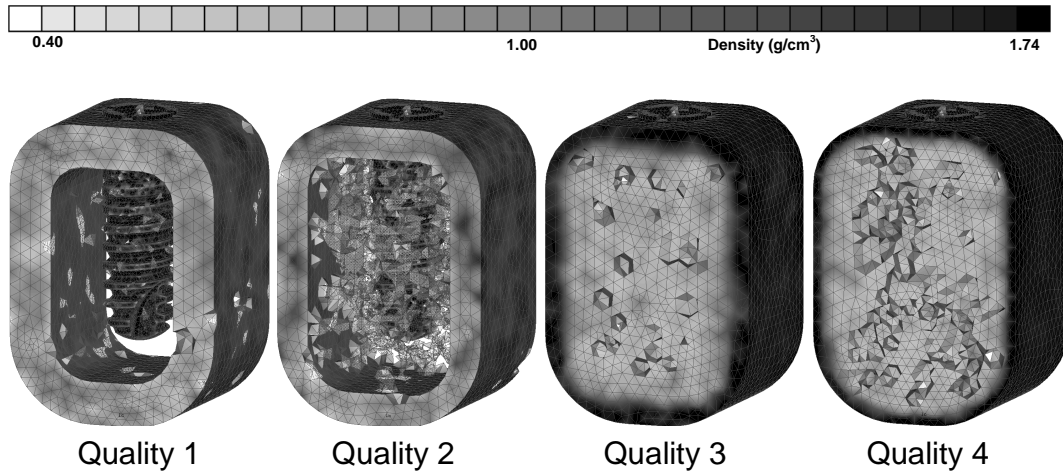
Figure 52: The behaviour of the remodelling model with the four different qualities of the jaw bone.

4.2.1.8. Sensitivity Test: Implant Geometry

The distribution of the density was different by applying the remodelling model to another implant macro-geometry (Figure 53).
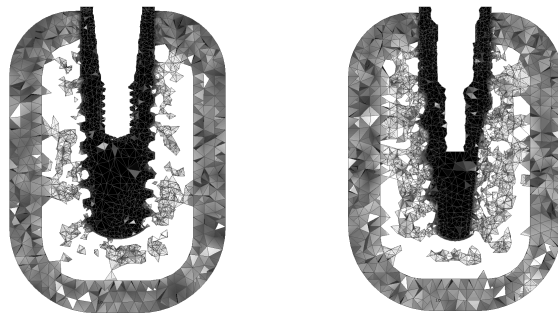
Figure 53: Density distribution after 100 time steps with different implant geometries. On the left Ankylos® A11 (Ø 3.5, L 11 mm) and on the right tioLgic© (Ø 3.3, L 11 mm).

4.2.2. Validation of the Computational Trabecular Geometry around an Implant by Using 6-year CT-Images

Density distribution of trabecular elements were analysed after 100 time steps of the remodelling simulation. Trabecular structure around the implant within about 1 mm thickness was compared to the CT-images. Despite radiation artefacts that usually combine CT-resolutions, in particular at the bone-implant interface, some regions showed a similarity between the numerical and CT-image bone structure (red arrows in Figure 54).
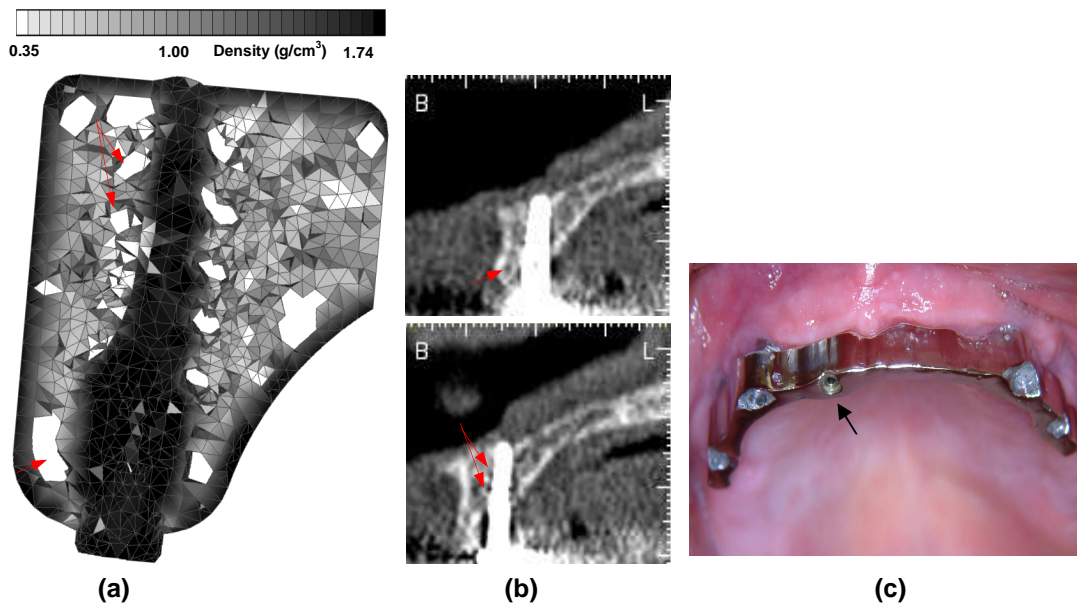
Figure 54: (a) Computational trabecular structure by applying the remodelling simulation after 100 time steps, (b) 0.7 to 1 mm thick slice along the mid of the implant from CT-images, and (c) the clinical situation of the implant at the time of CT-image documentation.

4.2.3. The influence of Soft Tissue Thickness on Bone Remodelling Simulation

Different behaviour of density distribution was obtained with the different thicknesses of the soft tissue layer using bone EEL of 0.4 mm and 0.6 mm: For bone EEL of 0.4 mm, the most stable condition was with the soft tissue layer of 60 µm thickness. By increasing the thickness to 200 µm and 400 µm, most of the bone elements, in particular in the cortical bone region, had density dropping below 0.3 g/cm^3 within the first ten time steps of running the simulation (Figure 55). The use of 0.6 mm as bone EEL did not, however, show much better results concerning the stability of the remodelling model. The sudden drop of the element density below 0.3 g/cm^3 started even earlier, i.e. with 80 µm thick layer of the soft tissue. By increasing the thickness to 200 µm and 600 µm, no bone elements but the soft tissue ones were remained after 100 time steps of running the simulation (Figure 56).

4.2.4. Remodelling Model Including Soft Tissue Interface

Running the remodelling simulation for the FE model of the two weeks healing phase (only connective tissue) showed a positive remodelling and increase of the element density, in particular at the thread region of the implant-CT interface. The FE model of the two months healing phase showed continuous increase of the density associated with negative remodelling at certain regions, namely, in the spaces between the lower threads. However, a creation of a cortical layer at the initial SC-region was observed with the FE model of the four months healing phase (Figure 57 a-c). The obtained results are comparable with the documented radiographical findings which show the building of a thin layer of highly dense bone around the implant after six months from the operation (Figure 58). The results of the three healing phases models showed a correction by concerning the density change of the callus tissues and implant displacement, i.e., the improvement of the positive remodelling and the reduction of the implant displacement (Figure 59).
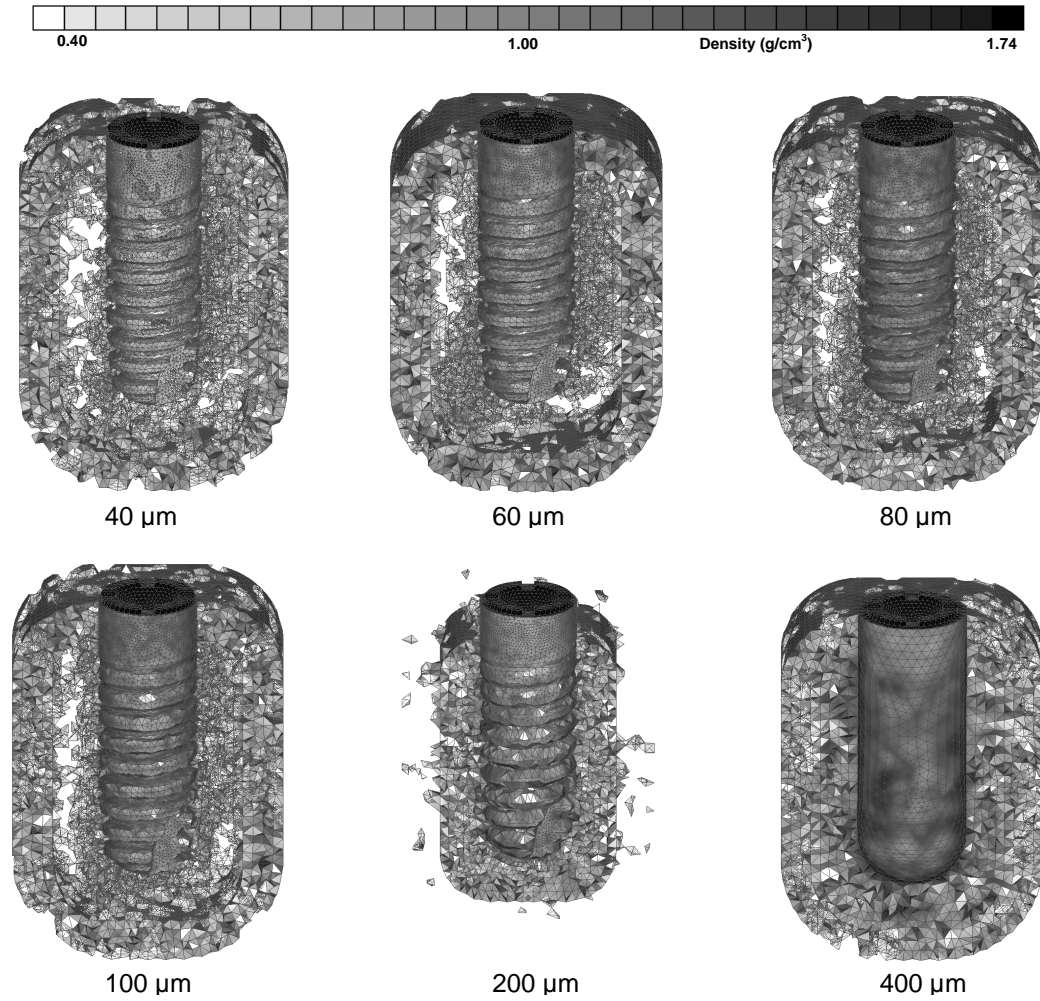
Figure 55: A view along the mid of the FE model describing density distribution with different thickness of soft tissue around the dental implant using EEL of 0.4 mm. The light layer around the dark coloured implant is the soft tissue layer.
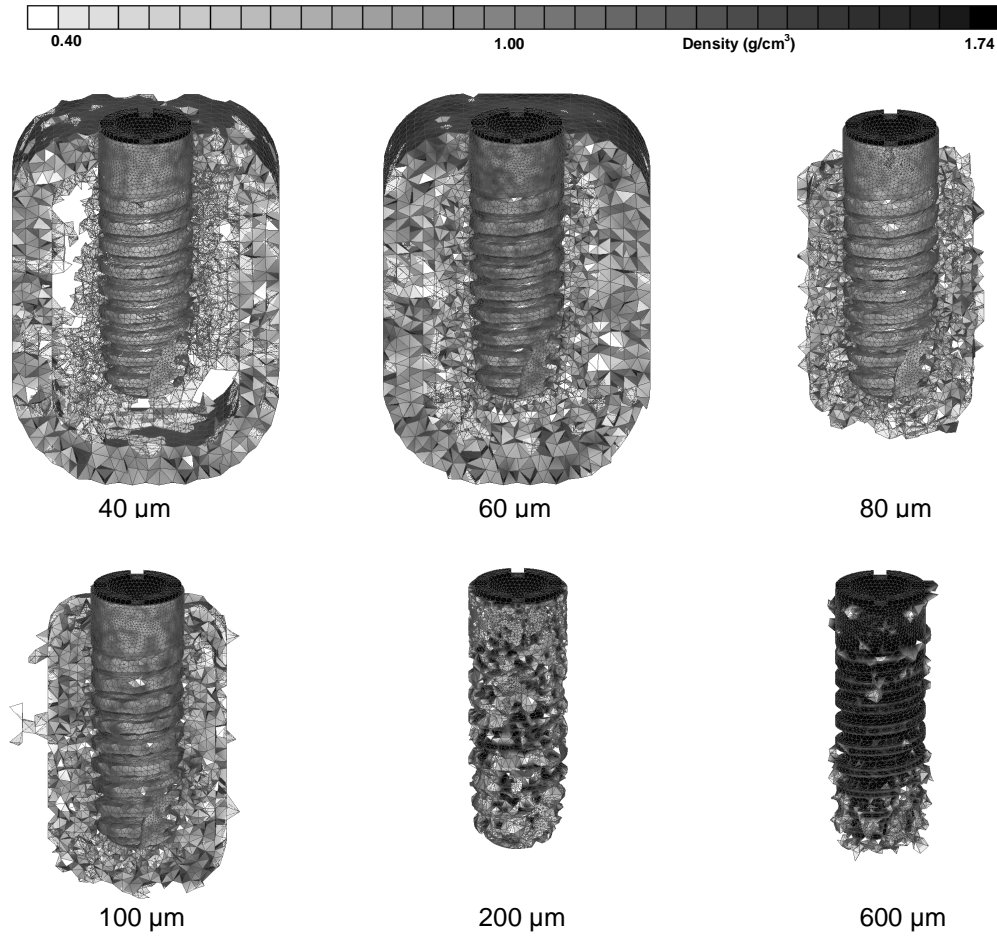
Figure 56: A view along the mid of the FE model describing density distribution with different thickness of soft tissue around the dental implant using EEL of 0.6 mm. The light layer around the dark coloured implant is the soft tissue layer.
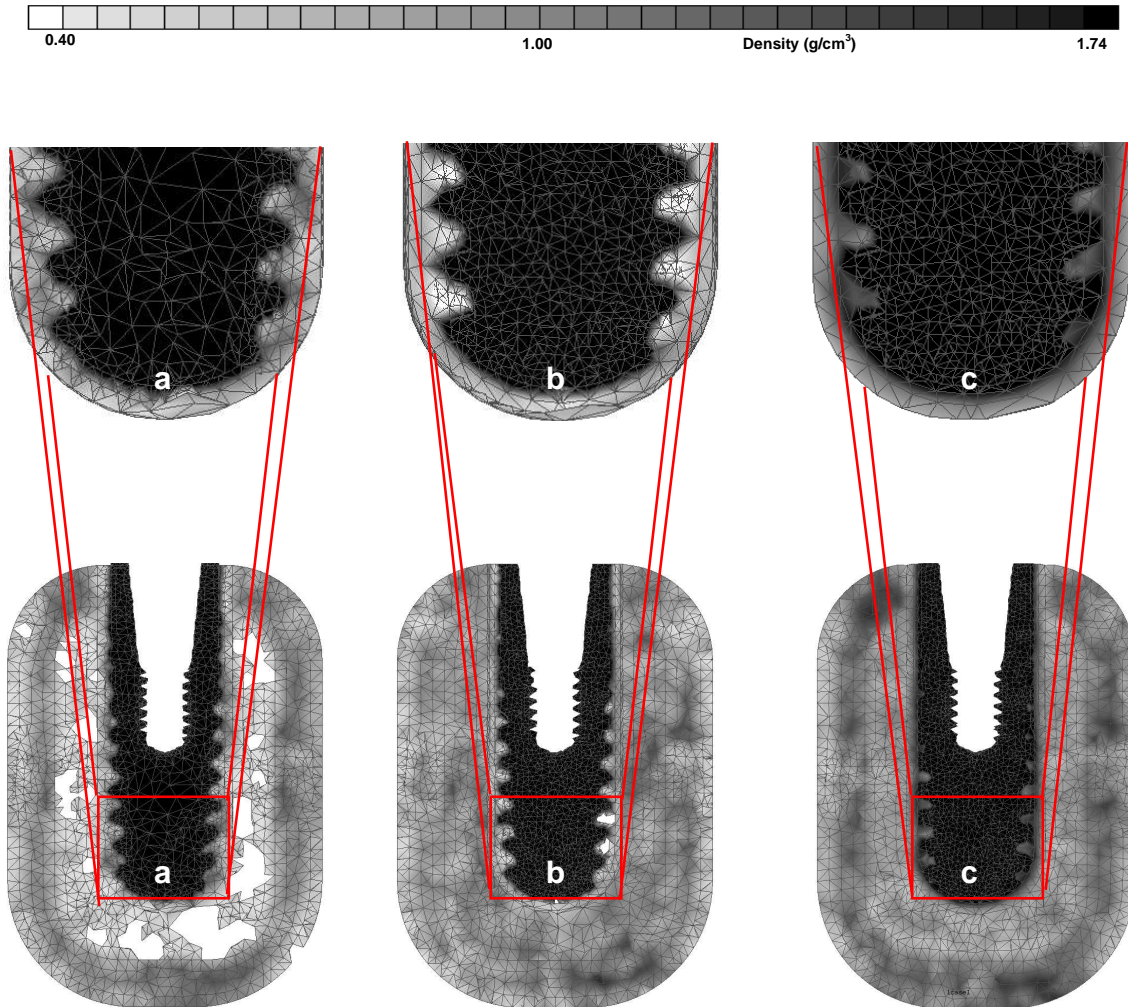
Figure 57: Density distributions of the different callus tissues that represent the progress of healing for the three FE models. (a) Model after two weeks, (b) model after two months, and (c) model after four months.

Upper row: Detailed view of the density distributions within the callus layer(s).

Lower row: General view of the density distributions of the whole model presented in a longitudinal cross section throughout the mid of the FE model.
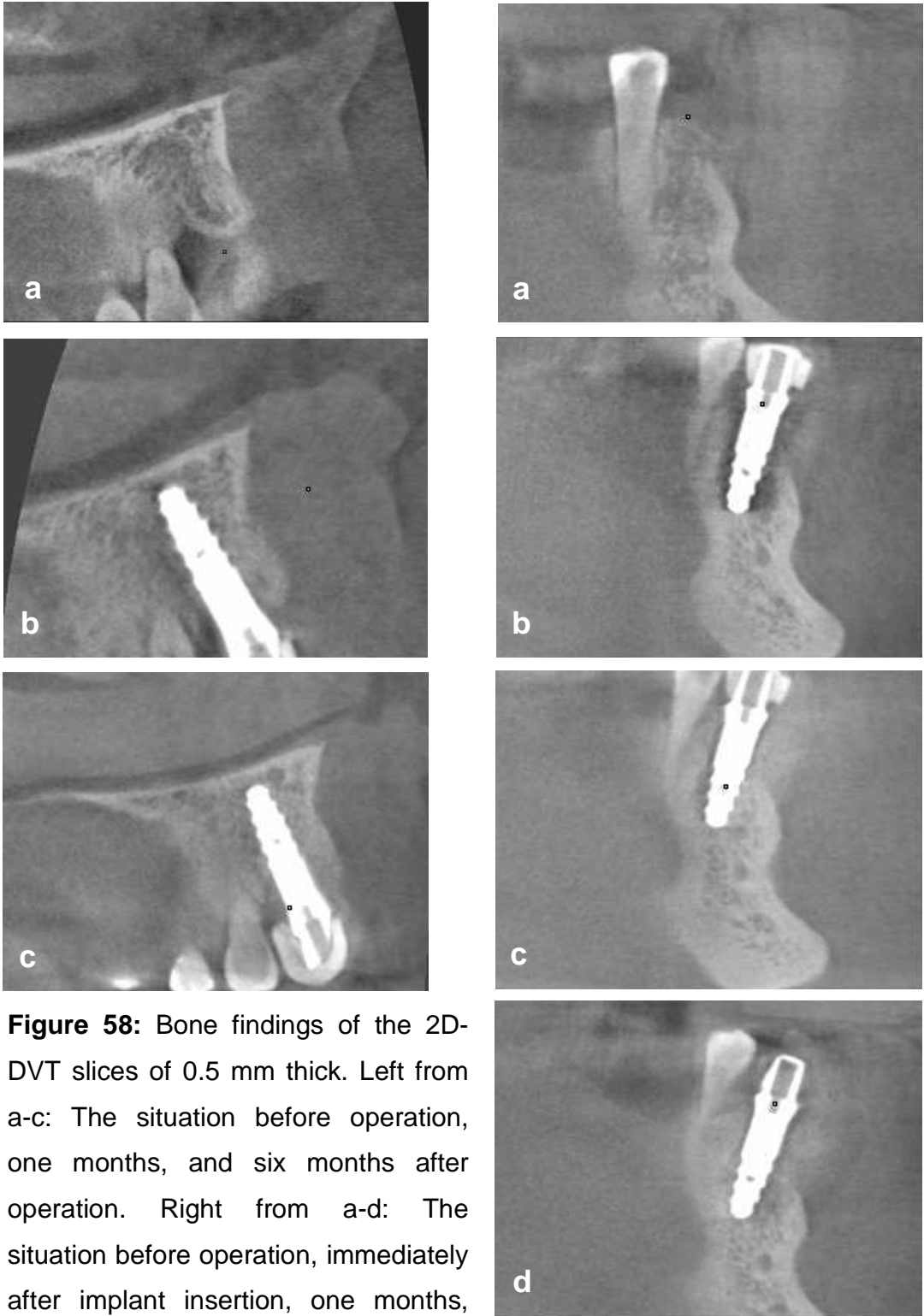
Figure 58: Bone findings of the 2D-DVT slices of 0.5 mm thick. Left from a-c: The situation before operation, one months, and six months after operation. Right from a-d: The situation before operation, immediately after implant insertion, one months, and six months after operation.
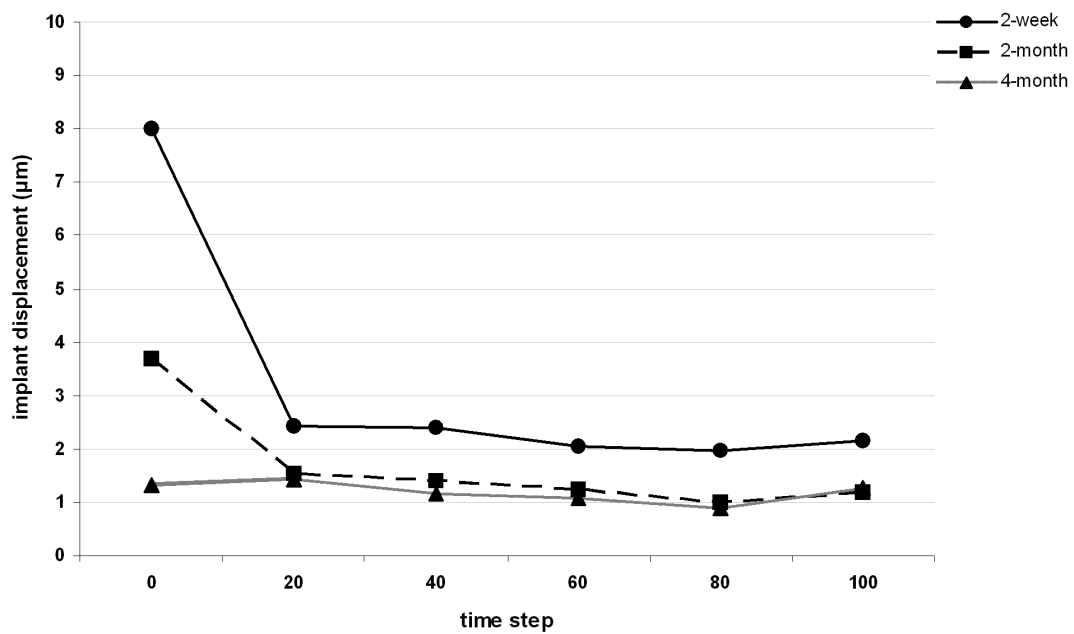
Figure 59: Implant displacements from time step zero to 100 of the three healing phases.

Chapter 5

5. Discussion

5.1. Mechanical Investigation of Different Implant and Abutment Designs: Experimental, Numerical and Clinical Aspects

5.1.1. Numerical Investigation of Fixed Partial Prosthesis FPP

Designing models that simulate clinical situations is essential. In this part of the study, the bone in the anterior maxilla was carefully designed in order to approximate the clinical situation of Kennedy Class IV edentulous ridge treated with four-unit fixed partial prosthesis. The prosthesis was supported by two immediately loaded endosseous implants. Clinically, restoration of all four upper incisors with a prosthesis supported by only two endosseous implants represents an extreme solution, when immediate loading is assumed. The study was based on this extreme condition to investigate numerically the distribution of stresses and strains around the supporting implants in relation to the abutment design.

To approximate the clinical situation, a distance that represents the thickness of the residual mucosa was maintained between the lower border of the prosthesis and the alveolar bone. Applying the load near the cingulum area in a palato-labial direction simulates a clinical situation.The mandibular incisors close on the palatal surfaces of the maxillary incisors, with the mandible near centric occlusion. Applying the load in such a way helps to assess the behaviour of the implant and the response of the bone in such a clinical condition. It may be argued that a force of 150 N is quite low; however, *Mericske-Stern et al.* (1995) found that the average value of the maximal occlusal force was distinctly lower with implant-supported prosthesis than with the natural dentition. Accordingly, in the present study a total force of 150 N was distributed equally on the four units of the prosthesis at 45° to the long axis of the ab utment in the palato-labial direction defined locally for each unit of the prosthesis. Moreover, typical occlusal forces are in the range of 100 N under normal biting, higher forces only occur in patients suffering from bruxism or parafunction and during grinding. Usually this is defined as a contra-indication for treatment with implant-supported FPP.

Several studies showed that a micro-motion of less than 30 µm at the bone-implant interface does not interfere with the osteogenesis (Kawahara et al., 2003), while an even wider range (50-100 µm) has also been reported as not being determinal (Horinchi et al., 2000; Meyer et al., 2003). In the present study, the resultant implant displacements were within the safe range without interfering with the primary stability of the supporting implants. However, implant displacement was 15% less with the straight abutments than with those associated with the angled abutments.

Saab et al. (2007) studied the strain in the bone around dental implants in the anterior maxilla in a FE investigation. They obtained a value of 4,650 µε as a maximum principle strain with the straight abutment and 4,020 µε with the angled abutment with a generally similar pattern of strain distribution for both models. The presented immediately loaded models yielded a 12% higher strain in the bone for the angled abutment compared with the straight abutment. Wider stress and strain distributions in the bone were associated with the angled abutments. On the other hand, osseointegrated models showed a value of 1,026 µε as a total equivalent strain with the straight abutment and 1,313 µε with the angled abutment and a similar distribution pattern. The strain values of the osseointegrated models in the present study were about 70% lower than those obtained by *Saab et al.* (2007) in their study of a single osseointegrated implant with an applied force of 178 N. As can be seen in Figures 21a and 21b there is a difference in the stain distributions at the left and right lateral incisal areas, i.e. at the coarse thread region which could be related to the position of the splits along the coarse threads in relation to the direction of the applied forces. Such behaviour could be one of the possible reasons of the different survival rates of the immediately loaded implants that support the same prosthesis.

The mechanostat theory proposed by *Frost* (2003) indicates that mechanically induced bone remodelling remains inactive during loads that cause bone strains of 200 to 400 µε. However, it is enabled when strains are higher than 400 µε up to 4,000 µε, where the bone density is increased. Accumulation of bone micro-damage starts with strains higher than 4,000 µε up to 25,000 µε. The increase in

bone mass caused by strains within the physiological range would tend to reduce the deformation back to the threshold strain. The obtained strains from immediately loaded cases were within the pathological strain range according to the mechanostat theory, whereas those obtained from osseointegrated cases were within the physiological range. Basically, these arguments hold true for the mandible as well. However, the bony structure in the mandible differs from that in the maxilla, as does the loading condition. Consequently, analyses of an implant-supported FPP in the mandible would have to take into account the different bone qualities and loading conditions, resulting in slightly different stress and strain distributions, explaining perhaps the reduced clinical failure rate in the mandible. Consequently, the presented results can confirm the success of the standard protocol of unloaded healing and progressive bone loading, which are commonly recommended for the implant treatment in general and in the anterior maxilla in particular. Immediate loading of two implants in such a clinical situation is not recommended, unless more implants are to be considered, i.e. four implants in the presented case instead of two, employing splinted crowns of the final prosthesis to reduce the risk of overloading and ensure a homogenous distribution of the load throughout the implants.

One of the limitations was the use of an idealised geometry of the final prosthesis and the corresponding adaptation of the position of the implants within the bone, which is the opposite case clinically. In order to produce more accurate geometrical foundation, it might be possible to improve the present FE model by using computer tomography of animal maxillary specimens with implant-supported prosthesis.

5.1.2. Experimental and the Associated Numerical Investigations of Different Implant and Abutment Designs

This part of the study differentiated between passive-threads, roughened neck implants versus modified passive-threads, fine-threaded neck implants, in addition to the differentiation between straight abutments versus 20°-angled designs. The direction, magnitude and repetition rate of biomechanical loading can influence the modelling and remodelling process in bone surrounding endosseous implants. Strain incurred on immediately loaded implants can stimulate bone healing similar to that of fracture healing, where cyclic micromovement causing strain or deformation of the bone cells largely determines the cellular behaviour of bone cells.

Implant stability might be different since implant primary stability is the result of the interaction among implant design, the biomechanical properties of the local bone and the implant bed preparation technique (Meredith, 1998). According to *Meredith* (1998), macrogeometery and implant design should alter implant primary stability. *O'Sullivan et al.* (2000) compared the primary stability of implants of various designs like MKII, the MKIV, the Osseotite and the TiOblast implants placed in the maxilla of human cadavers. They did not find a statistically significant difference between implants despite differences in peak torque insertion. Similarly, *Rasmusson et al.* (2001) failed to measure any difference in primary stability between Brånemark and Astra implants placed in a dog mandible. Surprisingly, it appears that a large variety of implants achieve similar primary stability. Primary stability seems less affected by implant design than by local bone quality. In this study the displacements of both implant designs were nearly similar (mean displacement of 151 μm for Tiolox[®] and 145 μm for tioLogic[©]) although the total applied load was lower than the average biting force at the upper anterior region. There are numerous studies evaluating the primary stability of implants; however, there are relatively few which evaluate the influence of abutment design on the primary stability.

In this part of the study, tioLogic$^©$ implants had noticeably smaller mean displacement and rotation (103 μm, 2.7°) with the a ngled abutments than with the straight ones (145 μm, 3.7°). On the contrary, Tiol ox$^®$ implants showed higher mean displacement and rotation (174 μm, 4.8°) with the angled abutments than with the straight ones (151 μm, 4.4°). The values w ere given with a total applied force of 40 N. Figures 60a and 60b give an overview of the mean total displacement and rotation of the implants with the two abutment designs with the total force of 75 N.
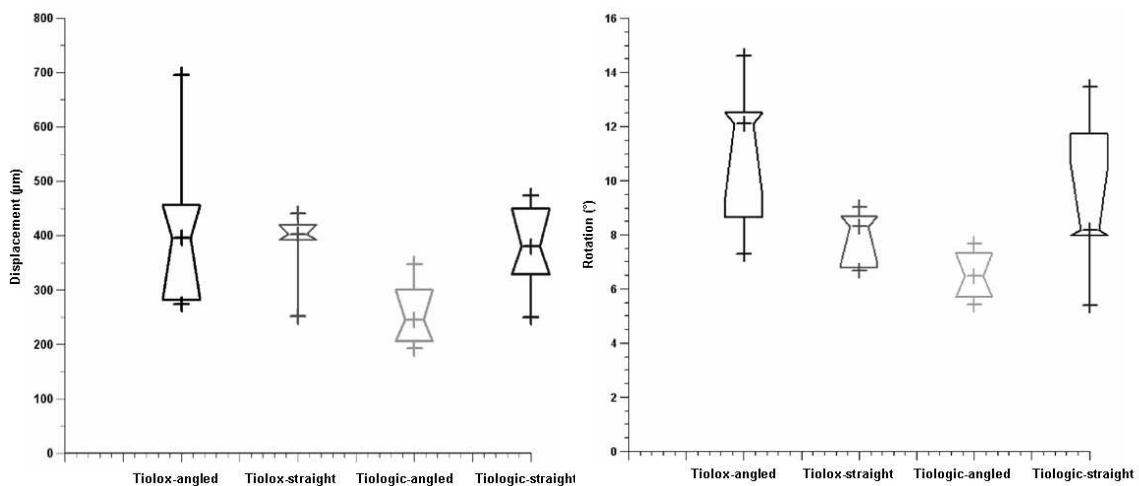
Figure 60: Mean displacements and rotations of the two implant systems with the straight and 20°-angled abutment designs with t he total force of 75 N.

It seems that the influence of the abutment design on the magnitude of the total displacement is associated with the design of the endosseous implant. The connection of an angled abutment with an implant with rough, fine-threaded cervical region, in our case tioLogic$^©$ implants, showed less micromotion than the straight abutment. This can give an impression that such implant design can better tolerate angular load. On the other hand, the connection of an angled abutment with an implant with passive threads and roughened cervical region, in

our case Tiolox® implants, showed an inverse effect and resulted in higher micromotion of the implant.

The obtained displacements from the presented experimental study showed high values (>100 µm) with a small force magnitude (40 N) according to the suggested allowed micromorion for dental implants. However, most of the similar implant systems have a long-term survival cinically (Mundt et al., 2006), a matter that arises the questions: (1) Is the suggested range of the allowed micromotion of dental implants reasonable? (2) Does the method that is usually used for testing the primary stability give the actual magnitude of the implant motion? Further studies concerning the type of the bone tissue used as an implant bed and the method of measuring the implant micromotion is needed to clarify the influence of the above mentioned factors on the precision of the allowed range of implant micromotion. The numerical results showed mean displacements close to those obtained in the experiment, while the rotation showed a considerable drop numerically (Figure 61).
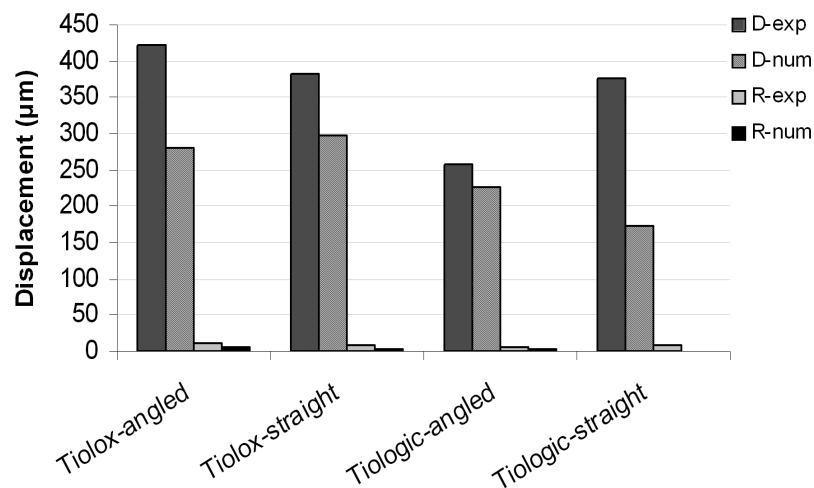
Figure 61: Experimental and numerical mean displacements and rotations of the both implant systems Tiolox® and tioLogic© with the corresponding straight and angled abutments. The displacements and rotations are achieved with a total force of 75 N.

It seems that the success of immediate loading procedures is a matter of appropriate patient selection, loading conditions, implant (geometry and surface treatment) and prosthesis design (Gapski et al., 2003). However, due to the lack of understanding of the relationship between interface biomechanics and bone biology, it is difficult to predicatively comment on any of the previous factors. Optimising implant geometry in order to maintain a beneficial stress level at the bone-implant interface is a complex issue (Geng et al., 2004). There are many studies analysing the stress distribution generated in the surrounding bone in order to arrive at the optimum shape and thread design (Chun et al., 2002; Pierrisnard et al., 2002).

A couple of basic prerequisites are to be fulfilled by a proper implant design, that are: (1) Assure sufficient initial stability, reducing implant micromotion below the 'tolerated threshold' (approximately 100 µm) and thus minimising the waiting-period required for loading the implant. (2) Incorporate design factors, that would diminish the effect of shear forces on the interface (such as surface roughness related and thread features) so that marginal bone is preserved. (3) Respect design features that may stimulate bone formation and/or facilitate bone healing (secondary osseointegration).

A certain thread size and thread profile cannot only be chosen on the basis of how it performs in an idealised model but should also be validated when applied on the intended implant design and with the bone anatomy in which it is to perform. *Hansson and Werke* (2003) studied the pure effect upon bone stresses of variations of the thread profile of implants embedded in cortical bone. They concluded that for an axially loaded, infinitely long and infinitely stiff, screw-shaped implants embedded in homogenous isotropic cortical bone and with a frictionless and continuous bone-implant interface (1) the profile of the threads affects the magnitude of the stress peaks in the bone and the capacity of the implant to resist loads, (2) providing that the profile is favourable, threads of small dimensions are quite effective, and (3) a straight part at the bottom of the thread is for most thread profiles unfavourable.

If the profile is favourable, a thread of depth D of only 0.1 mm appears to be effective as a thread of 0.4 mm depth. Thus threads of very small dimensions can theoretically be quite effective. This conclusion finds support in the remarkably good preservation of the marginal bone observed for a dental implant provided with a microthread at the neck (Nordin et al., 1998; Norton, 1998; Palmer et al., 1997; Puchades-Roman et al., 2000). In this part of the study, both implant systems had a coarse-thread depth of 0.43 mm and fine-thread depth (tioLogic© implants) of 0.1 mm.

In order to avoid stress induced bone resorption, it was suggested to use an implant design for which the peak bone stresses resulting from an axial load are spatially separated from those resulting from a transversal load. For a dental implant *Hansson* (2000, 2003) found that with a conical implant-abutment interface located at the level of the marginal bone combined with retention elements at the endosseous implant neck portion, the peak bone stresses provided by an axial load are located further down in the bone implying that this is a design fulfilling the requirement set up by *Mailath et al.* (1989) and *Stoiber* (1988). It is evident that the design of the implant thread does affect the stress pattern in the bone. An underlying assumption was that the smaller the peak stress in the bone, caused by a standardised load, the higher is the load the implant can carry before bone resorption is triggered.

FEM allows the estimation of stresses and strains of extremely geometrically complex systems, such as dental implant-bone systems. The validity of mathematical models is difficult to estimate objectively. It might be assessed by experimental verification, that is, by relating the calculated results with other comparable FE analyses. The possibility of investigating several loading conditions on different types of implants and different morphometry and bone properties is a remarkable advantage of numerical analyses. In spite of the fact that solutions arising from numerical methods must always be carefully evaluated in the light of experimental testing, it seems reasonable to exploit this approach for the possibility of evaluating data that are experimentally not measureable,

such as strain or stress in the bone tissue, thus completing and extending information obtained from in vivo or in vitro tests.

Concerning the stress, in this study Tiolox[®] implants (without fine threads in the cervical region) showed higher mean stresses than tioLogic[©] implants (with fine threads in the cervical region). In both implant systems, the stresses were within the acceptable range (below 100 MPa, Frost, 2003, Figure 30a). The strains were higher with the Tiolox[®] implants connected to angled abutments to those connected to straight abutments, while tioLogic[©] implants showed no difference in the magnitude of the strain between the straight and angled abutments (Figure 30b). Still the obtained strains with both implant systems are much higher than those suggested for the physiological strain limits of the bone (above 4,000 µε, Frost, 2003). The numerically obtained high values of the strain coincide with the high displacement of implants that were observed experimentally.

Based on the above mentioned numerically obtained results and their linearity, the strains and stresses are above the physiological range when normal implant loading at the anterior region is considered.

5.1.3. The Relation of Crestal Bone Resorption to the Abutment Design used in Implant-Supported Fixed Partial Prosthesis

Numerous recently published studies have focused on treatment outcomes of implant therapy in partially edentulous patients in general and related to maxillary anterior teeth replacement in particular (Belser et al., 2003; Naert et al., 2002; Wyatt and Zarb, 1998). Implants placed in the anterior region of the maxilla failed significantly more often than those placed in the posterior region. Length and diameter of the implants did not have significant influence on the cumulative survival rate (Andersen et al., 2001). Factors favourably affecting the success of screw-type implants placed to support full- or partial-arch prosthesis include: Location (jaw and area of implantation), length, restorative\abutment design, and implantation protocol (nonsubmerged or submerged).

The use of angulated abutments is well established. The concern about survival of implants had largely been dispelled (Kallus et al., 1990). Angulated implant placement to optimise the available bone is seen as an advantage (Krekmanov et al., 2000).

In this part of the study, we investigated the relation of the abutment design on the amount of cervical bone resorption clinically as a complementary step for the numerical and experimental investigations that were discussed previously in this chapter. *Celland et al.* (1993) studied the effect of abutment angulation in a photoelastic resin and using a strain gauge in one model. They tested 0º, 15º and 20º abutments and demonstrated that a statistically significant difference existed for each increase in abutment angulation. According to the authors, all abutments produced strains that appear to be within the physiologic range for bone.

The study of *Gelb and Lazzara* (1993) and *Celletti et al.* (1995) showed no adverse osseous changes over a period of three years when preangled abutments were used after six months healing period. However, these authors reported three clinical cases, and the correlation is being made with results from an animal study that took 1.5 years, during which the implants were loaded only for one year.

In this part of the study, probing depth around implants up to one year was measured. 24 patients were included. The implants for 13 patients were connected to straight abutments and for 11 patients were connected to 20º angled abutments. In the FE investigation of implant-supported FPP (section 4.1.1.), the magnitude and the distribution of the stresses around implants cervically with 0º and 20º angled abutments were studied.

Concerning the stress results obtained from FE models of FPPs (Table 8), the clinical follow-up showed no statistical significant difference of the probing depth (P=0.4), although the numerical analysis showed higher stresses for nonsubmerged (immediately loaded) implants with straight abutments than submerged (osseointegrated) implants. Nevertheless, the stress results agree with the clinical finding for angled abutments when they were used for

submerged or nonsubmerged protocol, i.e. angled abutments showed less probing depth when a submerged implantation protocol was selected instead of a nonsubmerged protocol (P=0.01).

Furthermore, no statistical significant difference was obtained for straight and angled abutments with the nonsubmerged protocol (P=0.2). This is an agreement with the numerical results of the FPPs (Table 8) and those of the experimentally investigated bovine samples (Figure 61).

However, smaller values of probing depth were obtained and were statistically significant for angled abutments with submerged protocol than straight abutments although the numerical analysis showed a minimal difference of the two abutments. However, smaller values of probing depth were obtained and were statistically significant for angled abutments with submerged protocol than straight abutments although the numerical analysis showed a minimal difference of the two abutments.

Although the size of the study groups was small and the follow-up period was short, the present results could be the primary stone for further investigations and for longer periods. Finally and according to the results from the experimental, numerical and clinical studies, we can conclude that numerical analysis by means of FEM is a useful tool that could help to understand the biomechanical reaction of bone to changes of the mechanical environment. The results of this and previous studies underline that a combination of experimental and/or clinical results is essential.

5.2.   Bone Remodelling Simulation

5.2.1. Sensitivity Analysis

After apprehensive study of the available literature concerning bone remodelling, the model suggested by *Weinans et al.* (1992) and expanded by *Li et al.* (2007) was finally selected. It is an internal bone remodelling scheme that uses an internal remodelling approach based on the changes in the apparent bone

density as a function of the mechanical stimulus. The model demonstrates bone resorption by means of density change rate in the negative direction, in both disuse and overloading conditions. The sensitivity of the applied model was tested in response to different mechanical environments, started by developing idealised bone models surrounding a screw-shape implant with different EELs, from a small one represented by 0.2 mm and lasting with a large length which was selected to be 0.8 mm. Different behaviour concerning density change and distribution were obtained (Figure 32). This could probably be caused by the use of linear elements (tetrahydral 4) that results in a sudden jump in the element stresses and strains which correspondingly results in different behaviour of the change in the bone densities. EELs 0.4 mm and 0.6 mm were finally selected to test the other mechanical condition. The selection was based on two main reasons; firstly, the comparable density distribution with the histomorphometric studies (Ulm et al., 1999; Watzak et al., 2005), in particular the stability of the density within the cortical bone region; secondly, the acceptable total time required to calculate the density change for the whole bone elements of the model.

The clear influence of element size was confirmed again by applying a thin layer of soft tissue to the FE model. The disturbance of the homogenous size of bone elements by introducing fine elements, which could not be avoided for thickness and morphological requirements, resulted in an unstable model and a sudden drop of the density of most of bone elements below 0.3 g/cm^3 (Figures 55 and 56).

The internal stress distribution in the jaws is affected not only by forces on the teeth/implants, but also by forces applied on the jaw by the muscles of the masticatory system and facial expression, due to various moving actions required by chewing, swallowing, speech and involuntary jaw motions. *Hobkirk and Schwab* (1991) have demonstrated, in subjects with edentulous mandibles containing osseointegrated implants, that jaw movement from the rest position results in relative displacement between the linked implants of up to 420 µm and force transmission of up to 16 N. Determination of muscle forces presents a

complicated problem, which requires information on the muscle activity levels, which are further complicated if mastication is taking place (Koolstra et al., 1999; Müftü and Müftü, 2006). The internal stress in the mandible, therefore, can have a very complicated distribution (Hart et al., 1992; Hirayabashi et al., 2002). In the presented study, different boundary conditions were tested to study the response of the applied remodelling model to the different loading condition of the jaw bone represented by the attached muscles in function (pulling and/or pushing action on the jaw) with varying loading magnitudes (Figure 43) by concerning the mass weight of the muscle and the length of the attachment side to the bone.

Koseki et al. (2005) estimated the forces and stresses within the mandible caused by the masticatory system in a FE model of the human mandible. The stress was within 13 to 15 MPa at the posterior buccal region of the body of the mandible and 6 to 8 MPa at the posterior lingual region. In the present study, tension face load of 4.0 MPa was applied on the periphery of the cortical bone on one half (represents the buccal side) and compression face load of 3.0 MPa on the other half (represents the lingual side). After 100 time steps, a homogenous stress distribution of 14 to 15 MPa on the tension side and 5 to 7 MPa on the compression side was obtained (Figure 44b). The distribution of the density was located more on the compression (lingual) side than on the tension (buccal) side. A similar behaviour was observed by *Ulm et al.* (1999) in their study of the characteristic features of cancellous bone in edentulous maxillae. They were observed a denser configuration of trabeculae palatally than those in the buccal and crestal portions.

Frost proposed that bone responds to a complex interaction of strain magnitude and time. Conceptually, the interfacial bone maturation, crestal bone loss and loading can be explained by the Frost mechanostat theory (Frost, 1987) which connects the two processes of modelling (new bone formation) and remodelling (continuous turnover of the older bone without a net change in shape or size). In accordance with the theory, bone acts like a "mechanostat", in that it brings about a biomechanical adaptation, corresponding to the external loading condition.

Frost (2000) described four micro-strain zones and related each zone to a mechanical adaptation (Figures 2 and 14). The four zones include the disuse atrophy, steady state, physiologic overload and pathologic overload zones. Both extreme zones (pathologic overload zone and disuse atrophy zone) are proposed to result in a decrease in bone volume. When peak strain magnitude falls below 50 to 200 µε, disuse atrophy is proposed to occur, a phenomenon that is likely to explain ridge resorption after tooth loss. In the pathologic overload zone, peak strain magnitude over 4,000 µε may result in net bone resorption. The steady state zone comprises the range between disuse atrophy and pathologic overload zone, and is associated with organised, highly mineralised lamellar bone. In this study, remodelling parameters were adapted to match the zones described by the mechanostat theory, i.e. the lower critical stress to be 2.0 MPa (105 µε) below it disuse bone resorption takes place, where as the steady state is to be within the range of 2.0 to 8.0 MPa (105-415 µε), where no change in bone density occurs. The upper critical stress was considered to be 60 MPa (4,000 µε), above it overload bone resorption occurs.

Various factors can influence the maximal bite force such as different age groups, between denture wearers and persons with natural teeth, between different parts of the dental arch, between persons with and without clinical symptoms of dysfunction. In a multivariate approach, 58% of the variance of bite force magnitude in adults was explained by craniofacial morphology and master muscle thickness (Raadsheer et al., 1999). Bite force magnitude had a positive association with thickness of the masseter muscle. *Radsheer et al.* (1999) also found that the contribution of the masseter muscle to the variation in bite force magnitude and moment was higher than that of the craniofacial factors. Regarding the muscle per se, there is a large inter-subject variability of size and shape of muscular attachments, jaw muscle insertions alter position during functional movements, and their displacement patterns vary according to the muscle (Goto et al., 1995). Also, *Goto et al.* (2001) showed that the deep and superficial regions of the masseter muscle do not stretch uniformly during major

jaw movements. Deep masseter showed the largest increase in muscle length, and the smallest changes occurred in the posterior most, superficial masseter. Each muscle part moves differently according to variations in the size and shape of insertion areas, musculoskeletal form, and patterns of jaw motion during function (Goto et al., 1995).

As the majority of muscles have a large vertical component, the moment is largest for vertical bite forces. The second largest force can be generated in posterior direction (only the posterior temporalis). Consequently, the number of muscles participating in generating a moment decreases from vertically to anteriorly to posteriorly directed bites, and this is seen for the moments. Despite this, the bite force in a posterior direction is larger than in an anterior direction. This is the direct result of the small resistance arm of the posteriorly directed bite force and thus the more efficient transfer of muscle to bite force.

The study by *Korioth and Hannam* (1994) in which the static bites on a 3D FE model of the human mandible were simulated, found that the highest occlusal forces were predicted for more posterior tooth location during intercuspal clenching. The study by *Sato* (1997), in which distribution of occlusal forces on a dental arch at various clenching strengths were measured by the Dental Prescale System, concluded that the distribution of the occlusal force was greatest on the tooth located more posteriorly in the dental arch. The proportion of occlusal force on molar regions increased and decreased on premolar and anterior teeth as clenching strength increased. Distribution of occlusal force on a dental arch should be considered from a viewpoint of movement of teeth, distortion of the mandible, positional relationship between bone and muscle, and the thickness of measuring device.

The occulsal component of the masticatory force is usually 75 to 200 N for a complete denture, and 40 to 400 N for implant-supported FPP (Lee et al., 2005). *Hansson* (2003) suggested that the loading on a dental implant consists of two components in the vertical F_v and transverse F_t directions (Courteneyharris et al., 1995). The suggested range of these external loads can be: $0 < F_v < 400$ N; and $0 < F_t < 150$ N. It was reported that the axial loading in the posterior region is

between 42 N and 412 N in an implant-supported FPP (Huiskes et al., 1987; Khraisat et al., 2004; Stanford et al., 1999).

In the present study, the influence of the variation of the magnitude and direction of the occlusal load on the remodelling model was tested. The applied load on the dental implant was gradually increased within the range of the bite force at the posterior region (150-300 N). A stable behaviour of the density of the cortical bone was obtained within the vertical force range of 250 to 300 N. As the applied vertical load is smaller than 200 N, 60% of the cortical bone and 80% of the cancellous bone had a density less than 0.4 g/cm^3. The gradual increase of the axial load on the dental implant caused an increase of the created stress in the bone within the physiological limits, where bone remodelling takes place. Combining lateral force with the axial resulted in further increase of the bone stress that consequently caused an increase in the rate of change in the apparent density. The influence of the lateral force was obvious on the stability of the density of the cortical bone when the axial load on the implant was below 250 N. In order to study the effect of the lateral force on the remodelling model, pure lateral load was applied on the implant starting with 150 N up to 300 N. The large magnitude of the lateral force combined with sudden increase of the bone stresses that consequently resulted in a large change in the bone density within a short time that finally caused a rapid drop of the density below 0.4 g/cm^3, i.e. the density of the cancellous bone calculated with Young's modulus of 300 MPa.

The response of the remodelling model to the variation of the initial stiffness of cancellous bone was tested by increasing the Young's modulus from 100 to 800 MPa keeping that of the cortical bone constant (20 GPa). The change of the Young's modulus of certain selected elements within the cancellous bone zone was studied. Starting with a very low stiffness of the cancellous bone (100 MPa) up to 300 MPa resulted in a wide remodelling range and reached a final maximum Young's modulus of 11 GPa. However, continuous increase of the stiffness of cancellous bone (400 MPa) up to 800 MPa caused shifting of the

remodelling to a lower range to obtain a final maximum Young's modulus of 9 GPa.

Experimental studies showed different remodelling activities of the cortical and cancellous bone (Gibson, 1985; Harrigan et al., 1981). Based on this fact, a density-dependant modulus-density relation was suggested by *Orr et al.* (1990), in which a bilinear power function of the new apparent density was used to calculate the elastic modulus for each element. Using this relation enables us to achieve a stable behaviour of the elements in the cortical zone with forces below 200 N applied on the implant, a matter that the previous relation that was suggested by *Carter and Hayes* (1977) failed to obtain when the applied force was smaller than 200 N, 90% of the cortical elements had density larger less than 0.2 g/cm^3 at the end of running the simulation.

It is well known that the favourable bone qualities for dental implants are quality 2 and quality 3. The highest surgical failure rate is obtained with quality 1 (4.5%) followed by quality 4 (3.9%) as presented in the report of the Dental Implant Clinical Research Group (Truhlar et al., 1994). The applied remodelling model was tested with the four different bone qualities. The model showed primary acceptable results with bone of quality 2 (Figure 52b) and quality 1 (Figure 52a). On the other hand, the results of quality 3 and quality 4, regarding the density change, were unrealistic in comparison to the clinical prognosis in particular those with quality 4 model where severe bone resorption would be expected as an outcome of the remodelling simulation. Reducing the cortical thickness to 1.0 mm and 0.5 mm resulted in more homogenous distribution of the stress in the cancellous bone zone that consequently led to a longer modelling phase (increase in the density).

5.2.2. Validation of the Computational Trabecular Geometry around an Implant by Using 6-year CT-Images

After studying the sensitivity of the remodelling model, the simulation was applied to a FE model of an implant inserted in the upper anterior region. The model was developed on the base of CT-images of a patient after six years from the insertion of the implant. Bone dimensions and implant position were created from the measurement of the CT-images. The numerically obtained trabecular structure after running the simulation of 100 time steps was close at several regions to that in the CT-images. However, and because that standard transaxial CT-images in the vicinity of metallic implants are usually associated with artefacts at the implant surface (Kalender et al., 1987), the visualisation of the bone-implant interface and bone structure around the implant was difficult.

5.2.3. Remodelling Model Including Soft Tissue Interface

The interactions in the implant-bone interface are initiated from the time of implant insertion. The biological response can, according to fracture healing, be divided into primary and secondary healing (Einhorn, 1998). *Primary healing* involves a direct healing without formation of callus. Primary healing seems to occur only when optimum conditions exist, i.e. mechanical stability and without presence of gaps. In fracture healing anatomical restoration of the bone fragments is needed (McKibbin, 1978). *Secondary fracture healing* which is supposed to take place around cementless implants occurs when optimum conditions for repair are absent and involves the formation of callus (Ashhurst, 1986; Buckwalter et al., 1995a; Buckwalter et al., 1995b; Einhorn, 1998).
Initially, a haematoma is formed and the inflammatoric response commences. The haematoma is suggested to be a source of signalling molecules which are released from platelets and inflammatoric cells. The haematoma will be invaded by cells and vessels, and callus formation begins after 7 to 14 days (Dhert et al., 1998; Sennerby et al., 1993) followed by the formation of woven bone which is

later converted to lamellar bone (Einhorn, 1998). The newly formed bone adapts to the new situation by the orientation of the bone architecture.

In the present study, the characterisation of mechanical conditions that determine the tissue differentiation was primarily based on the study of *Claes and Heigele* (1999). Regardless of individual differences in callus formation there is still a typical pattern of the tissues involved in bone healing (Claes et al., 1995b; Sevitt, 1981).

Three 3D FE models were developed in this part of the study. Each model represents one specific healing stage. The first model reflects the healing foundation within the first two weeks of implantation/immediate loading. The second and third models represent the 8th and 16th healing weeks, respectively. The remodelling simulation was applied on the three models separately. The changes in the density within the different callus layers were studied.

The first model (two weeks healing) showed a positive remodelling and increase of the element density, in particular in the thread region. The second model (two months healing) showed further increase of the density, as a continuation that was observed in the first model. However, it was associated with negative remodelling at certain regions, namely, in the spaces between the lower threads. Finally, a creation of a cortical layer at the initial SC-region was observed with the third model (four months healing).

The obtained results are comparable with the documented radiographical findings after one and six months from implant insertion. In most cases, implants showed, radiographically, the formation of a thin layer of highly dense bone which increases in its thickness until it reaches his optimal shape after six months healing period. A similar behaviour could be observed from the obtained numerical results of the three models.

However, finite element models generally have some limitations. The quality of a FE analysis strongly depends on the geometry, material properties and loading conditions (Huiskes and Hollister, 1993). The geometry of the soft tissue layer and the callus were grossly idealised in the presented model by considering a cylindrical geometry around the implant, whereas histologically, the soft tissue

layer or the callus follows the geometry of the implant. Further analysis of the healing phases with different loading conditions is necessary to validate the primary results that were presented in this work.

5.2.4. Future Perspectives

A remodelling model for osseointegrated and immediately loaded dental implants was presented in this work. The sensitivity analyses of the model under different mechanical conditions enabled the development of a generalised model for the bone remodelling around dental implants. This primary model can be further expanded to include the influence of under- and overloading immediately after implantation to study the early implant failure. Furthermore, the late implant failure can be studied too, when a modification is applied to the remodelling model to analyse the cervical bone resoption around the implants.

References

Adell R., Lekholm U., Rockler B., Brånemark P.I. A 15-year study of osseointegrated implants in the treatment of the edentulous jaw. Int J Oral Surg 1981; 10:387-416.

Adell R., Eriksson B., Lekholm U., Brånemark P.I., Jemt T. Long-term follow-up study of osseointegrated implants in the treatment of totally edentulous jaws. Int J Oral Maxillofac Implants 1990; 5:347-359.

Albrektsson T. A multicenter report on osseointegrated oral implants. J Prosthet Dent 1988; 60:75-84.

Ament C., Hofer E.P., Augat P., Claes L. Modelling of tissue transformation processes in fracture healing. Book of Abstracts, 4th Conference of the ISFR 1994:94.

Andersen E., Saxegaard E., Knutsen B.M., Haanaes H.R. A prospective clinical study evaluating the safety and effectiveness of narrow-diameter threaded implants in the anterior region of the maxilla. Int J Oral Maxillofac Implants 2001; 16:217-224.

Arpak N., Niedermeier W., Nergiz I., Schulz A., Bostanci H. Morphometry of the periimplant of immediate and late endosseous implants. J Dent Res 1995; 74:110.

Ashhurst D.E. The influence of mechanical conditions on the healing of experimental fractures in the rabbit: a microscopical study. Philos Trans R Soc Lond B Biol Sci 1986; 313:271-302.

Atwood D.A. Some clinical factors related to rate of resorption of residual ridges. J Prosthet Dent 1962; 12:441-450.

Augat P., Merk J., Genant H.K., Claes L. Quantitative assessment of experimental fracture repair by peripheral computed tomography. Calcif Tissue Int 1997; 60:194-199.

Bahat O. Treatment planning and placement of implants in the posterior maxillae: Report of 732 consecutive Nobelpharma implants. Int J Oral Maxillofac Implants 1993; 8:151-161.

Bass S.L., Triplett R.G. The effects of preoperative resorption and jaw anatomy on implant success. A report of 303 cases. Clin Oral Implants Res 1991; 2:193-198.

Bassett C.A.L. Biophysical principles affecting bone structure. In the Biochemistry and Physiology of Bone, 2nd ed., vol. III (ed. G. H. Bourne). 1971:1-77. London: Academic Press.

Beaupré G.S., Giori N.J., Blenman-Fyhrie P.R., Carter D.R. Modelling fracture healing. The influence of mechanical loading on tissue differentiation. Book of Abstracts, 4th Conference of the ISFR, 1992:1-11.

Beer A. Methoden der knochendichtemessung des unterkiefers. Thesis. Department of Biomedical Engineering and Physics, University of Vienna, Austria, 2000.

Belser U.S., Bernard J.P., Buser D. Implant placement in the aesthetic zone. In: Lindhe J., Karring T., Lang N.P. (eds). Clin Periodont Implant Dent Ed 4. Oxford: Blackwell Munksgaard 2003:915-944.

Benzing U.R., Gall H., Weber H. Biomechanical aspects of two different implant-prosthetic concepts for edentulous maxillae. Int J Oral Maxillofac Implants 1995; 10:188-198.

Biegler F.B., Hart R.T. Finite element modelling of long bone fracture healing. In: Middleton J., Pande G.N., Williams K.R. (Eds.), Recent Advances in Computer Methods in Biomechanics and Biomedical Engineering. Books and Journals International LTD, 1992:30-39.

Blenman P.R., Carter D.R., Beaupré G.S. Role of mechanical loading in the progressive ossification of a fracture callus. J Orthop Res 1989; 7:398-407.

Blunn G.W., Wait M.E. Remodelling of bone around intramedullary stems in growing patients. J Orthop. Res 1991; 9:809-819.

Borchers L., Reichart P. Three-dimensional stress distribution around a dental implant at different stages of interface development. J Dent Res 1983; 62:155-159.

Boyce T.M., Fyhrie D.P., Glotkowski M.C., Radin E.L., Schaffler M.B. Damage type and strain mode associations in human compact bone bending fatigue. J Orthop Res 1998; 16:322-329.

Brånemark P.I., Adell R., Breine U., Hansson B.O., Lindström J., Ohlsson A. Intra-osseous anchorage of dental prostheses. I. Experimental studies. Scand J Plast Reconstr Surg 1969; 3:81-100.

Buchjek K. Non-equilibrium bone remodelling: Changes of mass density and of the axes of anisotropy. Int J Engng Sci 1990; 28:1039-1004.

Buckwalter J.A., Glimcher M.J., Cooper R.R., Recker R. Bone biology. Part 1: Structure, blood supply, cells, matrix, and mineralization. J Bone Joint Surg 1995a; 77:1256-1275.

Buckwalter J.A., Glimcher M.J., Cooper R.R., Recker R. Bone biology. Part II: Formation, form, modelling, remodelling, and regulation of cell function. J Bone Joint Surg 1995b; 77:1276-1289.

Burr D.B. Targeted and nontargeted remodelling. Bone 2002; 30:2-4.

Cameron H.U., Pilliar R.M., MacNab I. The effect of movement on the bonding of the porous metal to bone. J Biomed Mater Res 1973; 7:301-311.

Canay S., Hersek N., Akpinar I., Aşik Z. Comparison of stress distribution around vertical and angled implants with finite element analysis. Quintessence Int 1996; 27:591-598.

Carlsson G.E. Clinical morbidity and sequelae of treatment with complete dentures. J Prosthet Dent 1998; 79:17-23.

Carter D.R., Hayes W.C. The compression behaviour of bone as a two-phase porous structure. J Bone Joint Surg 1977; 59:954-962.

Carter D.R., Caler W.E. Cycle-dependent and time-dependent bone fracture with repeated loading. J Biomech Eng 1983; 105:166-170.

Carter D.R. Mechanical loading histories and cortical bone remodelling. Calcif Tissue Int 1984; 36:19-24.

Carter D.R. Mechanical loading history and skeletal biology. J Biomech 1987; 20:1095-1109.

Carter D.R., Fyhrie D.P., Whalen R.T. Tabecular bone density and loading history: Regulation of connective tissue morphology by mechanical energy. J Biomech 1987; 20:785-794.

Carter D.R., Blenman P.R., Beaupré G.S. Correlations between mechanical stress history and tissue differentiation in initial fracture healing. J Orthop Res 1988; 6:736-748.

Carter D.R., Orr T.E., Fyrie D.P. Relationships between loading history and femoral cancellous architecture. J Biomech 1989; 22:231-244.

Celland N.L., Gilat A., McGlumphy E.A., Brantley W.A. A photoelastic and strain gauge analysis of angled abutments for an implant system. Int J Oral Maxillofac Implants 1993; 8:541-548.

Celletti R., Pameijer C.H., Bracchetti G., Donath K., Persichetti G., Visani I. Histologic evaluation of osseointegrated implants restored in nonaxial functional occlusion with preangled abutments. Int J Periodont Rest Dent 1995; 15:563-573.

Cheal E.J., Mansmann K.A., DiGioia A.M., Hayes W.C., Perren S.M. Role of interfragmentary strain in fracture healing: ovine model of a healing osteotomy. J Orthop Res 1991; 9:131-142.

Chun H.J., Cheong S.Y., Han J.H., Heo S.J., Chung J.P., Rhyu I.C., Choi Y.C., Baik H.K., Kim M.H. Evaluation of design parameters of osseointegrated dental implants using finite element analysis. J Oral Rehabil 2002; 29:565-574.

Churches A.E., Howlett C.R., Waldron K.J., Ward G.W. The response of living bone to controlled, time varying loading: Method and preliminary results. J Biomech 1979; 12:35-45.

Claes L.E., Wilke H.J., Augat P., Rübenacker S., Margevicius K.J. Effect of dynamization of gap healing of diaphyseal fractures under external fixation. Clin Biomech 1995a; 10:227-234.

Claes L.E., Wilke H.J., Kiefer H. Osteonal structure better predicts tensile strength of healing bone than volume fraction. J Biomech 1995b; 28:1377-1390.

Claes L.E., Heigele C.A. Magnitudes of local stress and strain along bony surfaces predict the course and type of fracture healing. J Biomech 1999; 32:255-266.

Cochran D.L., Schenk R.K., Lussi A., Higginbottom F.L., Buser D. Bone response to unloaded and loaded titanium implants with a sandblasted and acid-etched surface: A histometric study in the canine mandible. J Biomed Mater Res 1998; 40:1-11.

O'Connor J.A., Lanyon L.E., MacFie H. The influence of strain rate on adaptive bone remodelling. J Biomech 1982; 15:767-781.

Courteneyharris R.G., Kayser M.V., Downes S. Comparison of the early production of extracellular-matrix on dense hydroxyapatite and hydroxyapatite-coated titanium in cell and organ-culture. Biomat 1995; 16:489-495.

Cowin S.C., Hegedus D.H. Bone remodelling I: Theory of adaptive elasticity. J Elasticity 1976; 6:313-326.

Cowin S.C., Firoozbakhsh K. Bone remodelling of diaphysial surfaces under constant load: Theoretical predictions. J Biomech 1981a; 7:471-484.

Cowin S.C., Firoozbakhsh K. An analytical model of Pauwel's functional adaptation mechanics in bone. J Biomech Eng 1981b; 103:246-252.

Cowin S.C. Mechanical modelling of the stress adaptation process in bone. Calcif Tissue Int 1984; 36:98-103.

Cowin S.C., Hart R.T., Balser J.R., Kohn D.H. Functional adaptation in long bones: Establishing in vivo values for surface remodelling rate coefficients. J Biomech. 1985; 18:665-684.

Cowin S.C. Bone mechanics handbook. CPC Press, Boca Raton 2001.

Davies J.E., Ottensmeyer P., Shen X., Hashimoto M., Peel S.A.F. Early extracellular matrix synthesis by bone cells. In: The bone-biomaterial interface (Ed. Davies JE). University of Toronto Press. Toronto 1991; 20:214-228.

Davy D.T., Connolly J.F. The biomechanical behaviour of healing canine radii and ribs. J Biomech 1982; 15:235-247.

Dhert W.J., Thomsen P., Blomgren A.K., Esposito M., Ericson L.E., Verbout A.J. Integration of press-fit implants in cortical bone: A study on interface kinetics. J Biomed Mater Res 1998; 41:574-583.

DiGioia A.M., Cheal E.J., Hayes W.C. Three-dimensional strain fields in a uniform osteotomy gap. J Biomech Eng 1986; 108:273-280.

Eger D.E., Gunsolley J.C., Feldman S. Comparison of angled and standard abutments and their effect on clinical outcomes: A preliminary report. Int J Oral Maxillofac Implants 2000; 15:819-823.

Einhorn T.A. The cell and molecular biology of fracture healing. Clin Orthop Relat Res 1998:7-21.

Ellis D.K., Natali A. Dental biomechanics. New York: Taylor & Francis 2003:1-19.

Engquist B., Bergendal T., Kallus T., Linden U. A retrospective multicenter evaluation of osseointegrated implants supporting overdentures. Int J Oral Maxillofac Implants 1988; 3:129-134.

Eriksen E.F., Mosekilde L., Melsen F. Effect of sodium fluoride, calcium, phosphate, and vitamin D2 on trabecular bone balance and remodelling in osteoporotics. Bone 1985; 6:381-389.

Friberg B., Jemt T., Lekholm U. Early failures in 4,641 consecutively placed Brånemark dental implants: A study from stage 1 surgery to the connection of completed prostheses. Int J Oral Maxillofac Implants 1991; 6:142-146.

Friberg B. Treatment with dental implants in patients with severe osteoporosis: A case report. Int J Periodontics Restorative Dent 1994; 14:348-353.

Friberg B., Sennerby L., Roos J., Johansson P., Strid C.G. Lekholm U. Evaluation of bone density using cutting resistance measurements and microradiography: An in vitro study in pig ribs. Clin Oral Implants Res 1995a; 6:164-171.

Friberg B., Sennerby L., Roos J., Lekholm U. Identification of bone quality in conjunction with insertion of titanium implants: A pilot study in jaw autopsy specimens. Clin Oral Implants Res 1995b; 6:213-219.

Friberg B., Sennerby L., Meredith N., Lekholm U. A comparison between cutting torque and resonance frequency measurements of maxillary implants. Oral Maxillofac Surg 1999; 28:297-303.

Friberg B., Gröndahl K., Lekholm U., Brånemark P.I. Long-term follow-up of severely atrophic edentulous mandibles reconstructed with short Brånemark implants. Clin Implant Dent Relat Res 2000; 2:184-189.

Frost H.M. Presence of microscopic cracks in vivo in bone. Henry Ford Hospital Medical Bulletin 1960; 8:25-35.

Frost H.M. Bone Remodelling Dynamics. Springfield, IL: Charles C.Thomas 1963.

Frost H.M. The law of bone structure. Charles C. Thomas, Springfield 1964.

Frost H.M. Bone Modelling and Skeletal Modelling Errors. Springfield, IL: Charles C. Thomas 1973.

Frost H.M. Intermediary Organization of the Skeleton. Boca Raton, FL:CRC Press 1986.

Frost H.M. Bone "mass" and the "mechanostat": A proposal. Anat Rec 1987; 219:1-9.

Frost H.M. Obesity, and bone strength and "mass": A tutorial based on insights from a new paradigm. Bone 1997; 21:211-214.

Frost H.M. Bone's Mechanostat: A 2003 update. Anat Record part A 2003; 275:1081-1101.

Fyhrie D.P., Carter D.R. A unifying principle relating stress to trabecular bone morphology. J Orthop Res 1986; 4:304-317.

Gapski R. Wanh H.L., Mascarenhas P., Lang N.P. Critical review of immediate implant loading. Clin Oral Implants Res 2003; 14:515-527.

García J.M., Martínez M.A., Doblaré M. An anisotropic internal–external bone adaptation model based on a combination of CAO and continuum damage mechanics technologies. Comput Meth in Biomech Biomed Engin 2001; 4:355–377.

Garn S.M. The Earlier Gain and the Later Loss of Cortical Bone. Springfield, IL: Charles C. Thomas 1970.

Gelb D.A., Lazzara R.J. Hierarchy of objectives in implant placement to maximize esthetics: Use of preangulated abutments. Int J Periodont Rest Dent 1993; 13:277-287.

Geng J.P., Ma Q.S., Xu W., Tan K.B., Liu G.R. Finite element analysis of four thread-form configurations in a stepped screw implant. J Oral Rehabil 2004; 31:233-239.

Geng J.P., Xu D.W., Tan K.B., Liu G.R. Finite element analysis of an osseointegrated stepped screw dental implant. J Oral Implantol 2004; 30:223-233.

Geramy A., Morgano S.M. Finite element analysis of three designs of an implant-supported molar crown. J Prosthet Dent 2004; 92:434-440.

Gibson L.J. The mechanical behaviour of cancellous bone. J Biomech 1985; 18:317-328.

References

Goto T.K., Langenbach G.E., Korioth T.W., Hagiwara M., Tonndorf M.L., Hannam A.G. Functional movements of putative jaw muscle insertions. Anat Rec 1995; 242:278-288.

Goto T.K., Langenbach G.E., Hannam A.G. Length changes in the human masseter muscle after jaw movement. Anat Rec 2001; 262:293-300.

Hansson S. Implant-abutment interface: Biomechanical study of flat top versus conical. Clin Implants Dent Rel Res 2000; 2:33-41.

Hansson S. A conical implant-abutment interface at the level of the marginal bone improves the distribution of stresses in the supporting bone: An axisymmetric finite element analysis. Clin Oral Implants Res 2003; 14:286-293.

Hansson S., Werke M. The implant thread as a retention element in cortical bone: The effect of thread size and thread profile: A finite element study. J Biomech 2003; 36:1247-1258.

Harrigan T.P., Caner D.R., Mann R.W., Harris W.H. The influence of apparent density and trabecular orientation on the elastic modulus of cancellous bone. Trans Orthop Res Soc 1981; 6:277-281.

Hart R.T., Davy D.T., Heiple K.G. A computational method for solution of adaptive elasticity problems. Advances in Bioengineering, American Society of Mechanical Engineers 1982:123-126.

Hart R.T., Davy D.T., Heiple K.G. A predictive model for strain-induced remodelling in long bones. Transactions of the 1983. Orthop Res Society 1983:71.

Hart R.T., Davy D.T., Heiple K.G. Mathematical modelling and numerical solutions for functionally dependent bone remodelling. Calcif Tissue Int 1984a; 36:104-109.

Hart R.T., Davy D.T., Heiple K.G. A computational method for stress analysis of adaptive elastic materials with a view towards applications in strain-induced bone remodelling. J Biomech Eng 1984b; 106:342-350.

Hart R.T., Davy D.T. Theories of bone modelling and remodelling in: Cowin Sc. (ed.). Bone Mechanics CRC Press, Boca Raton 1989:253-277.

Hart R.T., Henebbel V., Thongpreda N., van Buskirk W.C., Anderson R.C. Modelling the biomechanics of the mandible: A three dimensional finite element study. J Biomech 1992; 25:261-286.

Hassler C.R., Rybicki E.F., Cummings K.D., Clark L.C. Quantification of bone stresses during remodelling. J Biomech 1980; 13:185-190.

Helkimo E., Carlsson G.E., Helkimo M. Bite force and state of dentition. Acta Odontol Scand 1977; 35:297-303.

Hert J., Lisková M., Landrgot B. Influence of the long-term continuous bending on the bone. Folia Morphol 1969; 17:389-399.

Hert J., Lisková M., Landa M. Reaction of bone to mechanical stimuli. Part I. Continuous and intermittent loading of tibia in rabbit. Folia Morphol 1971; 19:290-300.

Hert J., Fiala P., Petrtyl M. Osteon orientation of the diaphysis of the long bones in man. Bone 1994; 15:269-277.

Higuchi K.W., Folmer T., Kultje C. Implant survival rate in partially edentulous patients. A 3-year prospective multicenter study. J Oral Maxillofac Surg 1995; 53:264-268.

Hillam R.A., Skerry T.M. Inhibition of bone resorption and stimulation of formation by mechanical loading of the modelling rat ulna in vivo. J Bone Miner Res 1995; 10:683-689.

Hirayabashi M., Motoyoshi M., Ishimaru T., Kasai K., Namura S. Stress in mandibular cortical bone during mastication: Biomechanical considerations using a three dimensional finite element method. J Oral Science 2002; 44:1-6.

Hobkirk J.A., Schwab J. Mandibular deformation in subjects with osseointegrated implants. Int J Oral Maxillofac Implants 1991; 6:319-328.

Horinchi K., Uchida H., Yamamoto K., Sugimura M. Immediate loading of Brånemark System Implant Following Placement In Edentulous Patients: A Clinical Report. Int J Oral Maxillofac Implants 2000; 15:824-830.

Huiskes R. Some fundamental aspects of human joint replacement. Acta Orthop Scand Suppl 1980; 185:1-208.

Huiskes R., Weinans H., Grootenboer H.J., Dalstra M., Fudala B., Slooff T.J. Adaptive bone remodelling theory applied to prosthetic design analysis. J Biomech 1987; 20:1135-1150.

Huiskes R., Weinans H., Reitbergen B.V., Sumner D.R., Turner T.M., Galante J.O. Validation of strain adaptive bone-remodelling analysis to predict bone morphology around non-cemented THA. Orthopedic Trans 1991; 15:399.

Huiskes R., Hollister S.J. From structure to process, from organ to cell: recent developments of FE-Analysis in orthopaedic biomechanics. J Biomech Eng 1993; 115:520-527.

Jaffin R.A., Berman C.L. The excessive loss of Brånemark fixtures in type IV bone: A 5-year analysis. J Periodontol 1991; 62:2-4.

Jee W.S., Frost H.M. Skeletal adaptations during growth. Triangle 1992; 31:77-88.

Jemt T., Strid K.G. Assessment of bone quality from cutting resistance during implant surgery. Int J OralMaxillofac Surg 1994; 9:279-288.

Jemt T., Lekholm U. Implant treatment in edentulous maxillae: A five-year follow-up report on patients with different degrees of jaw resorption. Int J Oral Maxillofac Implants 1995; 10:303-311.

Johansson P., Strid K.G. Assessment of bone quality from cutting resistance during implant surgery. Int J Oral Maxillofac Implants 1994; 9:279-288.

Jones P.M. Complete dentures and the associated soft tissues. J Prosthet Dent 1976; 36:136-149.

Johns R.B., Jemt T., Heath M.R., Hutton J.E., McKenna S., McNamara D.C., van Steenberghe D., Taylor R., Watson R.M., Herrmann I. A multicenter study of overdentures supported by Brånemark implants. Int J Oral Maxillofac Implants 1992; 7:513-522.

Jurvelin J.S., Buschmann M.D., Hunziker E.B. Optical and mechanical determination of Poisson's ratio of adult bovine humeral articular cartilage. J Biomech 1997; 30:235-241.

References

Kalender W.A., Hebel R., Ebersberger J. Reduction of CT artefacts caused by metallic implants. Radiology 1987; 164:576–577.

Kallus T., Henry P., Jemt T., Jörnéus L. Clinical evaluation of angled abutments for the Brånemark system: A pilot study. Int Oral Maxillofac Implants 1990; 5:39-45.

Kawahara H., Kawahara D., Hayakawa M., Tamai Y., Kuremoto T., Matsuda S. Osseointegration under immediate loading: Biomechanical stress-strain and bone formation-resorption. Implant Dent 2003; 12:61-68.

Keilig L., Bourauel C., Grüner M., Hültenschmidt R., Bayer S., Utz K.H., Stark H. Aufbau und Erprobung eines neuartigen Meßsystems für die dentale Biomechanik-Meßprinzip und Beispielmessungen des Hexapod-Meß-Systems. Biomed Technik 2004; 49:208-215.

Kenney R., Richards M.W. Photoelastic stress patterns produced by implantretained overdentures. J Prosthet Dent 1998; 80:559-564.

Khraisat A., Hashimoto A., Nomura S., Miyakawa O. Effect of lateral cyclic loading on abutment screw loosening of an external hexagon implant system. J Prosthet Dent 2004; 91:326-334.

Kingsmill V.J., Boyde A. Variation in the apparent density of human mandibular bone with age and dental status. J Anat 1998; 192:233-244.

Kirsch A., Mentag P.J. The IMZ endosseous two phase implant system: A complete oral rehabilitation treatment concept. J Oral Implantol 1986; 12:576-589.

Koolstra J.H., van Eijden T.M.G.J. Three dimensional dynamical capabilities of the human masticatory muscles. J Biomech 1999; 32:145-152.

Korioth T.W., Hannam A.G. Mandibular forces during simulated tooth clenching. J Orofac Pain 1994; 8:178-189.

Koseki M., Inou N., Maki K. Estimation of masticatory forces for patient-specific analysis of the human mandible. Nihon Kikia Gakkai Nenji Taikai Koen Ronbunshu 2005; 5:155-156.

Krekmanov L., Kahn M., Rangert B., Lindström H. Tilting of posterior mandibular and maxillary implants for improved prosthesis support. Int J Oral Maxillofac Implants 2000; 15:405-414.

Lazenby R.A. Continuing periosteal apposition. I. Documentation, hypotheses, and interpretation. Am J Phys Anthropol 1990a; 82:451-472.

Lazenby R.A. Continuing periosteal apposition. II. The significance of peak bone mass, strain equilibrium, and age-related activity differentials for mechanical compensation in human tubular bones. Am J Phys Anthropol 1990b; 82:473-484.

Lee J.H., Frias V., Lee K.W., Wright R.F. Effect of implant size and shape on implant success rates: A literature review. J Prosthet Dent 2005; 94:377-381.

Lee T.C., Staines A., Taylor D. Bone adaptation to load: Microdamage as a stimulus for bone remodelling. J Anat 2002; 201:437-446.

Lekholm U., Zarb G.A. Patient selection and preparation. In: Brånemark P.I., Zarb G., Albrektsson T., eds. Tissue-integrated prostheses. Osseointegration in clinical dentistry 1985:199–209. Chicago: Quintessence Publishing Company Inc.

Lekholm U., van Steenberghe D., Herrmann I., Bolender C., Folmer T., Gunne J., Henry P., Higuchi K., Laney W.R., Lindén U. Osseointegrated implants in the treatment of partially edentulous jaws: A prospective 5-year multicenter study. Int J Oral Maxillofac Implants 1994; 9:627-635.

Li J., Li H., Shi L., Fok A., Ucer C., Devlin H., Horner K., Silikas N. A mathematical model for simulating the bone remodelling process under mechanical stimulus. Dental Mater 2007; 23:1073-1078.

Lindh C., Nilsson M., Klinge B., Petersson A. Quantitative computed tomography of trabecular bone in the mandible. Dentomaxillofac Radiol 1996; 25:146-150.

Lindh T., Gunne J., Tillberg A., Molin M. A meta-analysis of implants in partial edentulism. Clin Oral Implants Res 1998; 9:80-90.

Liskova M., Hert J. Reaction of bone to mechanical stimuli. Part II. Periosteal and endosteal reaction of tibial diaphysis in rabbit to intermittent loading. Folia Morphol 1971; 19:301-317.

Lundgren D., Laurell L., Falk H., Bergendal T. Occlusal force pattern during mastication in dentitions with mandibular fixed partial dentures supported on osseointegrated implants. J Prosthet Dent 1987; 58:197-203.

O'Mahony A.M., Williams J.L., Spencer P. Anisotropic elasticity of cortical and cancellous bone in the posterior mandible increases peri-implant stress and strain under oblique loading. Clin Oral Implants Res 2001; 12:648-657.

Mailath G., Stoiber B., Watzek G., Matejka M. Die Knochenresorption an der Eintrittstelle osseointegrierter Implantate: Ein biomechanisches Phänomen. Eine Finite-Element-Studie. Zeitschrift für Stomatologie 1989; 86:207-216.

Makoto S., Kenji S., Koichi K. Measurements of mechanical properties of cortical bone using nanoindication tests. Proceedings of Annual Meeting of Japanese Society for Orthopaedic Biomechanics 2003; 24:1-5.

Martin R.B., Burr D.B. Structure, function and adaptation of compact bone. Raven Press, New York 1989.

Martin R.B. Fatigue microdamage as an essential element of bone mechanics and biology. Calcif Tissue Int 2003; 73:101-107.

McHorris W.H. The importance of anterior teeth. J Gnath 1982; 1:19-36.

McKibbin B. The biology of fracture healing in long bones. J Bone Joint Surg [Br] 1978; 60:150-162.

Meade J.B., Cowin S.C., Klawitter J.J., Skinner H.B., van Buskirk W.C. Short term modelling due to hyperphysiological stress. Transactions of the 1983. Orthop Res Society 1981:62.

Meredith N. Assessment of implant stability as a prognostic determinant. Int J Prosthodont 1998; 11:491-501.

Mericske-Stern K. Overdentures with roots or implants for elderly patients. A comparison. J Prosthet Dent 1994; 72:543-550.

Mericske-Stern R., Assal P., Mericske E., Bürgin W. Occlusal force and oral tactile sensibility measured in partially edentulous patients with ITI implants. Int J Oral Maxillofac Implants 1995; 10:345-354.

Meyer V., Wiesmann H.P., Fillies T., Joos U. Early tissue reaction at the interface of immediately loaded dental implants. Int J Oral Maxillofac Implants 2003; 18:489-499.

Misch C.E. Density of bone: Effect on treatment plans, surgical approach, healing and progressive bone loading. Int J Oral Implantol 1990; 6:23-31.

Misch C.E. Progressive loading of bone with implant prostheses. J Dent Symp 1993; 1:50-53.

Misch C.E. Bone density: A key determinant for clinical success. In: Misch C.E., ed. Contemporary Implant Dentistry, 2nd ed. St Louis, Mo: Mosby 1999.

Morris H.F., Ochi S., Gillette W. Bone quality and implant integration during follow-up in the DICRG clinical study. J Dent Res 1995; 74:495-753.

Müftü S., Müftü A. Biomechanics of tooth and jaw. In: Webster,JG. (Ed.), Encyclopedia of Medical Devices and Instrumentation. Wiley, NY 2006:411-428.

Mundt T., Mack F., Schwahn C., Biffar R. Private practice results of screw-type tapered implants: Survival and evaluation of risk factors. Int J Oral Maxillofac Implants 2006; 21:607-614.

Närhi T.O., Ettinger R.L., Lam E.W. Radiographic findings, ridge resorption, and subjective complaints of complete denture patients. Int J Prosthodont 1997; 10:183-189.

Naert I., Koutsikakis G., Duyck J., Quirynen M., Jacobs R., van Steenberghe D. Biologic outcome of implant-supported restorations in the treatment of partial edentulism. Part I: A longitudinal clinical evaluation. Clin Oral Implants Res 2002; 13:382-389.

Nordin T., Jonsson G., Nelvig P., Rasmusson L. The use of a conical fixture design for fixed partial prostheses: A preliminary report. Clin Oral Implants Res 1998; 9:343-347.

Norton M. Marginal bone levels at single tooth implants with a conical fixture design: The influence of surface macro- and microstructure. Clin Oral Implants Res 1998; 9:91-99.

van Oosterwyck H., Duyck J., Vander Sloten J., van der Perre G., De Cooman M., Lievens S., Puers R., Naert I. The influence of bone mechanical properties and implant fixation upon bone loading around oral implants. Clin Oral Implants Res 1998; 9:407-418.

Orr T.E., Beauprè G.S., Carter D.R., Schurman D.J. Computer predictions of bone remodelling around porous-coated implants. J Arthoplasty 1990; 5:191-200.

Palmer R.M., Smith B.J., Palmer P.J., Floyd P.D. A prospective study of Astra single tooth implants. Clin Oral Implants Res 1997; 8:173-179.

Papavasiliou G., Kamposiora P., Bayne S.C., Felton D.A. Three-dimensional finite element analysis of stress-distribution around single tooth implants as a function of bony support, prosthesis type, and loading during function. J Prosthet Dent 1996; 76:633-640.

Parfitt A.M. Quantum concept of bone remodelling and turnover: implications for the pathogenesis of osteoporosis. Calcif Tissue Int 1979; 28:1-5.

Parfitt A.M. Osteonal and hemi-osteonal remodelling: The spatial and temporal framework for signal traffic in adult human bone. J Cell Biochem 1994; 55:273-286.

Parfitt A.M. The mechanism of coupling: A role for the vasculature. Bone 2000; 26:319-323.

Patra A.K., DePaolo J.M., D'Souza K.S., DeTolla D., Meenaghan M.A. Guidelines for analysis and redesign of dental implants. Implant Dent 1998; 7:355-368.

Pearce A.I., Richards R.G., Milz S., Schneider E., Pearce S.G. Animal models for implant biomaterial research in bone: A review. Eur Cell Mater 2007; 13:1-10.

Pierrisnard L., Hure G., Barquins M., Chappard D. Two dental implant design for immediate loading: A finite element analysis. Int J Oral Maxillofac Implants 2002; 17:353-362.

Poumarat G., Squire P. Comparison of mechanical properties of human, bovine bone and a new processed bone xenograft. Biomater 1993; 14:337-340.

Puchades-Roman L., Palmer R.M., Palmer P.J., Howe L.C., Ide M., Wilson R.F. A clinical, radiographic, and microbiologic comparison of Astra Tech and Brånemark single tooth implants. Clin Implants Dent Rel Res 2000; 2:78-84.

Raadsheer M.C., van Eijden T.M., van Ginkel F.C., Prahl-Andersen B. Contribution of jaw muscle size and craniofacial morphology to human bite force magnitude. J Dent Res 1999; 78:31-42.

Rahimi A., Keilig L., Bendels G., Klein R., Buzug T.M., Abdelgader I., Abboud M., Bourauel C. 3D reconstruction of dental specimens from 2D histological images and microCT-scans. Comput Methods Biomech Biomed Engin 2005; 8:167-76.

Rahimi A., Bourauel C., Jäger A., Gedrange T., Heinemann F. Load transfer by fine threading the implant neck: A FEM study. J Physiol Pharmacol 2009; 60 (Suppl 8):107-112.

Rasmusson L., Kahnberg K.E., Tan A. Effects of implant design and surface on bone regeneration and implant stability: An experimental study in the dog mandible. Clin Implant Dent Related Res 2001; 3:2-8.

Reiter T.J. Functional adaptation of bone and application in optimal structural design. VDI-Berichte 1996; 17:145.

Robling A.G., Castillo A.B., Turner C.H. Biomechanical and molecular regulation of bone remodelling. Annu Rev Biomed Eng 2006; 8:455-498.

Rubin C.T., Lanyon L.E. Bone remodelling in response to applied dynamic loads. Orthop Trans 1981; 5:2-37.

Rubin C.T., Lanyon L.E. Regulation of bone formation by applied dynamic loads. J Bone Joint Surg Am 1984; 66:397-402.

Rubin C.T., Lanyon L.E. Regulation of bone mass by mechanical strain magnitude. Calcif Tissue Int 1985; 37:411-417.

Saab X., Griggs J., Powers J., Engelmeier R. Effects of abutment angulation on the strain on the bone around an implant in the anterior maxilla: A finite element study. J Prosthet Dent 2007; 97:85-92.

Sato T. A study of bite force distribution on the dental arch in normal subjects. J Japan Prosthodont Society 1997; 41:634 (in Japanese with English abstract).

Schaeffer A. Behaviour of the axis of human incisor teeth during growth. Angle Orthodont 1949; 19:254-275.

Sennerby L., Thomsen P., Ericson L.E. Early response to titanium implants inserted in rabbit in cortical bone. J Mater Sci Mater Med 1993; 4:240-250.

Sethi A., Kaus T., Sochor P. The use of angulated abutments in implant dentistry: five-year clinical results of an ongoing prospective study. Int J Oral Maxillofac Implants 2000; 15:801-810.

Sevitt S. Secondary repair of fractures. Events preparatory to union. In: Sevitt S., (Ed.), Bone Healing and Fracture Repair in Man 1981. Churchill Livingstone.

Smith D.E. Review of endosseous implants for partially edentulous patients. Int J Prosthodont 1990; 3:12-19.

Søballe K., Brockstedt-Rasmussen H., Hansen E.S., Bünger C. Hydroxyapatite coating modifies implant membrane formation. Controlled micromotion studied in dogs. Acta Orthop Scand 1992a; 63:128-140.

Søballe K., Hansen E.S., Brockstedt-Rasmussen H., Jørgensen P.H., Bünger C. Tissue ingrowth into titanium and hydroxyapatite-coated implants during stable and unstable mechanical conditions. J Orthop Res 1992b; 10:285-299.

Stanford C.M., Brand R.A. Toward an understanding of implant occlusion and strain adaptive bone modelling and remodelling. J Prosthet Dent 1999; 81:553-561.

van Steenberghe D., Lekholm U., Bolender C., Folmer T., Henry P., Herrmann I., Higuchi K., Laney U., Linden U., Astrand P. The applicability of osseointegrated

oral implants in the rehabilitation of partial edentulism: A prospective multicenter study on 558 fixtures. Int J Oral Maxillofac Implants 1990; 5:272-281.

Stegaroiu R., Sato T., Kusakari H., Miyakawa O. Influence of restoration type on stress distribution in bone around implants: A three-dimensional finite element analysis. Int J Oral Maxillofac Implants 1998; 13:82-90.

Stoiber B. Biomechanische Grundlagen enossaler Schraubenimplantate. Diss. Universitätsklinik für Zahn-, Mund- und Zahnheilkunde, Wien 1988.

Sullivan D.Y. Prosthetic considerations for the utilization of osseointegrated fixtures in the partially edentulous arch. Int J Oral Maxillofac Implants 1986; 1:39-45.

O'Sullivan D., Sennerby L., Meredith N. Measurements comparing the initial stability of five designs of dental implants: A human cadaver study. Clin Implant Dent Related Res 2000; 2:85-92.

Thompson D. On growth and form. Am J Orthod 1952; 53:881-903.

Trisi P., Rao W. Bone classification: Clinical histomorphometric comparison. Clin Oral Implants Res 1999; 10:1-7.

Truhlar R.S., Morris H.F., Ochi S., Winkler S. Second-stage failures related to bone quality in patients receiving endosseous dental implants: DICRG interim report No. 7. Dental Implant Clinical Research Group. Implant Dent 1994; 3:252-255.

Tsai S.W., Wu E.M. General theory of strength for anisotropic materials. J Composite Mater 1971; 5:58-80.

Ulm C., Solar P., Blahout R., Matejka M., Gruber H. Reduction of the compact and cancellous bone substances of the edentulous mandible caused by resorption. Oral Surg Oral Med Oral Pathol 1992; 74:131-136.

Ulm C., Kneissel M., Schedle A., Solar P., Matejka M., Schneider B., Donath K. Characteristic features of trabecular bone in edentulous maxillae. Clin Oral Implant Res 1999; 10:459-467.

Verborgt O., Gibson G.J., Schaffler M.B. Loss of osteocyte integrity in association with microdamage and bone remodelling after fatigue in vivo. J Bone Miner Res 2000; 15:60-67.

Watzak G., Zechner W., Ulm C., Tangel S., Tepper G., Watzer G. Histologic and histomorphometric analysis of three types of dental implants following 18 months of occlusal loading: A preliminary study in baboons. Clin Oral Implants Res 2005; 16:408-416.

Wennerberg A., Albrektsson T., Andersson B. Design and surface characteristics of 13 commercially available oral implant systems. Int J Oral Maxillofac Implants 1993; 8:622-633

Wennerberg A. On surface roughness and implant incorporation. PhD Thesis. Götegborg: Biomaterials/Handicap Research, Göteborg University 1996.

Weibel E.R. Stereological Methods, Vol. 2: Theoretical Foundations, Academic Press, New York 1980.

Weinans H., Huiskes R., Grootenboer H.J. Convergence and uniqueness of adaptive bone remodelling. Trans 35th Orthop Res Soc 1989; 14:310.

Weinans H., Huiskes R., Grootenboer H.J. A hypothesis concerning minimal bone density threshold levels as final stages of bone remodelling. Trans 35th Orthop Res Soc 1990; 15:78.

Weinans H., Huiskes R., Grootenboer H.J. The behaviour of adaptive bone-remodelling simulation models. J Biomech 1992; 25:1425-1441.

Wolff J. Über die innere Architektur der Knochen und ihre Bedeutung für die Frage vom Knochenwachstum. Virchows Arch Pathol Anat Physio Klein Med 1870; 50:389.

Wolff J. Das Gesetz der Transformation der Knochen. Hirschwald Berlin 1892.

Wyatt C.L., Zarb G.A. Treatment outcomes of patients with implant-supported fixed partial prostheses. Int J Oral Maxillofac Implants 1998; 13:204-211.

Zarb G.A., Schmitt A. The longitudinal clinical effectiveness of osseointegrated dental implants: The Toronto Study. Part II: The prosthetic results. J Prosthet Dent 1990; 64:53-61.

Zarb G.A., Zarb F.L., Schmitt A. Osseointegrated implants for partially edentulous patients. Interim considerations. Dent Clin North Am 1987; 31:457-472.

Zarb J.P., Zarb G.A. Implant prosthodontic management of anterior partial edentulism: Long-term follow-up of a prospective study. J Canadian Dent Asso 2002; 68:92-96.

List of Symbols

$d\rho/dt$:	Rate of change in the apparent density of the bone at a particular location
ρ:	Apparent bone density
σ:	Local stress tensor
ε:	Local strain tensor
ρ_{cb}:	Maximal density of cortical bone
B:	Remodelling constant
S:	Daily mechanical stimulus
K:	Reference stimulus
dE/dt:	Rate of change of elastic modulus E
E:	Local modulus of elasticity
e_{ij}:	Actual strain tensor
e°_{ij}:	Equilibrium strain tensor
A_{ij}:	Matrix of remodelling coefficients
dX/dt:	Rate of surface growth
X:	Characteristic surface coordinate perpendicular to the surface
B_{ij}:	Matrix of coefficients for external remodelling
s_{ij}:	Local stress tensor
U:	Actual strain energy density
U_n:	Site-specific homeostatic equilibrium strain energy density
C_e, C_x:	Remodelling rate coefficients
n:	Number of elements for internal remodelling
ΔE:	Change in the elastic modulus in one time-step
Δt:	Period of one time-step
m:	Number of surface nodal points considered
c:	Discrete loading condition
s:	Continuum model cyclic peak effective stress (scalar quantity)
S_{eff}:	Effective stress

D:	Constant
U/ρ:	Mechanical daily stimulus
w:	Half-width of the dead zone
C:	Constant
ρ_0:	Initial density of the bone
σ_1:	Lower critical stress
σ_2:	Upper critical stress

Glossary

FPP	Fixed Partial Prosthesis
3D	Three-Dimensional
BSUs	Bone Structural Units
BMU	Basic Multicellular Unit
MES	Minimal Effective Strain
(FE)M	Finite Element Method
SED	Strain Energy Density
MESr	Mechanically-Controlled Disuse-Mode Remodelling
LBB	Load-Bearing Bone
MESp	Microdamage Threshold Range
MDx	Microscopic Fatigue Damage
Fx	Fracture Strength
EEL	Element Edge Length
CT-Image	Computer Tomography-Image
CT	Connective Tissue
MSC	Intermediate Stiffness Callus
SOC	Soft Callus
SC	Stiff Callus
DVT	Digital Volume Tomography
SAM	Straight Abutment Model
AAM	Angled Abutment Model
HexMeS	Hexpod Measurement System